Cavity-Enhanced Laser-Induced Fluorescence for Real-time Breath Acetone Monitoring

NADA AHMED A AL-TAISAN

Cavity-Enhanced Laser-Induced Fluorescence for Real-time Breath Acetone Monitoring

Nada Ahmed Al Taisan

Abstract

Diabetic ketoacidosis (DKA) is a life threatening complication in children with type 1 diabetes. In DKA, the body breaks down fatty acids as an alternative energy source producing high concentrations of acidic blood ketones. Normally, DKA is treated by a "guess" dosage of intravenous insulin infusion following blood analysis. There is an unmet need for alternative, non-invasive methods to the inaccurate, untimely blood tests to monitor each patient's response to the treatment in real time. This will help in determining the optimum insulin dosage and adjusting the treatment protocol. Breath-acetone measurement is a promising non-invasive alternative as it is proportional to blood ketone concentrations.

This thesis describes building a device based on the cavity-enhanced laser-induced fluorescence (CELIF) technique for real-time, online, non-invasive breath acetone measurements. CELIF combines the sensitivity of laser-induced fluorescence (LIF) and the absolute measurement capabilities of cavity ring-down spectroscopy (CRDS) into one cross-correlated technique.

The device is capable of making an acetone CELIF measurement in 100 ms, with a concentration dynamic range of 1.6–2000 ppm, covering the range of breath acetone concentration a DKA patient might have. The response time of the device is fast enough to follow a real breath pattern, with a 10–90% rise time of the CELIF signal of 370 ± 15 ms, and a 90–10% fall time of 850 ± 21 ms, which is enough for the signal to rise and find the maximum acetone concentration, then decay back to the background level before the next breath arrives. The performance of the acetone CELIF device was validated by using a selected-ion flow-tube mass spectrometer (SIFT-MS). The results show that this device is useful for reliable online breath acetone analysis. Subsequently, the validated CELIF device was tested for breath acetone measurements in fasted healthy human subjects, using a home-built, online, buffered end-tidal breath sampler.

Cavity-Enhanced Laser-Induced Fluorescence for Real-time Breath Acetone Monitoring

Nada Ahmed Al Taisan

A thesis submitted in partial fulfilment
of the requirements for the degree of
Doctor of Philosophy

Department of Physics
University of Durham
England

October, 2019

Contents

List of Figures

Declaration

The work in this thesis is based on research carried out at the Department of Physics, University of Durham. No part of this thesis has been submitted elsewhere for any other degree or qualification and it is all my own work unless referenced to the contrary in the text.

Acknowledgements

My five year PhD journey involved many people who have contributed to the success of this project. Hereby, I would like to take this chance to thank them. First and foremost, I would like to express my sincere gratitude to my supervisor, Dr David Carty for his continuous guidance, support, patience and motivation throughout my PhD. His guidance helped me in all the time of research and writing of this thesis. I could not have imagined having a better supervisor for my PhD study.

Besides my supervisor, I would like to thank my co-supervisor, Dr Eckart Wrede for his guidance, immense knowledge and encouragement throughout my PhD. Anyone would be lucky to have David and Eckart as their supervisors. I would like to express my sincere gratitude to our project partner from Heriot Watt University, Dr N Hendrik Nahler for his contributions in the project.

My sincere thanks go to all the master students who have contributed to this project: Jack Eardley for starting building the experiment from scratch, Pedro Taylor-Burdett for optimising the LIF optics, Augustus Anthony for building the breath sampler, Joseph Landes for performing the CFD simulations. Without their work, we would not have gotten far in the time given.

My sincere thanks also go to my friend and colleague Dr Arin Mizouri, for her work towards the validation of the CELIF instrument and for her precious support throughout this research. She taught me plenty, and it was a pleasure to work alongside her.

Special thanks go to the electronics workshop supervisor in the department of chemistry, Dr Bryan Denton for building the various electronic parts needed for the project, especially the analog integrator. I am grateful to everyone else in both mechanical workshops in the departments of chemistry and physics, for all of the

parts that were built for the experiment.

I would like to thank all the members of the Quantum Light and Matter group in the department of physics for their moral support and for their questions during the group meetings which helped me to widen my research from various perspectives.

I would now like to thank all of my family who supported me through these challenging years. My journey companions: my husband Mohammed and my smart daughter Jood, for their continuous love, support, patience and all the beautiful days we have had in Durham. I cannot imagine going through the PhD journey without them.

My biggest gratitude goes to my parents: Ahmed and Aneesa, for their unconditional love, support and for making me who I am now. Without their support and prayers I would not have got this PhD. I am very grateful to my beloved sisters: Shaikha, Huda, Eman, Alanoud, Alhanoof and Alreem, and my beloved brother Abdulaziz for their love and for supporting me spiritually throughout my PhD.

Last but not least, I would like to thank all of my friends who I met in Durham, for all the fun we have had in the last five years. My life in Durham would not have been easy without them.

Dedicated to

My parents: Aneesa and Ahmed,

my husband Mohammed and my daughter Jood,

my sisters and brother.

Chapter 1

Introduction

1.1 Breath Gas Analysis

Human breath gas analysis for non-invasive disease diagnosis has gained high research interest since the discovery in 1971 that hundreds of volatile organic compounds (VOCs) are present in normal human breath [1]. Breath studies showed that normal human breath contains more than $1,000$ breath compounds between a few atmospheric molecules, such as H_2O, CO_2, N_2, O_2 in high concentrations, inorganic compound, such as ammonia and nitric oxide and several major VOCs arising from normal body metabolism, such as isoprene and acetone at part per million (ppm) or sub ppm levels and several hundreds of VOCs at part per billion (ppb) or part per trillion (ppt) levels [2, 3]. Many exhaled VOCs reflect the physiological conditions, and some VOCs have been established as biomarkers for specific diseases. For example, altered concentrations of isoprene in human breath is related to blood cholesterol levels, and increased breath acetone levels and odour is associated with abnormal metabolic status, such as diabetes [4–6].

1.2 Diabetes and Diabetic Ketoacidosis

Diabetes is a common life-long health issue. It is a metabolic disorder that affects blood glucose levels. It occurs when the body lacks insulin, a hormone produced by the pancreas, which allows the body to use glucose as a source of energy. There

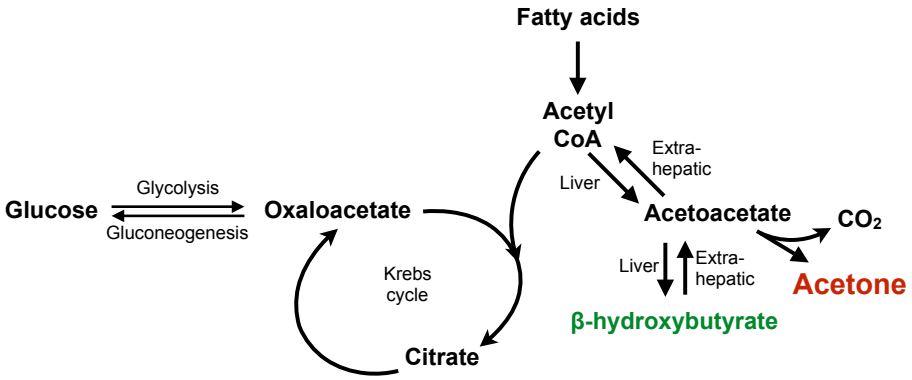

Figure 1.1: Generation of acetone in the liver via decarboxylation of acetoacetate.

are two main types of diabetes, type 1 diabetes (T1D) and the most common type of diabetes, type 2 diabetes (T2D). T1D results from the failure of the pancreas in producing insulin, and usually occurs suddenly at young ages. T2D results from the shortage in insulin production, or when the cells don't react to insulin, and tends to develop gradually in adults. The main symptoms of diabetes are feeling thirsty, tiredness, frequent urinating, blurred vision and slowly healing cuts and wounds. It is important to diagnose diabetes as early as possible to reduce the risk of its complications if left unmanaged. The complications of diabetes can affect a wide variety of parts of the body including eyes, heart, kidneys, nerves and feet. The most dangerous complication of diabetes is diabetic ketoacidosis [7].

Diabetic ketoacidosis (DKA) is a life threatening complication of T1D that could lead to organ failure, brain damage, and is the most common cause of death in children who have type 1 diabetes. It occurs when the body is unable to allow enough glucose to enter cells due to a severe lack of insulin. As an alternative source of energy the body switches to burning fatty acids. This causes a formation and a build-up of by-products, acidic ketone bodies: β-hydroxybutyrate (BHB) and acetoacetate. The latter decomposes into acetone by decarboxylation as illustrated in figure 1.1. Acetone, which is a small volatile compound, diffuses easily from the blood into the lungs, leading to elevated concentrations of acetone in exhaled breath [4, 6].

1.2.1 DKA Diagnosis, Management and Treatment

Historically, diabetic ketoacidosis has been diagnosed and managed by urine acetoacetate testing with laboratory measurement of blood bicarbonate or pH to confirm the diagnosis. Blood BHB predominates in diabetic ketoacidosis and correlates with the degree of acidosis. It can be detected in blood before detecting acetoacetate in urine. Blood BHB testing allows more rapid diagnosis of diabetic ketoacidosis, thus offering potential advantages of blood BHB over urine testing in timely ketone detection and in management of ketoacidosis [8].

The National Institute for Health and Care Excellence (NICE) published guidelines for the diagnosis and management of diabetic ketoacidosis in children and young people [9]. It reported that children and young people taking insulin for diabetes may develop DKA with normal blood glucose levels. It recommends measuring the blood BHB when DKA is suspected in a child or young person with known diabetes. The blood measurement should be made using a near-patient method if available, or measuring urine ketones if it is not. If the level of ketones is elevated, it recommends sending the patient immediately to a hospital with acute paediatric facilities.

DKA is diagnosed in children and young people with diabetes who have acidosis (indicated by blood pH below 7.3 or plasma bicarbonate below 18 mmol/L) and ketonaemia (indicated by blood BHB above 3 mmol/L). When DKA is diagnosed in a child or young person in hospital, the NICE guideline recommends measuring the capillary or venous pH and plasma bicarbonate. The guideline recommends considering a near-patient blood BHB testing method for rapid diagnosis and monitoring of DKA in children and young people in hospital.

The NICE guideline recommends treating DKA with oral fluids and subcutaneous insulin only if the patient is alert, and not clinically dehydrated, otherwise it recommends starting treating DKA with intravenous fluids, and starting an intravenous insulin infusion 12 hours after beginning intravenous fluid therapy. To ensure that the patient is recovering, it is recommended to monitor the patient for resolution of acidosis after 2 hours from starting treatment, and then at least every 4 hours, carrying out blood glucose, blood pH and blood BHB tests.

The recommended dosage of insulin is 0.05 units/kg/hour. If the blood BHB

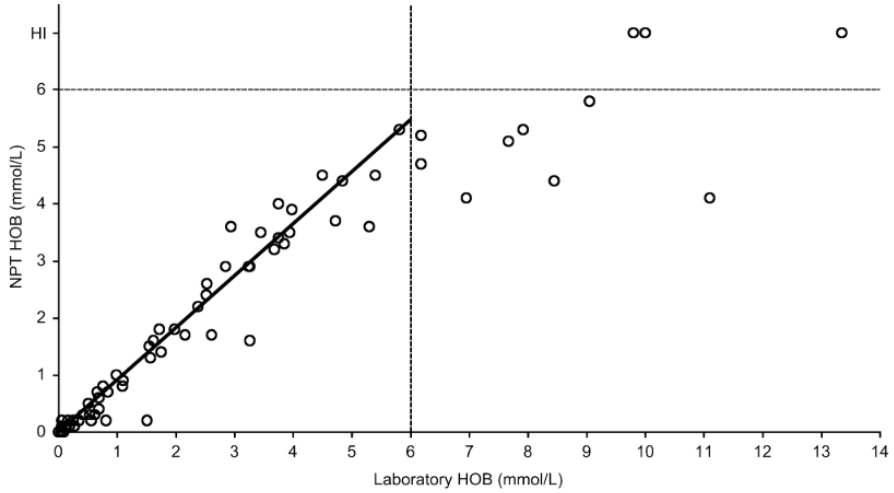

Figure 1.2: Comparison between NPT and laboratory blood BHB from patients with DKA. The dashed lines show the analytical range of the meter (6 mmol/L). Taken from [10].

level is not falling within 6-8 hours in a child or young person with DKA, the guideline recommends increasing the insulin dosage to 0.1 units/kg/hour or greater. So far, there is no known optimal dosage of intravenous insulin for managing diabetic ketoacidosis in children and young people, and the rate of DKA resolution is not known. There is a concern that larger dosages are associated with an increased risk of cerebral oedema, a complications of diabetic ketoacidosis. Large clinical trials are still needed to undertake a comparative study of different insulin dosages.

1.2.2 Breath Acetone as an Alternative for DKA Management

To date, DKA is managed by frequent measurement of the blood BHB. These measurements need to be made up to ten times per day to adjust the dose of insulin needed for treatment. Frequent taking of blood samples, especially for children, is intrusive, invasive and physically painful. Furthermore, the near-patient test (NPT) (Abbott Diabetes Care Ltd., UK, FreeStyle Optium) measures blood ketones in the form of blood BHB. The clinical application of this NPT was assessed for capillary blood BHB measurement in the monitoring of DKA. As shown in figure 1.2, there was clinically acceptable agreement between the meter and laboratory

blood BHB measurements when laboratory BHB was < 6 mmol/L (i.e., within the meter's analytical range). However, the NPT lacked accuracy when plasma BHB was > 6 mmol/L; the meter gave results much lower than the laboratory BHB [10]. The NPT BHB value at presentation will not be suitable to indicate the degree of severity of DKA, as DKA patients are more likely to have BHB level of more than 6 mmol/L. The NPT has a readout precision of 0.1 mmol/L, and thus the measurements could have a relatively substantial uncertainty in BHB values [11].

Previous studies showed that breath acetone levels are predictive of blood BHB levels and a significant relationship was found between the two in T1D patients [11–13]. The results of these studies suggest a potential to develop a non-invasive breath acetone analyser to provide an alternative to blood testing for ketone measurement to assist with the management of T1D and DKA.

Many groups have done historical reviews on measuring breath acetone as a potential biomarker of diabetes and DKA. The reader is referred to read these reviews for more detail [3–6, 14].

Most breath measurements on people with type 1 diabetes have been carried out on relatively small cohorts, with relatively few measurements on children. Sun *et al.* monitored breath acetone and blood BHB in 20 type 1 diabetic outpatients (adults) over 30 days [13]. Blood BHB levels of the patients were measured, then within 5 minutes breath samples were collected in breath bags, then the breath measurements were carried out using a ring-down breath acetone analyzer. The study confirmed that type 1 diabetic patients have elevated mean breath acetone concentrations as compared to the controls. It showed a weak correlation between the individual mean breath acetone and the individual mean blood BHB measured in the 20 T1D outpatients. However, the group mean breath acetone concentrations were grouped into six groups based on different blood BHB levels. A strong correlation between the group mean breath acetone and the group mean blood BHB has been found. The highest individual mean breath acetone concentration in this study was 7.3 ppm, with a mean blood BHB of 0.3 mmol/L. in one of the 30 days, this patient's breath acetone concentration reached 49.5 ppm, corresponding to blood BHB of 4.3 mmol/L.

Another study by Blaikie *et al.* showed the predictive nature of blood BHB by the breath acetone in children and adolescents with type 1 diabetes [11]. End-tidal breath samples from 113, well-controlled, type 1 diabetic patients (age 7–18 years) were collected in breath bags during a routine visit to a clinic and analysed the by means of a soft-ionization mass spectrometer. At the same time, the patients provided blood samples for BHB measurements. The comparison between the two measurements showed a significant relationship between breath acetone and blood BHB. However, the patients in this study had relatively low concentrations of BHB (0-0.4 mmol/L).

Thus, these studies must be extended, and the correlation between breath acetone and blood BHB has to be confirmed in children diagnosed with DKA, and thus presenting with BHB levels considerably above 0.4 mmol/L. A larger number of children with a wider age range should be considered in these studies. The study by Sun *et al.* did not include any child, and the patients age range in the study by Blaikie *et al.* was restricted by the ability of the children to blow reliably through a tube to collect the breath sample, thus did not include any child below 7 years old.

1.3 Breath Sampling and Breath Phases

There are no accepted standardized methods until now for direct (on-line) or indirect (off-line) VOC breath-gas sampling and analysis. In off-line sampling, breath gas is collected and stored in a container such as a bag, canister or compound trap and analysis is carried out some time later after the sample has been brought to the analytical instrument. The benefit of this technique is enabling sampling to be carried out near the patient, which is essential when the instrument cannot be brought to the patient or vice versa. However, there are risks involved in off-line sampling, primarily relating to sample stability during handling and storage. For example, degradation of the compound concentration caused by diffusion of the compound through the container walls, or by condensation of breath water vapour at room temperature which could lead to more compound losses. Furthermore, the cleanliness of the storage container is critical in off-line sampling and must be

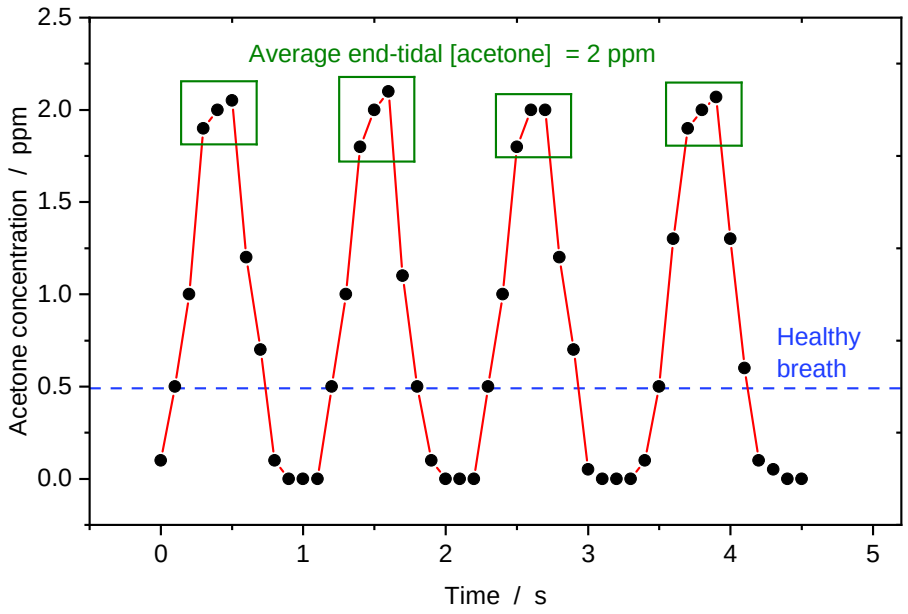

Figure 1.3: Representation of breath-cycle resolved acetone concentration in a diabetic patient, showing an average end-tidal acetone concentration of 2 ppm.

suitably controlled to avoid false signals.

On-line breath sampling and analysis offers several advantages over off-line analysis of stored samples. On-line sampling is achieved when the exhaled breath is directly transferred into the inlet and subsequently the detection unit of the analytical instrument. On-line sampling and analysis requires the real-time capability of the detection system employed, a fast response time and direct analysis without the need for sample pre-treatment [15, 16].

Breath is a combination of gases from the upper and lower airways. As shown in figure 1.3, a single exhalation can be broken down into three phases, each reflect different fractions of breath: a brief initial phase containing dead-space gas from the oral cavity and trachea; a mixed expiratory phase in which gas from the lungs mixes with and purges the dead-space; and an end-tidal, or expiratory plateau phase that reflects alveolar gas in the lungs.

The choice of which fraction of breath to sample depends on the compound under investigation. During tidal breathing, saturation of the air stream with acetone occurs almost in the alveoli. Here, the end-tidal plateau of an exhalation provides the richest, highest concentration gas sample for analysis [17]. Continuous measure-

ments of the acetone present in all the different phases (breath-cycle resolved) could be achieved using an on-line, real-time, fast response instrument.

1.4 The Techniques Used in the Measurements of Breath Acetone

Measuring breath acetone concentration has been a topic of interest for many years. Due to the large number and low concentrations of trace compounds in exhaled breath, breath acetone detection and measurement require a highly sensitive and a highly selective instrument. Several reviews covering breath gas analysis techniques are available in the literature [3, 4].

Several breath analysis methods are currently employed for exhaled VOCs detection and analysis, ranging from mass spectrometry to laser-based spectroscopy and electrochemical sensors. The most widely used analytical tool is mass spectrometry, such as gas chromatography mass spectrometry, GC-MS. GC-MS instruments have detection sensitivity down to parts per billion (ppb) levels. However, they are very large, laboratory-based, do not allow online sampling (i.e., exhaling directly into the instrument without sample pre-treatment) and have a long analysis time. Thus, GC-MS technique is unsuitable for real-time and online breath acetone monitoring [18, 19].

Many electrochemical sensors have been reported for breath acetone measurements [20–22]. These are cost-effective, compact and could be sensitive. However, they have long response and recovery times, which are in the order of tens or hundreds of seconds. Furthermore, some electrochemical sensors require significantly higher than room temperature conditions ($200 - 300\,^{\circ}\mathrm{C}$) for optimal performance. The main drawback of the electrochemical sensors is the poor selectivity for breath acetone. These drawbacks restrict their applications in breath acetone monitoring.

Extensive research has been conducted to develop alternative breath analysis methods that can be used to perform online, real-time (sub-second time resolution and breath-cycle resolved) detection, sensitive, analysis, preferably for many volatile compounds simultaneously. Proton-transfer reaction mass spectrometry (PTR-MS)

[23] and selected ion flow-tube mass spectrometry (SIFT-MS) [24,25] are examples of online, real-time mass-spectrometric methods currently employed in breath analysis.

SIFT-MS is a relatively new analytical technique for online, real-time quantification of several trace gases simultaneously in air or exhaled breath. It relies on chemical ionization of the trace gas molecules introduced into fast-flowing helium carrier gas using a chosen precursor ion (either H_3O^+, NO^+, or O_2^+), selected by a quadrupole mass filter from a mixture of ions generated in a microwave discharge and injected into the fast-flowing helium carrier gas. Reactions between the precursor ions and trace gas molecules proceed for an accurately defined time. A downstream mass spectrometer rapidly detects and counts the precursor and product ions to observe the temporal variations in the concentrations in the chosen molecules. The ambient air at the SIFT-MS entry port is displaced by directly exhaled breath removing the need for breath sample collection [18, 26, 27]. Despite the advantages of the SIFT-MS and similarly the PTR-MS, these instruments are very expensive, very large and require a lot of expertise.

Compared to the electrochemical sensors and the online mass spectrometry, laser spectroscopy-based techniques can provide an accurate and precise quantitative analysis, with cost-effective, compact instruments that do not necessarily require an expert user. Various laser spectroscopy-based techniques have been applied for detection of breath acetone [28–32].

For example, Sun *et al.* reported a fully integrated, standalone, portable breath acetone analyzer based on the cavity ring-down spectroscopy technique (CRDS) for near-real time measurements [32]. In a typical CRDS experiment, a laser pulse is injected into an optical cavity that is formed by a pair of highly reflective mirrors. The small amount of light that is trapped inside the cavity reflects back and forth between the two mirrors, with a small fraction of the intensity transmitting through each mirror with each reflection, increasing the effective path length of the light inside the cavity to thousands of kilometers. The resultant transmission of the circulating light is monitored behind the cavity exit mirror as a function of time, allowing the decay time of the cavity to be determined. The time required for the intensity exiting the cavity to decay to 1/e of the intensity of the initial output

pulse is called the cavity ring-down time, (τ_0). If an absorbing medium is placed inside the cavity the ring-down time will be reduced to (τ). From the measured difference between τ_0 and τ, the frequency-dependent absorption coefficient α can be calculated as

$$\alpha = \rho\sigma = \frac{1}{c}\left(\frac{1}{\tau} - \frac{1}{\tau_0}\right)\frac{L}{d}, \tag{1.4.1}$$

where, ρ is the number density of the sample inside the cavity, σ is the absorption cross section, c is the speed of light, L is the cavity length and d is the sample length [33]. CRDS is a simple, sensitive technique which offers absolute density measurement capability, and independence from pulse-to-pulse fluctuations of the laser intensity.

Sun *et al.*'s instrument features a 50 cm optical cavity and a Q-switched Nd:YAG laser operated at 266 nm with a repetition rate of 1 kHz. A theoretical acetone limit of detection (LOD) of the analyzer was estimated to be 57 ppb based on the ring-down baseline stability, which was estimated by averaging over 100 ring-down events for 30 minutes. A subject is required to exhale a single deep breath via a disposable mouthpiece into a breath collection bag which is then connected to the device.

Blaikie *et al.* have demonstrated a compact device for measuring breath acetone at sub ppm levels using diode laser cavity enhanced absorption spectroscopy (CEAS) [31]. CEAS is a modification of CRDS technique. It is based on off-axis arrangement of the optical cavity. In this configuration, the light is repeatedly reflected by the mirrors, however, the reflection points are spatially separated. CEAS is based on detection of the time-integrated intensity of the light passing through the cavity, rather than cavity ring-down time [33, 34].

Blaikie *et al.*'s device features a 7 cm long high-finesse optical cavity that is coupled to a miniature adsorption pre-concentrator. Breath samples are either collected in breath bags which are then connected to the device or sampled directly through the device. Acetone is trapped out of breath and released into the optical cavity where it is probed by a near-IR diode laser operating at about 1670 nm.

Although both devices have appealing features for point-of-care and fast breath acetone measurements with detection limits below ppm levels, the sampling techniques in both instruments do not resolve breath cycles. Breath-cycle resolved sam-

pling adds significant advantages such as, resolving the different respiratory phases and continuous measurements of the acetone present in these different phases. The high precision, absolute accuracy, and breath-cycle resolved sampling allow much more data to be collected and very detailed biomarker studies to be performed.

Fast online sampling, combined with real-time detection, eliminates the need for collection and storage of breath samples, which constituted a potential source of errors because of the possible risk for dilution and contamination of the breath sample [3]. Furthermore, online sampling via direct normal breathing into the instrument is required especially for young children or unconscious patients, who are unable to provide single, deep exhalation.

The two examples of the laser spectroscopy-based instruments were not tested to measure acetone concentration of more than 25 ppm. It is likely that the upper limit of detection of these instrument does not cover the required range for DKA patients. Also, the sensitivity of the instruments depends on the high reflectivity of the cavity mirrors. The contamination of the cavity mirrors caused by using a large number of breath samples will result in minor degradation of the limit of detection.

1.5 Our CELIF Device Specification and Aims

The aim of this project is to build a non-invasive, online, real-time, mobile, cost-effective breath analyzer using cavity-enhanced laser-induced fluorescence technique (CELIF). The specification of our device are:

- The dynamic range of the device must cover the range of breath acetone concentrations in DKA patients (up to several thousand ppm) [35], as well as being able to measure breath acetone concentration in healthy individuals (0.49 ± 0.20 ppm) [2] to allow breath acetone measurements for the monitoring and management of DKA, and help to identify children with new diabetes before DKA supervenes.

- The device must be able to make a real-time, breath-cycle resolved acetone CELIF measurements. As represented in figure 1.3, this requires the ability to

make a CELIF measurement at least every 100 ms to detect all of the three breath phases, then select the end-tidal acetone concentration.

- The response time of the CELIF measurement of the device must be fast enough, (in the order of 0.5 s) to detect in real-time the end-tidal acetone concentration, then fall back to the background level before the next breath arrives.

- The device must have an on-line breath sampling capability.

- The device must be cost effective and mobile such that it can be available and brought next to each diabetic or DKA patient.

With our CELIF device, our aim is, in a large cohort of children and young people with type 1 diabetes, to test the breath acetone concentrations, together with blood BHB measurements, and to look for correlations between these variables together in each individual.

Although some studies confirmed a correlation between blood BHB and blood pH [9, 36], relying on blood pH measurement for DKA monitoring is not sufficient; as there might be other factors which lower the blood pH, such as drug-induced metabolic acidosis [37], exercise-induced acidosis due to lactate production after exercise [38] and diet-induced acidosis [39]. Furthermore, lactate acidosis in DKA patients, which is thought to be a result of inadequate tissue perfusion and oxygenation, contributes to the low blood pH levels in DKA patients [40]. Several studies have shown that blood pH could be measured non-invasively by near-infrared spectroscopy [41–43]. Others have developed a wearable technology that provides real-time insight into the human body by acquiring and analyzing physiological signals such as blood pH [44, 45].

Currently, as the correlation between breath acetone and blood BHB is not very clear, especially at high blood BHB levels as mentioned previously, the CELIF device alone will not replace the blood ketone monitoring tests, but a suite of non-invasive devices such as a non-invasive blood pH and blood bicarbonate measuring devices, along with our CELIF device could possibly eliminate the need for frequent blood testing.

1.6 The Scope of this Thesis

This thesis presents the work carried out towards the building of our CELIF device. The research carried out is structured as follows:

- Chapter two begins by discussing standard, well established detection techniques used to measure absolute densities in gas samples: laser-induced fluorescence (LIF) and cavity ring-down-spectroscopy (CRDS), followed by explaining the methodology of cavity-enhanced laser-induced fluorescence (CELIF), a cross-correlated combination of the two methods.

- Chapter three outlines the technical details of the CELIF device. In this chapter I described the CELIF experiment setup, including: the laser system, the optical cavity, the LIF optics, data acquisition using a home-built analog integrator and a digitizer card, and finally the Labview programs which were written to acquire and analyse the data.

- In chapter four, the CELIF measurements are described in detail. It included discussing static vs. flow CELIF measurements, different flow-body designs and performance, computational fluid dynamic (CFD) simulations, the response time of the CELIF measurements and finally the validation of the CELIF instrument against the SIFT-MS.

- Chapter five presents the breath acetone measurements made with our home-built buffered end-tidal breath sampler.

- Chapter six presents the acetone CELIF measurements made with a high pulse energy laser, to explore the ability to expand the CELIF dynamic range.

- Finally, the thesis is concluded in chapter seven with a summary of all the findings. An outlook, including the plans of the CELIF device are also outlined.

Chapter 2

CELIF Methodology

2.1 Acetone Absorption and Fluorescence

There are three electronic states involved in the photoemission processes in acetone: the ground state singlet S_0, the first excited singlet S_1, and the first excited triplet T_1. Each electronic state includes a manifold of vibrational levels. Acetone absorption corresponding to excitation from S_0 to S_1 depends on temperature and excitation wavelength [50]. At atmospheric pressure and room temperature, acetone has a broadband absorption feature that extends from 225 to 320 nm with a flat region between 270 and 280 nm, as shown in figure 2.2. The absorption in this region corresponds to the transition from the non-bonding (n) orbital in the carbonyl group (C=O) in acetone (CH_3COCH_3), to the anti-bonding orbital (π^*) for the C=O group, where there is a destructive overlap of the p orbitals in the C=O group [52]. This broadband absorption spectrum suggests several possible excitation sources for pumping acetone. This includes a commercially available, frequency-quadrupled Nd:YAG laser at λ= 266 nm, where the acetone absorption cross section $\sigma = 4.4 \times 10^{-20}$ cm^2 [47].

Following a UV laser excitation of acetone molecules from the ground electronic state, S_0, to the first excited singlet state, S_1, the S_1 state can decay through several intramolecular photophysical mechanisms as illustrated in figure 2.1. The radiative processes include emission of fluorescence via the deexcitation from the S_1 to the S_0 states. The non-radiative processes include internal conversion (IC) from S_1 to

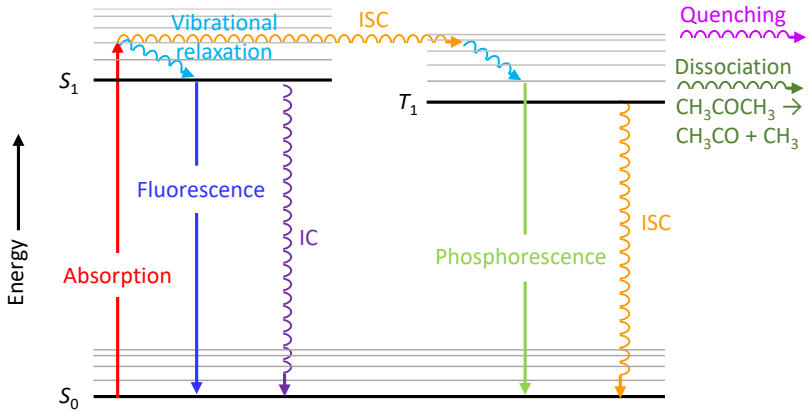

Figure 2.1: Jablonski diagram illustrating the radiative (straight lines) and non-radiative (wavy lines) processes in acetone following light absorption [46–49].

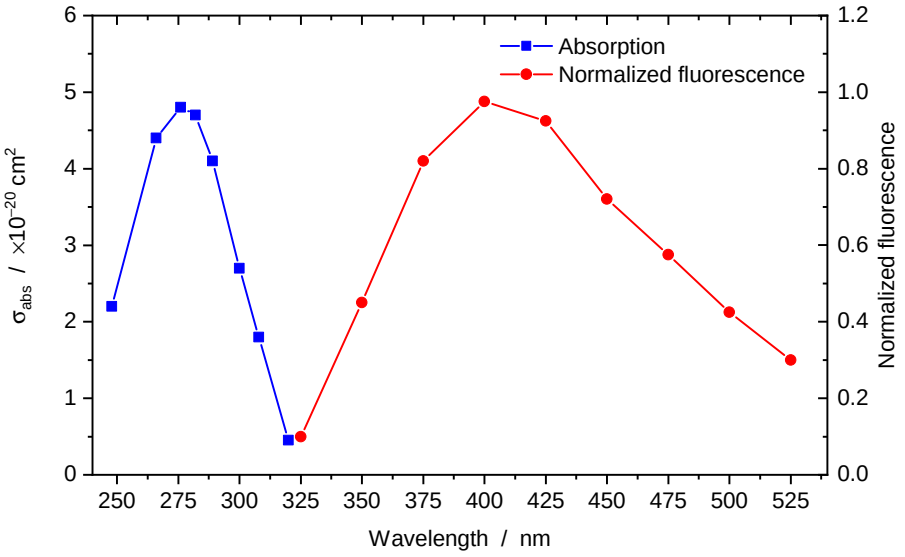

Figure 2.2: The blue curve is the absorption spectral profiles of acetone [50], and the red curve is the fluorescence emission spectrum of acetone after excitation at 266 nm [51]. Both were measured at 23 °C.

S_0, intersystem crossing (ISC) from S_1 to T_1 or from T_1 to S_0, collisional quenching and dissociation. The low fluorescence and phosphorescence quantum yields at all excitation wavelengths implies that the nonradiative processes dominate. The dominant nonradiative path for acetone singlets is the ISC from S_1 to T_1, with estimated branching fraction reaching unity at excitation wavelengths $\lambda < 306$ nm. The acetone molecules $(CH_3)_2CO$ dissociate on the T_1 surface to produce CH_3 and CH_3CO radical products. At energies below the triplet barrier, ISC from T_1 to S_0 becomes the only available pathway, other than phosphorescence and recrossing to S_1. The former has a very small quantum yield (< 0.01), while the latter is unlikely [46–49].

The wavelength-integrated fluorescence is detected (generally at 90° to the laser beam) leading to a molecular fluorescence excitation spectrum that is directly linked to the absorption spectrum by the fluorescence quantum yield. The acetone fluorescence yield at 266 nm excitation, room temperature and atmospheric pressure is 0.13 % [50]. The acetone fluorescence emission spectrum after excitation at 266 nm at room temperature was measured by Bryant *et al.* and is shown in figure 2.2 [51]. The fluorescence spectrum is red shifted from the absorption spectrum, because of the vibrational relaxation at the S_1 state before decaying to the S_0 state as shown in figure 2.1. The LIF spectrum is broadband, extending from 350 to 550 nm with a peak at 410 nm. Ossler and Alden measured the effective acetone fluorescence lifetime between 1–1.5 ns at atmospheric pressure of air and nitrogen at room temperature when excited at 266 nm [53].

An absolute measurement of absorbance by laser-induced fluorescence (LIF) requires detailed knowledge of the fluorescence process and meticulous calibration of the detection system (fluorescence quantum yield, geometrical setup, spectral response of the detector, etc.). Because of the calibration challenges, LIF is predominantly used to measure relative rather than absolute quantities.

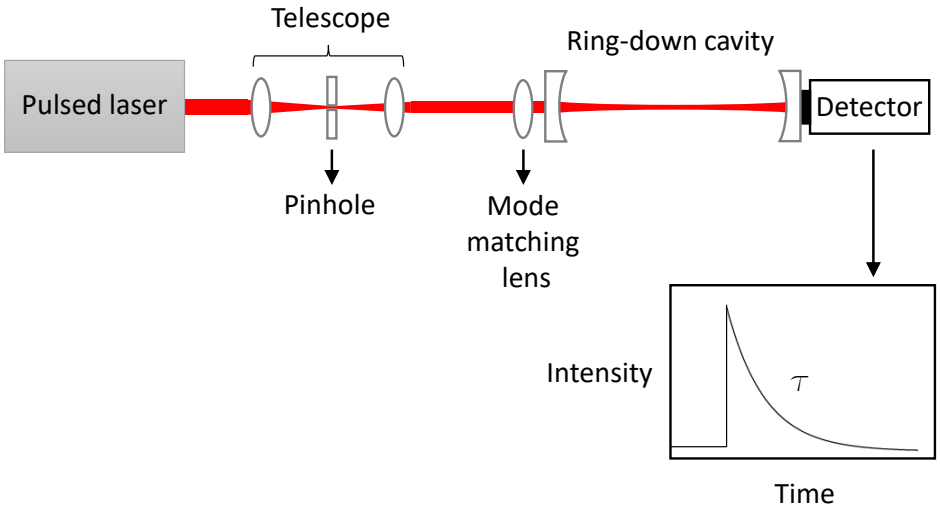

Figure 2.3: A schematic drawing of a typical CRDS setup.

2.2 Cavity Ring-Down Spectroscopy

Cavity ring-down spectroscopy (CRDS) is a direct absorption technique based on the Beer-Lambert law [54, 55]. Figure 2.3 shows a schematic of a typical CRDS apparatus. A typical setup consists of a pulsed laser source, an optical cavity with coupling optics, and a photo-detector. A stable optical cavity is formed by two concave mirrors of high reflectivity (typically $R > 0.999$). These mirrors serve also as the side windows of the sample gas chamber. A laser pulse enters the cavity through one of the mirrors. The pulse is spatially shaped via a pinhole to form a TEM_{00} mode of the cavity. It then circulates inside the cavity, reflecting back and forth. During each pass, a small fraction of light leaks out through the cavity exit mirror. The light intensity exiting the cavity will decay with an exponential time profile according to:

$$I(t) = I_0 \exp\left(-t/\tau_0\right), \tag{2.2.1}$$

where, τ_0 is the empty cavity ring-down time, the time for the intensity to decay to 1/e of its original value. τ_0 is given by

$$\tau_0 = \frac{d}{c(1-R)}, \tag{2.2.2}$$

where d is the distance between the cavity mirrors of reflectivity R and c is the speed of light. Thousands of round trips can be achieved, giving an effective path length

of kilometers. The existence of a sample inside the cavity causes an additional loss and consequently speeds up the decay and gives a shorter ring-down time, τ. For a sample filling the entire length of the cavity, τ is directly linked to the absorption coefficient

$$\alpha = \sigma\rho = \frac{1}{c}\left(\frac{1}{\tau} - \frac{1}{\tau_0}\right), \tag{2.2.3}$$

where, σ is the absorption cross section and ρ is the number density of the sample. Measuring the ring-down decay time removes any shot-to-shot fluctuations of the incident pulse intensity because the decay time constant is independent of the laser intensity, leading to a high sensitivity absorption measurement.

The ring-down time measurement is sensitive to the temporal shape of the ring-down decay, which depends on the mode coupling of the laser beam into the cavity, the stability of the mirror alignment, and the electronic noise of the detection system.

The lowest absorbance that can be measured with CRDS needs to cause a statistically significant change in the ring-down time. At the other end, CRD measurements are not valid any more when large absorbances lead to very short ring-down times. A typical pulsed UV/vis CRD measurement spans two to three orders of magnitude in the dynamic range [54].

The limit of detection of a CRD measurement is estimated from the minimum distinguishable difference between τ and τ_0, and is calculated from 3 standard deviations (3σ) of τ_0 as:

$$\rho_{\mathrm{LOD}}^{3\sigma} = \frac{1}{c\sigma}\left(\frac{3\,\delta(\Delta\tau)}{\tau_0\,\tau}\right), \tag{2.2.4}$$

where $\Delta\tau = \tau_0 - \tau$, and $\delta(\Delta\tau)$ is the error in $\Delta\tau$. At the limit of detection, $\tau \approx \tau_0$, thus, the number density at the limit of detection is

$$\rho_{\mathrm{LOD}}^{3\sigma} = \frac{1}{c\sigma}\left(\frac{3\sqrt{2}\,\delta\tau_0)}{\tau_0^2}\right). \tag{2.2.5}$$

The requirement for CRDS to be applicable as a quantitative diagnostic is for the light inside the cavity to obey the Beer-Lambert law, which means fulfilling the conditions for exponential decay of the light intensity [55]. Beer-Lambert behaviour requires that the widths of the absorption spectral lines are greater than the linewidth of the laser light within the cavity. If the linewidth of the light exceeds the width of the absorption line, the absorption coefficient is not constant and

non-exponential decay can result. This is not the case in our experiment because acetone has a very wide absorption feature, as shown in figure 2.2, which is wider than the 2 cm^{-1} bandwidth of our 266 nm ND:YAG laser.

The frequency spacing of the longitudinal modes of the cavity (the cavity free spectral range, $\Delta\nu$) depends on the round-trip time, t_r, of light within the cavity (and hence the separation of the cavity mirrors, d) according to :

$$\Delta\nu = \frac{1}{t_r} = \frac{c}{2d}.$$

$\Delta\nu$ must not exceed the width of the spectral feature being studied, and the range of the frequencies covered by the cavity longitudinal modes must be narrower than the absorption line so that the coefficient describing the absorption may be treated as constant over the mode structure frequencies. If $\Delta\nu$ exceeds the widths of the spectral features being studied, light of the appropriate frequency for excitation of certain spectral lines will not be injected into the cavity. Excitation of a single longitudinal cavity mode will result in exponential decay of the light intensity within the cavity. If more than a single longitudinal mode is excited in the cavity, beats between the modes occur at the cavity output which may cause modulation of the continuous decay waveform. However, this mode beating is much faster than the decay time of the exponential and hence washes out significantly after the decay waveform is averaged over several laser pulses.

The optical cavity used in our CELIF experiment setup is 53 cm long. The longitudinal mode spacing, $\Delta\nu$, is 283 MHz (≈ 0.01 cm^{-1}), which is much narrower than the acetone absorption feature shown in figure 2.2. The bandwidth of our laser is 60 GHz (= 2 cm^{-1}), which exceeds the cavity longitudinal mode spacing. This means that in our cavity at least 212 cavity longitudinal modes are spanned.

The round trip time of the laser pulse inside the cavity $t_r = 3.5$ ns, which is longer than the laser pulse width, $t_p = 1.5$ ns. Therefore, when the light is coupled into the cavity the front end of the pulse does not overlap the rear end propagating in the same direction, and the intensity pattern of the cavity output consists of a train of pulses of decreasing intensity, with a single exponential envelope. If the input pulse width is longer than the cavity round-trip time, these pulses overlap and give a continuous decay waveform.

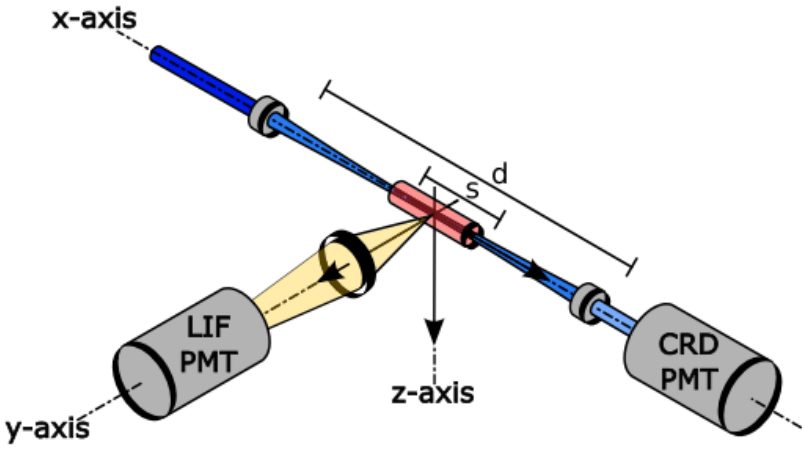

Figure 2.4: Schematic diagram of a typical setup of a CELIF experiment. The fluorescence is collected at a right angle from the ring-down cavity axis. d is the distance between the mirrors and s is the length of the sample.

For experiments in which the laser light pulse is not carefully shaped to match the lowest order, Gaussian TEM_{00} mode of the cavity, or is not injected perfectly axially into the cavity, transverse cavity modes will be established that have frequencies lying between those of the longitudinal cavity modes. For a cavity excited on numerous transverse cavity modes, the light emitted from the cavity can experience temporal interference because of beating between the slightly different decay rates of the separate TEM_{mn} modes. This mode beating can lead to non-exponential decays, which makes CRDS not applicable, or it can lead to oscillatory structure superimposed on the decay envelope, which can be averaged out in the fitting or filtered out electronically using a bandwidth limit.

Excitation of higher transverse modes can be suppressed by "mode-matching", which means to shape the input beam so that it closely matches the size and radius of curvature of the TEM_{00} mode of the cavity. This requires a telescope, spatial filter and a mode matching lens. Collection of the entire cross-section of the beam at the detector is important to suppress transverse mode beating effects.

2.3 CELIF Methodology

Recently, a new method called cavity-enhanced laser-induced fluorescence (CELIF) has been developed by Sanders *et al.*, and then tested by measuring the absolute absorption coefficient of 1,4-bis(phenylethynyl)benzene (BPEB) [54]. CELIF is a direct combination of LIF and CRDS that employs a single pulsed laser beam inside the optical cavity interacting with the same sample for both the fluorescence and ring-down measurements. A schematic layout of the CELIF setup is shown in figure 2.4.

The term "cavity-enhanced" is used in the broader sense of the definition, *i.e.* concerning the increased interaction time between light and matter which corresponds to an effective interaction length of thousands of passes [56]. Assuming a small fractional absorption, through the repeated use of the light pulse inside the cavity, the integrated light intensity creating the LIF signal in a CELIF experiment is $I_n T/(1-R)$, where I_n is the laser intensity incident on the cavity entrance mirror, T and R are the intensity transmission and reflectivity of the mirror respectively. In a single-pass pulsed LIF experiment, the fluorescence signal is created by the full intensity of the probe laser, I_n. Therefore, the total light intensity in both techniques differs only by the factor $T/(1-R)$. Sanders *et al.* obtained $T/(1-R) = 0.4 \pm 0.2$. Consequently, the light available to invoke S^{LIF} in our CELIF setup is 40% of the light available in an equivalent single-pass LIF measurement. Therefore, in terms of number of photons interacting with the sample, CELIF and single-pass pulsed LIF are comparable.

The transients from the LIF and CRD detectors are recorded simultaneously on a shot-to-shot basis. The detected fluorescence is normalized by the time-integrated ring-down transient to compensate for fluctuating laser intensities. The simultaneous cavity ring-down time measurement provides the robust calibration of the fluorescence measurement without the requirement of any external calibration. The high sensitivity of LIF greatly extends the accessible dynamic range of CRDS and allows the measurement of absolute absorption coefficients several orders of magnitude below the limit of detection (LOD) of pulsed UV/vis CRDS with a much increased dynamic range. Unlike CRDS, the CELIF measurements are unaffected

by the shape of the CRD transients due to the robust shot-to-shot normalization that automatically compensates for the varying amount of light coupled into the cavity.

In a CELIF measurement, the following three quantities are extracted from the simultaneously recorded CRD and LIF transients: the ring-down time, τ, the time-integrated ring-down transient, S^{CRD}, and the time-integrated fluorescence transient, S^{LIF}. The latter two are a measure of the amount of light incident on the respective detectors.

2.3.1 CRD and LIF Signals

The CELIF methodology has been described in detail by Sanders *et al.* [54]. The detected fluorescence, S^{LIF}, is proportional to the light intensity, I_{L}, that has interacted with the sample within the LIF probe volume,

$$S^{\mathrm{LIF}} = \alpha \cdot \Gamma \cdot g^{\mathrm{LIF}} \cdot I_{\mathrm{L}}\,, \tag{2.3.6}$$

where Γ is the fluorescence quantum yield, and g^{LIF} is a geometry dependent factor of the detection system, *i.e.* g^{LIF} is the product of the fraction of fluorescence photons created in the probe volume that hit the LIF photomultiplier tube (PMT), the quantum efficiency of that PMT and a factor quantifying the convolution of the detection system solid angle with the angular distribution of the fluorescence or light scattering process. In order to obtain the absorption coefficient, α, from a fluorescence excitation measurement, S^{LIF} and I_{L} need to be measured. The factor g^{LIF} is not readily available but can be determined via a meticulous external calibration. The fluorescence quantum yield, Γ, is generally unknown and needs to be measured or predicted from theory.

It was shown that the time-integrated CRD transient, S^{CRD}, is correlated to I_{L} and is used to provide the normalization of S^{LIF} to eliminate shot-to-shot fluctuations in the laser intensity from Eqn 2.3.6. Furthermore, the absolute absorption coefficient determined from the ring-down time [Eqn 2.2.3] is used for the absolute calibration of the normalized LIF measurement such that in a CELIF measurement, prior knowledge of g^{LIF} and Γ is not required.

For highly reflective mirrors (R $\approx$ 100%) and low photon loss per cavity pass $\alpha d \ll 1$, S^{CRD} can be approximated as

$$S^{\mathrm{CRD}} \approx g^{\mathrm{CRD}} \cdot \frac{T}{2} \cdot I_{\mathrm{L}}, \tag{2.3.7}$$

where g^{CRD} is the detection efficiency of the CRD PMT (quantum efficiency and gain—not included in Sanders *et al.* [54]) and T is the transmission of the cavity mirrors. We define a calibration factor

$$\mathcal{K} = \Gamma \cdot \frac{g^{\mathrm{LIF}}}{g^{\mathrm{CRD}}} \cdot \frac{2}{T} \tag{2.3.8}$$

that links the time-integrated CRD transient, S^{CRD}, directly to the detected fluorescence:

$$S^{\mathrm{LIF}} = \alpha \cdot \mathcal{K} \cdot S^{\mathrm{CRD}}. \tag{2.3.9}$$

Acetone has a very small fluorescence quantum yield [50], and in our acetone CELIF experiment the acetone photon-counted LIF signals are close to the background levels. The total detected fluorescence, $S^{\mathrm{LIF}}_{\mathrm{tot}}$, will include background contributions:

$$S^{\mathrm{LIF}}_{\mathrm{tot}} = \alpha \mathcal{K} S^{\mathrm{CRD}} + \beta S^{\mathrm{CRD}} + \gamma. \tag{2.3.10}$$

βS^{CRD} accounts for background that depends on the light (laser) intensity, *e.g.* stray light or fluorescence of the mirrors. γ is laser-independent background, *e.g.* PMT dark counts and leaked ambient light.

2.3.2 CELIF Calibration

Eqn 2.3.10 forms the basis of the calibration of the CELIF setup. Note that S^{CRD} depends on the ring-down time, τ, which in turn depends on α:

$$\frac{1}{\tau} = \frac{1}{\tau_0} + \alpha c, \tag{2.3.11}$$

$$S^{\mathrm{CRD}} = \frac{S^{\mathrm{CRD}}_0}{1 + \alpha c \tau_0}, \tag{2.3.12}$$

in which τ_0 is the reference ring-down time without sample (signal blank), S^{CRD}_0 is the time-integrated CRD transient without sample and c is the speed of light. Eqn 2.3.12 is the theoretical dependence of S^{CRD} on α and will only be satisfied

if sufficiently averaged due to shot-to-shot variations of the incident laser intensity and the amount of light coupled into the cavity.

Ideally, $S_{\text{tot}}^{\text{LIF}}$ should be measured as a function of sample density, ρ, to change α. The unknown constants $\mathcal{K}$, β and γ can be determined by fitting the measured values of S^{LIF} as a function of α according to Eqn 2.3.10 where $\alpha = \alpha^{\text{CRD}}$ is determined by the simultaneous ring-down time measurement via Eqn 2.3.11. Note that the simultaneously measured values of S^{CRD} need to be used.

In practice, measurements at low densities will be noisy. In particular, α^{CRD} will become very inaccurate close to the CRD limit of detection. Without sample, *i.e.* for $\alpha = 0$, Eqn 2.3.10 becomes the background (signal-blank) measurement:

$$S_{\text{bg}}^{\text{LIF}} = S_0^{\text{LIF}} + \gamma = \beta S_0^{\text{CRD}} + \gamma, \tag{2.3.13}$$

in which $S_{\text{bg}}^{\text{LIF}}$ is the background signal detected by the LIF PMT, S_0^{LIF} is the laser-dependent background signal and S_0^{CRD} is the time-integrated CRD transient of the signal-blank measurement.

It is recommended that γ is determined from a measurement without laser, *i.e.* $S^{\text{CRD}} = 0$, and β from a subsequent measurement without sample, $\alpha = 0$, *i.e.* the signal-blank measurement to determine τ_0:

$$\beta = S_{\text{bg}}^{\text{CELIF}} = \frac{S_{\text{bg}}^{\text{LIF}} - \gamma}{S_0^{\text{CRD}}}. \tag{2.3.14}$$

Here, we can identify β as the background CELIF signal. Having established γ and β, the CELIF calibration factor, $\mathcal{K}$, can then be determined via

$$S_{\text{sample}}^{\text{CELIF}} = S_{\text{tot}}^{\text{CELIF}} - S_{\text{bg}}^{\text{CELIF}} = \frac{S_{\text{tot}}^{\text{LIF}} - \gamma}{S^{\text{CRD}}} - \beta = \mathcal{K} \cdot \alpha^{\text{CRD}}, \tag{2.3.15}$$

in which $S_{\text{sample}}^{\text{CELIF}}$ is the CELIF signal due to the sample fluorescence. If γ and β are determined as described above and $S_{\text{tot}}^{\text{CELIF}}$ is measured as a function of sample density, the linear fit using Eqn 2.3.15 should be forced through zero to determine $\mathcal{K}$.

This is a robust calibration as both the LIF and CRD measurements use the same photons to excite the same sample. Note that $\mathcal{K}$ depends on the experimental parameters of the detection system and the gains of both the LIF and the CRD

detectors, thus, the calibration needs to be repeated after any change of detection parameters.

Following the calibration, as described above, the absorption coefficient or sample density can be determined from CELIF when the sample concentration is not within the CRD dynamic range, *i.e.* when τ and τ_0 are indistinguishable, or when τ is very small and the CRD transient cannot be fitted with a single exponential decay. The absorption coefficient is determined via

$$\alpha^{\mathrm{CELIF}} = \frac{1}{\mathcal{K}}\left(S_{\mathrm{tot}}^{\mathrm{CELIF}} - S_{\mathrm{bg}}^{\mathrm{CELIF}}\right) = \frac{1}{\mathcal{K}}\left(\frac{S_{\mathrm{tot}}^{\mathrm{LIF}} - \gamma}{S^{\mathrm{CRD}}} - \frac{S_{\mathrm{bg}}^{\mathrm{LIF}} - \gamma}{S_0^{\mathrm{CRD}}}\right). \tag{2.3.16}$$

2.3.3 Densities and Concentrations

The number density of acetone in the cavity is measured from CRD, ρ^{CRD} using

$$\rho^{\mathrm{CRD}} = \frac{\alpha^{\mathrm{CRD}}}{\sigma} = \frac{1}{c\sigma}\left(\frac{1}{\tau} - \frac{1}{\tau_0}\right). \tag{2.3.17}$$

The number density of acetone can be converted into relative concentration, C^{CRD} in parts per million (ppm) (concentration by volume of one part of acetone per million parts of air in an acetone–air mixture) using

$$C^{\mathrm{CRD}} = \frac{\rho^{\mathrm{CRD}}}{\rho_{\mathrm{air}}} \times 10^6, \tag{2.3.18}$$

where ρ_{air} is the number density of air molecules in the cavity, and is given by the ideal gas law:

$$\rho_{\mathrm{air}} = \frac{p}{k_{\mathrm{B}}T}, \tag{2.3.19}$$

in which k_{B} is the Boltzmann constant, T is the temperature and p is the absolute pressure measured within the filled cavity. Substituting from Eqns 2.3.15, 2.3.17 and 2.3.19 into eqn 2.3.18:

$$C^{\mathrm{CRD}} = \frac{k_{\mathrm{B}}T}{p}\frac{1}{\sigma}10^6\alpha^{\mathrm{CRD}} = \frac{k_{\mathrm{B}}T}{p}\frac{1}{\sigma}10^6\frac{S_{\mathrm{sample}}^{\mathrm{CELIF}}}{\mathcal{K}}. \tag{2.3.20}$$

In the acetone CELIF calibration measurements, $S_{\mathrm{sample}}^{\mathrm{CELIF}}$ is expressed as

$$S_{\mathrm{sample}}^{\mathrm{CELIF}} = \mathcal{K}'C^{\mathrm{CRD}}, \tag{2.3.21}$$

where the proportionality factor $\mathcal{K}'$:

$$\mathcal{K}' = \frac{\sigma p}{k_{\mathrm{B}}T}10^{-6}\mathcal{K}. \tag{2.3.22}$$

The acetone concentration from CELIF, C^{CELIF}, can be determined from Eqn 2.3.21 as

$$C^{\mathrm{CELIF}} = \frac{S^{\mathrm{CELIF}}_{\mathrm{sample}}}{\mathcal{K}'}. \tag{2.3.23}$$

If any aspect of the detection system is changed then the calibration needs to be repeated, for example:

- g^{LIF} and g^{CRD} depend on the PMTs' gains;
- spectral or spacial filters to reduce background change g^{LIF} and β and may change γ;
- changing the probe wavelength may change Γ, g^{LIF}, g^{CRD} and T, *i.e.* all aspects of $\mathcal{K}$.

2.3.4 Error Propagation

For the following, we assume that the LIF PMT is operated under photon counting conditions. S^{LIF} is recorded as photon count per laser shot, averaged over n shots. Each of the quantities $S^{\mathrm{LIF}}_{\mathrm{tot}}$, $S^{\mathrm{LIF}}_{\mathrm{bg}}$ and γ is measured separately, thus the errors in these measurements are not correlated. The shot noise from counting LIF photons over n laser shots for $S^{\mathrm{LIF}}_{\mathrm{tot}}$, $S^{\mathrm{LIF}}_{\mathrm{bg}}$ and γ dominates, and is given as

$$\delta S^{\mathrm{LIF}}_{\mathrm{tot}} = \sqrt{\frac{S^{\mathrm{LIF}}_{\mathrm{tot}}}{n}}, \qquad \delta S^{\mathrm{LIF}}_{\mathrm{bg}} = \sqrt{\frac{S^{\mathrm{LIF}}_{\mathrm{bg}}}{n}}, \qquad \delta\gamma = \sqrt{\frac{\gamma}{n}},$$

and comes from Poisson statistics, as confirmed by the measurements presented in chapter 3. While γ is independent of the laser intensity, it is measured n times and averaged over the same time period in which the LIF measurements were taken. S^{CRD} is the corresponding average of the integrated transients. The errors of the measured S^{CRD} is:

$$\frac{\delta S^{\mathrm{CRD}}}{S^{\mathrm{CRD}}} = f,$$

in which f is the fractional error in the determination of S^{CRD}. In the acetone experiment, S^{CRD} is measured by an analogue integrator, as described in chapter 3. The comparison of the output of the integrator and the numerically integrated CRD

transient measured by the digiscope yielded $f = 2.7 \cdot 10^{-3}$. Note that the statistical fluctuations of S^{CRD} are irrelevant as in the CELIF method S^{LIF} needs to be normalized by the amount of light (as measured by S^{CRD}) that interacted with the sample for that measurement.

The partial derivatives required for the error propagation are:

$$\frac{\partial\alpha}{\partial S^{\mathrm{LIF}}_{\mathrm{tot}}} = \frac{1}{\mathcal{K}\cdot S^{\mathrm{CRD}}}, \qquad \frac{\partial\alpha}{\partial S^{\mathrm{LIF}}_{\mathrm{bg}}} = -\frac{1}{\mathcal{K}\cdot S^{\mathrm{CRD}}_0}, \qquad \frac{\partial\alpha}{\partial\gamma} = \frac{1}{\mathcal{K}}\frac{S^{\mathrm{CRD}} - S^{\mathrm{CRD}}_0}{S^{\mathrm{CRD}} S^{\mathrm{CRD}}_0},$$
$$\frac{\partial\alpha}{\partial S^{\mathrm{CRD}}} = -\frac{1}{\mathcal{K}}\frac{S^{\mathrm{LIF}}_{\mathrm{tot}} - \gamma}{(S^{\mathrm{CRD}})^2}, \qquad \frac{\partial\alpha}{\partial S^{\mathrm{CRD}}_0} = \frac{1}{\mathcal{K}}\frac{S^{\mathrm{LIF}}_{\mathrm{bg}} - \gamma}{(S^{\mathrm{CRD}}_0)^2}.$$

The overall expression of the error in α as measured by CELIF becomes

$$\begin{aligned}\delta\alpha = &\frac{1}{\mathcal{K}}\left\{\frac{S^{\mathrm{LIF}}_{\mathrm{tot}}}{n(S^{\mathrm{CRD}})^2} + \frac{S^{\mathrm{LIF}}_{\mathrm{bg}}}{n(S^{\mathrm{CRD}}_0)^2} + \frac{(S^{\mathrm{CRD}} - S^{\mathrm{CRD}}_0)^2}{(S^{\mathrm{CRD}})^2(S^{\mathrm{CRD}}_0)^2}\frac{\gamma}{n}\right.\\ &\left. + \frac{(S^{\mathrm{LIF}}_{\mathrm{tot}} - \gamma)^2}{(S^{\mathrm{CRD}})^2}f^2 + \frac{(S^{\mathrm{LIF}}_{\mathrm{bg}} - \gamma)^2}{(S^{\mathrm{CRD}}_0)^2}f^2\right\}^{1/2}.\end{aligned} \tag{2.3.24}$$

In practice, the latter two terms including f^2 should be negligible unless n becomes extremely large. Eqn 2.3.24 will also include a term to propagate the error in $\mathcal{K}$ determined from the fit to Eqn 2.3.15. However, this will be a systematic error for the determination of α. The square root in Eqn 2.3.24 represents the statistical error of the CELIF signal, $\delta S^{\mathrm{CELIF}}_{\mathrm{sample}} = \mathcal{K}\,\delta\alpha$:

$$\begin{aligned}\delta S^{\mathrm{CELIF}}_{\mathrm{sample}} = &\left\{\frac{S^{\mathrm{LIF}}_{\mathrm{tot}}}{n(S^{\mathrm{CRD}})^2} + \frac{S^{\mathrm{LIF}}_{\mathrm{bg}}}{n(S^{\mathrm{CRD}}_0)^2} + \frac{(S^{\mathrm{CRD}} - S^{\mathrm{CRD}}_0)^2}{(S^{\mathrm{CRD}})^2(S^{\mathrm{CRD}}_0)^2}\frac{\gamma}{n}\right.\\ &\left. + \frac{(S^{\mathrm{LIF}}_{\mathrm{tot}} - \gamma)^2}{(S^{\mathrm{CRD}})^2}f^2 + \frac{(S^{\mathrm{LIF}}_{\mathrm{bg}} - \gamma)^2}{(S^{\mathrm{CRD}}_0)^2}f^2\right\}^{1/2}.\end{aligned} \tag{2.3.25}$$

The errors in $\mathcal{K}$, σ, T and p represent systematic errors of the CELIF measurement and should be quoted separately. In terms of relative errors of the acetone number density and concentration as measured by CELIF, C^{CELIF} we get:

$$\left.\frac{\delta\rho}{\rho}\right|_{\mathrm{stat}} = \frac{\delta S^{\mathrm{CELIF}}_{\mathrm{sample}}}{S^{\mathrm{CELIF}}_{\mathrm{sample}}}, \qquad \left.\frac{\delta\rho}{\rho}\right|_{\mathrm{syst}} = \sqrt{\left(\frac{\delta\sigma}{\sigma}\right)^2 + \left(\frac{\delta\mathcal{K}}{\mathcal{K}}\right)^2}, \tag{2.3.26}$$

$$\left.\frac{\delta C^{\mathrm{CELIF}}}{C^{\mathrm{CELIF}}}\right|_{\mathrm{stat}} = \frac{\delta S^{\mathrm{CELIF}}_{\mathrm{sample}}}{S^{\mathrm{CELIF}}_{\mathrm{sample}}}, \quad \left.\frac{\delta C^{\mathrm{CELIF}}}{C^{\mathrm{CELIF}}}\right|_{\mathrm{syst}} = \sqrt{\left(\frac{\delta\sigma}{\sigma}\right)^2 + \left(\frac{\delta\mathcal{K}}{\mathcal{K}}\right)^2 + \left(\frac{\delta T}{T}\right)^2 + \left(\frac{\delta p}{p}\right)^2}. \tag{2.3.27}$$

The error in the acetone number density as measured by CRD, $\delta\rho^{\mathrm{CRD}}$ is

$$\delta\rho^{\mathrm{CRD}} = \frac{1}{c\sigma}\sqrt{\left(\frac{\delta\tau_0}{\tau_0^2}\right)^2 + \left(\frac{\delta\tau}{\tau^2}\right)^2}. \tag{2.3.28}$$

The relative errors of the acetone concentration as measured by CRD are

$$\left.\frac{\delta C^{\mathrm{CRD}}}{C^{\mathrm{CRD}}}\right|_{\mathrm{stat}} = \frac{\delta\rho^{\mathrm{CRD}}}{\rho^{\mathrm{CRD}}}, \qquad \left.\frac{\delta C^{\mathrm{CRD}}}{C^{\mathrm{CRD}}}\right|_{\mathrm{syst}} = \sqrt{\left(\frac{\delta T}{T}\right)^2 + \left(\frac{\delta p}{p}\right)^2}. \tag{2.3.29}$$

2.3.5 Limit of Detection

The CRDS measurement should have reached its limit of detection (LOD) well before the CELIF measurement, *i.e.* the ring-down times with and without sample should be indistinguishable within experimental uncertainties, $\tau = \tau_0$. Consequently, $S^{\mathrm{CRD}} = S_0^{\mathrm{CRD}}$ (*cf.* Eqns 2.3.11 and 2.3.12) and Eqn 2.3.24 simplifies to

$$\delta\alpha_{\mathrm{LOD}} = \frac{1}{\mathcal{K}\, S_0^{\mathrm{CRD}}}\left\{\frac{S_{\mathrm{tot}}^{\mathrm{LIF}}}{n} + \frac{S_{\mathrm{bg}}^{\mathrm{LIF}}}{n} + (S_{\mathrm{tot}}^{\mathrm{LIF}} - \gamma)^2 f^2 + (S_{\mathrm{bg}}^{\mathrm{LIF}} - \gamma)^2 f^2\right\}^{1/2}. \tag{2.3.30}$$

We express the total and background photon counts as a sum of their constituents:

$$S_{\mathrm{tot}}^{\mathrm{LIF}} = S^{\mathrm{LIF}} + S_0^{\mathrm{LIF}} + \gamma, \qquad S_{\mathrm{bg}}^{\mathrm{LIF}} = S_0^{\mathrm{LIF}} + \gamma,$$

in which S^{LIF} is the detected fluorescence from the sample, S_0^{LIF} is the laser-dependent background and γ the laser-independent background, see above. Multiplying Eqn 2.3.30 by $\mathcal{K}\, S_0^{\mathrm{CRD}}$ yields the error in S^{LIF}:

$$\delta S^{\mathrm{LIF}} = \mathcal{K}\, S_0^{\mathrm{CRD}}\, \delta\alpha = \left\{\frac{S^{\mathrm{LIF}} + 2S_0^{\mathrm{LIF}} + 2\gamma}{n} + \left((S^{\mathrm{LIF}})^2 + 2S_0^{\mathrm{LIF}} S^{\mathrm{LIF}} + 2(S_0^{\mathrm{LIF}})^2\right) f^2\right\}^{1/2}. \tag{2.3.31}$$

Again, the f^2 terms should be negligible.

In terms of Poisson statistics, δS^{LIF} represents one standard deviation. At the limit of detection, the measured total signal is multiple standard deviations above the signal blank. As the signal blank, $S_{\mathrm{bg}}^{\mathrm{LIF}}$, is already removed from S^{LIF}, the LOD is simply

$$S_{\mathrm{LOD}}^{\mathrm{LIF}} = m \cdot \delta S^{\mathrm{LIF}}, \tag{2.3.32}$$

in which $m = 1, 2, 3$ represent the 68%, 95% and 99.7% confidence limits, respectively. Solving Eqn 2.3.32 for S^{LIF} yields:

$$S_{\mathrm{LOD}}^{\mathrm{LIF}} =$$

$$\frac{2nS_0^{\mathrm{LIF}}m^2f^2 + m^2 + m\sqrt{m^2 + (2nS_0^{\mathrm{LIF}}f)^2(2 - m^2f^2) + 8n(S_{\mathrm{bg}}^{\mathrm{LIF}} - (S_0^{\mathrm{LIF}}/2 + \gamma)m^2f^2)}}{2n(1 - m^2f^2)}.$$

In the limit of $f \to 0$, the LOD becomes

$$S_{\mathrm{LOD}}^{\mathrm{LIF}} = \frac{m^2 + m\sqrt{m^2 + 8nS_{\mathrm{bg}}^{\mathrm{LIF}}}}{2n}, \tag{2.3.33}$$

and

$$\alpha_{\mathrm{LOD}} = \frac{1}{\mathcal{K}\, S_0^{\mathrm{CRD}}} \cdot \frac{1}{2n}\left(m^2 + m\sqrt{m^2 + 8nS_{\mathrm{bg}}^{\mathrm{LIF}}}\right). \tag{2.3.34}$$

Note that converting $S_{\mathrm{LOD}}^{\mathrm{LIF}}$ into α_{LOD} reintroduces the error in S_0^{CRD} which is again negligible in the limit $f \to 0$. Using the 99.7% confidence limit ($m = 3$) and for large n, the limit of detection simplifies to

$$\alpha_{\mathrm{LOD}}^{3\sigma} = \frac{1}{\mathcal{K}\, S_0^{\mathrm{CRD}}} \cdot 3\sqrt{\frac{2S_{\mathrm{bg}}^{\mathrm{LIF}}}{n}}. \tag{2.3.35}$$

The acetone concentration limit of detection can be expressed using the calibration factor $\mathcal{K}'$ as:

$$C_{\mathrm{LOD}}^{3\sigma} = \frac{1}{\mathcal{K}'\, S_0^{\mathrm{CRD}}} \cdot 3\sqrt{\frac{2S_{\mathrm{bg}}^{\mathrm{LIF}}}{n}}. \tag{2.3.36}$$

Scaling of the Limit of Detection

Using $S_{\mathrm{bg}}^{\mathrm{LIF}} = \beta S_0^{\mathrm{CRD}} + \gamma$ (Eqn 2.3.13) the limit of detection scales as

$$\alpha_{\mathrm{LOD}} = \frac{m}{\mathcal{K}}\sqrt{\frac{2}{n}\left(\frac{\beta}{S_0^{\mathrm{CRD}}} + \frac{\gamma}{(S_0^{\mathrm{CRD}})^2}\right)}. \tag{2.3.37}$$

Substituting S^{CRD} and $\mathcal{K}$ (Eqns 2.3.7 and 2.3.8) yields

$$\alpha_{\mathrm{LOD}} = \frac{m}{\Gamma\, g^{\mathrm{LIF}}}\sqrt{\frac{2}{n}\left(\frac{\beta g^{\mathrm{CRD}}T}{I_{\mathrm{L}} \cdot 2} + \frac{\gamma}{I_{\mathrm{L}}^2}\right)}. \tag{2.3.38}$$

Thus, the limit of detection can be lowered by

- reducing the detection of background photons by minimising β and γ;
- increasing the efficiency of the fluorescence detection: $\alpha_{\mathrm{LOD}} \propto (g^{\mathrm{LIF}})^{-1}$ (note that in the photon counting limit, the gain of the LIF PMT will not change g^{LIF});

- increasing the number of laser shots or the laser intensity: $\alpha_{\mathrm{LOD}} \propto (nI_{\mathrm{L}})^{-1/2}$.

The factor g^{CRD} in the square root suggests that reducing the CRD PMT gain will lower the LOD. However, for $g^{\mathrm{CRD}} \to 0$ the error in S^{CRD} will no longer be small and the approximation $f = 0$ will not be valid.

The dependency $\alpha_{\mathrm{LOD}} \propto (nI_{\mathrm{L}})^{-1/2}$ means that the reduction of the LOD simply depends on the total number of laser photons that have interacted with the sample. Hence, a laser with a low repetition rate but high pulse energy can deliver the same LOD as a high-rep-rate laser with low pulse energy.

Reducing Background Signal

Eqn 2.3.37 shows that the aim should be to minimise the number of background photons reaching the detector (minimise β) without compromising the detection of fluorescence photons from the sample (no reduction in $\mathcal{K}$). Experience with the acetone experiment shows that changes to the LIF detection system (*e.g.* changing filters or slits) should be evaluated via the calibration procedure, *i.e.* through the determination of γ, β and $\mathcal{K}$. γ should be unchanged unless there is a significant amount of ambient light reaching the detector. β should be reduced, *e.g.* by the introduction of a slit, as discussed in chapter 3. Ideally, $\mathcal{K}$ should not change but will be reduced in practice. The ratio

$$\alpha_{\mathrm{LOD}} \propto \frac{\sqrt{\beta}}{\mathcal{K}}$$

represents the quantitative improvement (*i.e.* reduction) of the limit of detection and should be minimised.

2.3.6 Under-Counting

When using the LIF detector in photon-counting mode, the possibility of under-counting, or pile-up, of photons needs to be considered: If two or more photons arrive at the PMT at the "same" time, only one is counted [57–60].

Amount of Under-Counting

There will be a minimum time delay, Δt, between the arrival of two photons that can be distinguished and separately counted by the detection system. This will depend on the sampling rate (*i.e.* time bin) of the digitiser, the speed of the PMT (*i.e.* the width of a digitised single photon event), the dead time of the PMT before the next photon produces sufficient signal and the photon-counting algorithm.

In the following derivation, we again adopt the convention that LIF signals are average photon counts per laser shot. We assume that the fluorescence lifetime is negligible compared to the ring-down time, τ, *i.e.* the temporal distribution of the fluorescence should follow the ring-down decay. The average total number of photons per shot is given by the temporal integration of the fluorescence:

$$S_{\text{tot}} = \int_0^\infty A\, e^{-t/\tau}\, \mathrm{d}t = A\tau, \tag{2.3.39}$$

in which A is the amplitude at time $t = 0$ and equates to the number of photons per unit time at the start of the decay. We define

$$S_0 = A\Delta t = S_{\text{tot}} \cdot \frac{\Delta t}{\tau} \tag{2.3.40}$$

as the number of photons expected to arrive in the first time bin. To make photon counting viable, S_0 should be small:

$$S_0 \ll 1. \tag{2.3.41}$$

Given the underlying random nature of the fluorescence, the number of emitted (or detectable) photons at any given time will follow a Poisson distribution:

$$p(k; \bar{M}) = \frac{\bar{M}^k}{k!}\, e^{-\bar{M}}, \tag{2.3.42}$$

in which k is the number of emitted or detected photons and $\bar{M}$ is the average number of photons. Here, $\bar{M}$ is given by the expected average number of photons at time t,

$$S(t) = S_0\, e^{-t/\tau}, \tag{2.3.43}$$

and the probability to count k photons at time t in the decay is

$$p(k, t) = \frac{\left(S_0\, e^{-t/\tau}\right)^k}{k!}\, \exp\left(-S_0\, e^{-t/\tau}\right). \tag{2.3.44}$$

The probability that a shot does not produce any photons at time t is

$$p(0,t) = \exp\left(-S_0\, e^{-t/\tau}\right), \tag{2.3.45}$$

and the probability that one or more photons occur is therefore

$$p(k>0,t) = 1 - \exp\left(-S_0\, e^{-t/\tau}\right). \tag{2.3.46}$$

This is also the probability of a photon count because if multiple photons arrive at the same time they will only be counted as one. Integration will lead to the number of counted photons per shot:

$$S_\mathrm{c} = \int_0^\infty p(k>0,t)\frac{1}{\Delta t}\,\mathrm{d}t = \int_0^\infty \left(1 - \exp\left(-S_0\, e^{-t/\tau}\right)\right)\frac{1}{\Delta t}\,\mathrm{d}t. \tag{2.3.47}$$

The factor $1/\Delta t$ converts the probability per bin into a probability per unit time and is required for the correct integration. The integral in Eqn 2.3.47 is non-trivial and requires some manipulations. This can be simplified, as detailed in appendix A, to

$$S_\mathrm{c} = S_\mathrm{tot}\left(1 - \frac{1}{4}\left(S_\mathrm{tot}\frac{\Delta t}{\tau}\right) + \frac{1}{18}\left(S_\mathrm{tot}\frac{\Delta t}{\tau}\right)^2 - \frac{1}{96}\left(S_\mathrm{tot}\frac{\Delta t}{\tau}\right)^3 + \ldots\right). \tag{2.3.48}$$

The 2$^\mathrm{nd}$ term in the bracket can be interpreted as the fractional under-count due to two simultaneous photons, however this overestimates the under-count, hence the 3$^\mathrm{rd}$ term is additive. An alternative derivation is presented in appendix A.

For the acetone experiment, typical parameters are $\tau = 900$ ns, $S_\mathrm{tot} = 4$ photons per shot for a relatively high acetone concentration and $\Delta t = 3$ ns as explained below. The relative corrections are then 0.3%, $1 \cdot 10^{-5}$ and $2 \cdot 10^{-8}$ for the two-, three- and four-photon terms, respectively. Nevertheless, increasing signal levels will invariably lead to significant under-counting as S_tot increases and τ decreases.

Under-Count Correction

Including only the two-photon correction, the number of counted photons is

$$S_\mathrm{c} = S_\mathrm{tot} - \frac{S_\mathrm{tot}^2}{4}\frac{\Delta t}{\tau}. \tag{2.3.49}$$

The corresponding quadratic equation is

$$\frac{\Delta t}{4\tau}S_\mathrm{tot}^2 - S_\mathrm{tot} + S_\mathrm{c} = 0, \tag{2.3.50}$$

with the relevant solution

$$S_{\text{tot}} = \frac{2\tau}{\Delta t}\left(1 - \sqrt{1 - \frac{\Delta t}{\tau}S_{\text{c}}}\right). \tag{2.3.51}$$

Using the Taylor expansion

$$\sqrt{1-x} = 1 - \frac{x}{2} - \frac{1}{2}\left(\frac{x}{2}\right)^2 - \frac{1}{2}\left(\frac{x}{2}\right)^3 - \dots$$

leads to the approximate expression

$$S_{\text{tot}} = S_{\text{c}}\left(1 + \frac{1}{4}\frac{\Delta t}{\tau}S_{\text{c}} + \frac{1}{8}\left(\frac{\Delta t}{\tau}S_{\text{c}}\right)^2 + \dots\right) \approx S_{\text{c}}\left(1 + \frac{\Delta t}{4\tau}S_{\text{c}}\right). \tag{2.3.52}$$

The approximation Eqn 2.3.52 is quite accurate even for an under-count of $(\Delta t/4\tau)S_{\text{c}} = 5\%$ where it only deviates by $\approx 0.5\%$ from the exact solution Eqn 2.3.51. However, once three-photon under-counting becomes significant, *cf.* Eqn 2.3.48, the above correction should be questioned.

The result Eqn 2.3.52 is not surprising when comparing to Eqn 2.3.48 as for small corrections $S_{\text{tot}} \approx S_{\text{c}}$. The inclusion of the higher terms in Eqn 2.3.48 will be more complex.

The under-count correction requires knowledge of the ring-down time, τ, and the minimum difference in arrival time to distinguish two photons, Δt. To determine Δt, the LIF signals from a high concentration acetone–nitrogen mixture were recorded from 10000 laser shots, with a sampling interval of 1 ns. The arrival times of the photons were recorded along with a histogram of the time difference between each two subsequent photons as shown in figure 2.5. From the histogram, we determined that the minimum distinguishable difference between two subsequent photons is 3 ns.

In the next chapter, the acetone CELIF experiment setup is described along with the technical details of the CELIF device including: the laser and optics system, the optical cavity and the data acquisition.

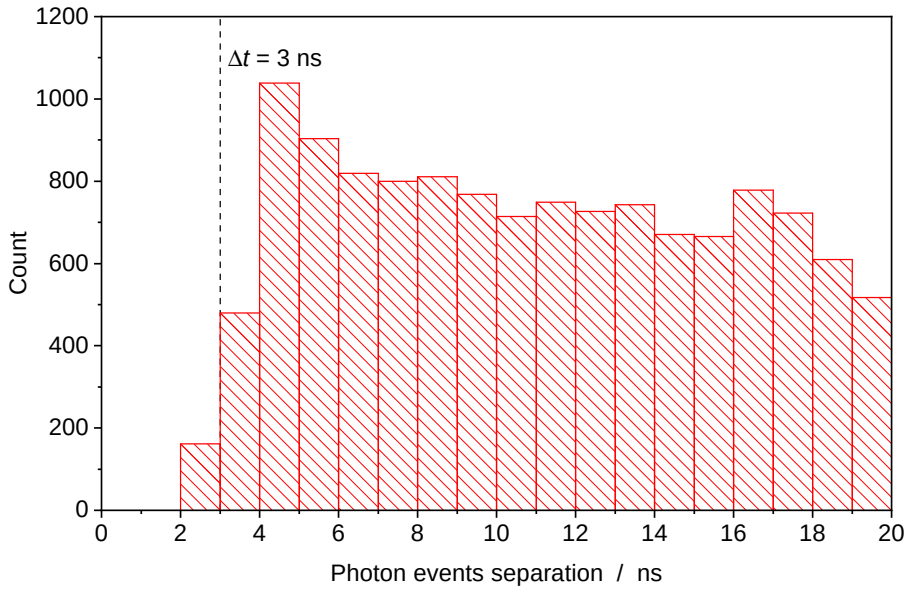

Figure 2.5: Histogram of the time difference between two subsequent acetone photons. The measurements were recorded over 10000 laser shots with a time interval of 1 ns. The recorded total number of photon events was 68412, but only data from 12678 photons with arrival time separation of < 20 ns were plotted.

Chapter 3

Experimental Setup and Data Acquisition

3.1 Laser System and Experiment Setup

The laser used in the experiment was a compact, frequency quadrupled Nd:YAG pulsed laser of 266 nm wavelength (Elforlight-SPOT-10-50-266). The laser is air cooled and the power consumption of the laser is 100 W. The laser is of 15 kHz repetition rate, 95 mW average power, 6.3 μJ pulse energy and < 2 ns pulse width. The high repetition rate of the laser was necessary to allow making a CELIF measurement every 100 ms, where, to minimise the statistical errors, each measurements was an average of 1500 laser shots.

Figure 3.1 shows the CELIF experiment setup. The wavelength separator works efficiently with a vertically polarised light, thus the laser head was rotated to rotate the polarisation of the beam to vertical. The beam was first passed through a Pellin-Broca prism to separate the remaining 532 nm beam. Because the output beam of the laser was divergent and elliptical, the 266 nm beam was spatially shaped so that it closely matches the size and and radius of curvature of the TEM_{00} mode of the cavity. This was achieved, as discussed in section 2.2, by directing it to a set of telescope lenses: a cylindrical horizontal lens (f = 100 mm), a focusing spherical lens (f = 75 mm), then a 100 μm pinhole to clean the edges of the beam and form the TEM_{00} transverse mode of the cavity, then through a collimating lens (f = 50 mm).

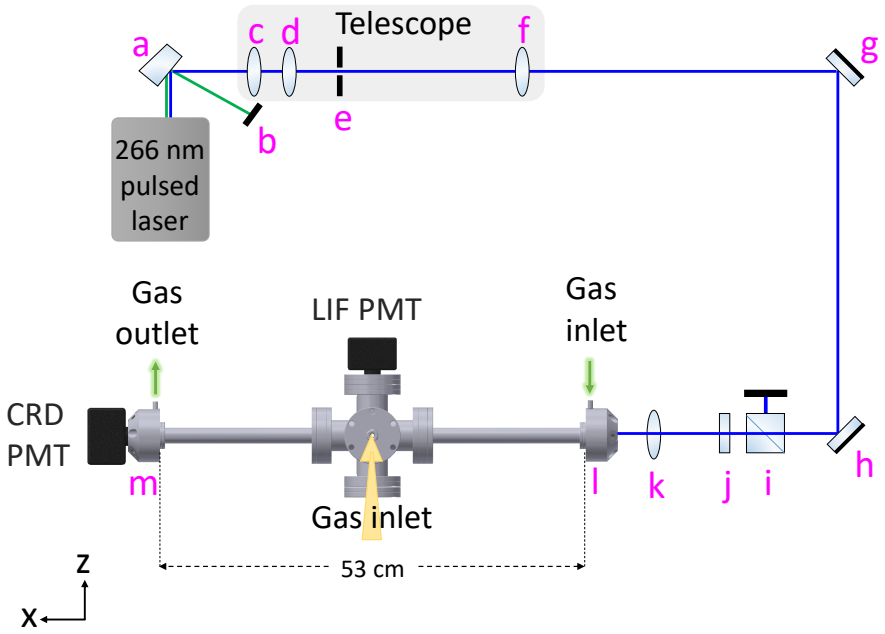

Figure 3.1: The laser and optics setup for the CELIF experiment. (a) Pellin-Broca prism, (b) Beam dump, (c) Horizontal cylindrical lens (f = 100 mm), (d) Spherical lens (f = 75 mm), (e) Pinhole (100 μm), (f) Spherical lens (f = 50 mm), (g) Mirror, (h) Mirror, (i) Glan-laser prism, (j) Quarter wave plate, (k) Mode matching lens (f = 750 mm), (l) Cavity entrance mirror, (m) Cavity exit mirror .

Next, the beam was sent through two 266 nm mirrors to direct it to the cavity axis, then to an optical isolater which prevents the reflected beam from hitting the laser source. The optical isolater consisted of a Glan-laser prism, which allows only the vertical polarisation of the beam to pass, followed by a quarter wave plate, which converts the vertically polarised light into circularly polarised light. When the light hits the cavity entrance mirror it reflects with rotated circular polarisation. It then passes through the quarter wave plate, which converts the circularly polarised light into horizontally polarised light. Once the horizontally polarised light hits the Glan-laser prism it changes its direction, and thus prevents it from propagating towards the light source. Next, the beam was directed to a mode matching lens (f = 750 mm) to focus the TEM_{00} mode of the beam into the middle of the cavity.

The optical cavity (x axis) was formed by two highly reflective mirrors (Layertec 128797, HR > 99.7%, R = 1 m), which were held by mounts. Each mount was designed with three high precision screws in order to allow the precise tilting of the mirrors and aligning of the beam through the centre of the cavity. Each mirror mount was fitted with a short section of a 1/4 inch tube for gas sample inlet/outlet, and to monitor the cavity pressure using a baratron (MKS 728A Absolute Capacitance Manometer). The middle section of the cavity was a 6-way cross (38.1 mm OD) which joined the mirror mounts with two side arms (each was 3/4 inch OD × 200 mm long tube). The 6-way cross was necessary for the LIF optics and PMT to be mounted on the top, perpendicular to the cavity axis (z axis), and to provide another gas path through the cavity (y axis). The total length of the cavity from the entrance mirror to the exit mirror was 53 cm.

3.1.1 CRD Setup

The beam enters the cavity, and bounces back and forth between the cavity mirrors, and the CRD signal is detected using the CRD photomultiplier tube (PMT) (Hamamatsu R1527) which was mounted after the exit cavity mirror and was enclosed in a RF shielding box. Even though the beam was shaped to match the TEM_{00} mode of the cavity, there still some oscillatory structure superimposed on the exponential decay of the CRD signal. As discussed in section 2.2, this structure is minimized

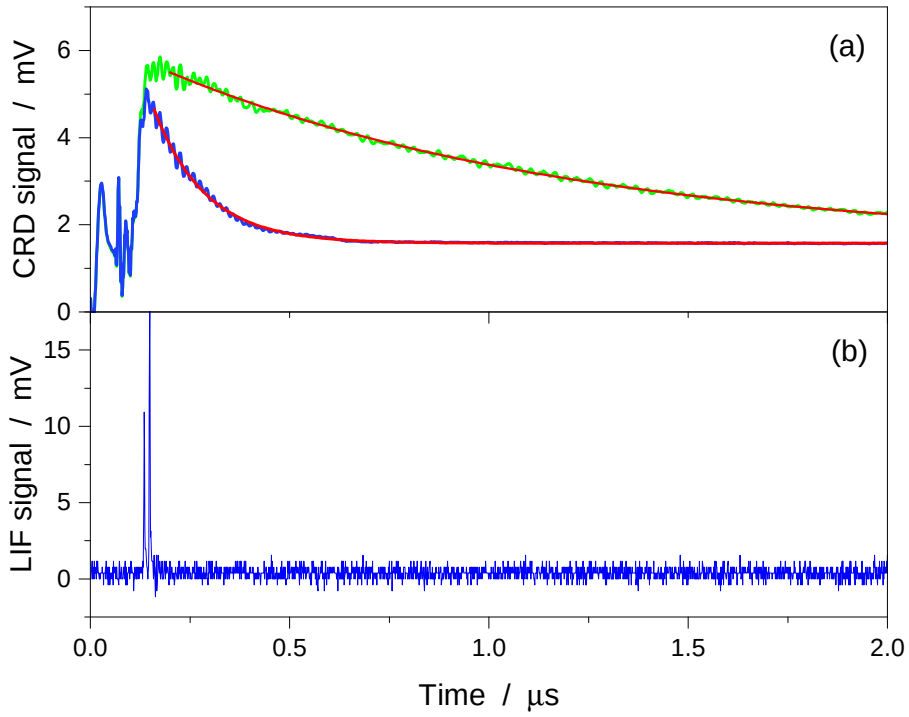

Figure 3.2: (a) The green curve is a background CRD transient recorded with 1 bar of nitrogen, and the blue curve is a CRD transient recorded using a 50 ppm acetone–nitrogen mixture. Each transient was an average of 1500 laser shots. The red curves are fitting curves to a first order exponential decay. The noise in the base line in the first 100 ns is from the integrator circuit. The CRD signal is divided by the integrator gain, 22. (b) LIF transient recorded using the same 50 ppm acetone–nitrogen mixture. This was the last transient of all the 1500 laser shots.

using a 20 MHz bandwidth limit when recording the CRD signals. An example of a raw CRD and LIF data is displayed in figure 3.2. Each of the background and acetone CRD transients was an average of 1500 laser shots. The red curves are fitting curves to a first order exponential decay to extract the ring-down times. The acetone LIF transient was the last transient of all the 1500 laser shots, as the digitizer only displays the last transient.

The CRD measurements are sensitive to the temporal shape of the ring-down decay, which not only depends on the mode coupling of the laser beam into the cavity, but also on the stability of the mirror alignment. The statistical error in the ring-down time was determined by how an acetone CELIF measurement affects the mirror alignment and the empty cavity ring-down time, τ_0. This was done by measuring τ_0 from fitting an average of 1500 CRD transients recorded at 1 bar of N_2 before exposing the cavity to acetone. Then, the cavity was filled with 1 bar of a mixture of acetone–nitrogen, and left inside for 30 s. The cavity was then pumped down and left under vacuum for 15 minutes. After that, the cavity was flushed 5 times with nitrogen, and then τ_0 was measured again. This CELIF measurement procedure yielded a ring-down time fractional error of:

$$\frac{\delta\tau}{\tau} = 0.02\,.$$

3.1.2 LIF Optics Setup

The LIF PMT is mounted perpendicular to the cavity axis (along the z axis), on the top of the 6-way cross, at the centre of the cavity. The LIF optics were chosen and optimised based on simulations made by another group member [61]. The LIF setup consists of two achromatic lenses (f = 30 mm), mounted in a lens tube and inserted in the 6-way cross as shown in figure 3.3. On the top of the two lenses there was a (21×3.5 mm) slit mounted in a X-Y translator on the focus of the top lens, along the laser axis (x axis). The slit was used to only image fluorescence from the gas samples, and to filter out the LIF noise which comes from the cavity mirrors fluorescence, as discussed in chapter 2. The accurate distance between the lenses, and the x,y,z position of the slit was optimised by optimising the CELIF signal of an acetone–nitrogen mixture.

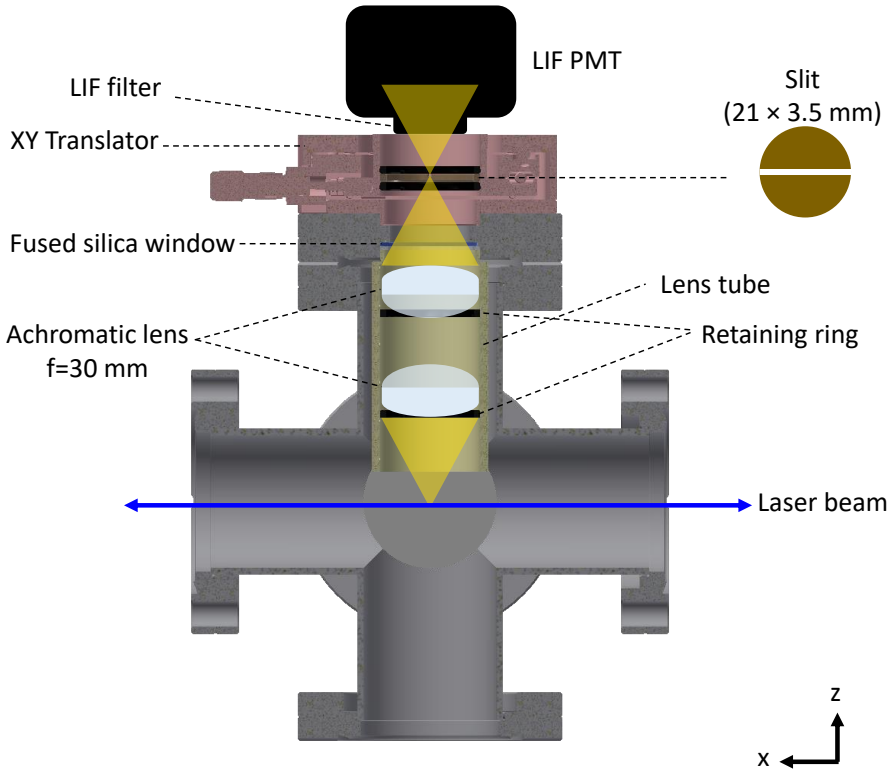

Figure 3.3: Schematic representation of a cross section view of the 6-way cross showing the LIF optics setup.

The slit width was chosen such that it does not block any acetone signal. It was optimised by measuring the LIF signal of an acetone–nitrogen mixture at different slit widths and comparing this to the LIF signal measured without slit. As shown in figure 3.4, while using the 3.5 mm width slit significantly reduced the background LIF signal, it did not reduce the acetone LIF signal. The slit's surrounding surface was blackened with an optical absorber coating (Alion MH2200) to minimize the amount of reflected photons.

On the top of the slit there was a LIF filter (Semrock BLP01-355R-25, 355 nm long-pass edge filter), to block any scattered 266 nm light from the laser beam. This Semrock filter was chosen because it works by reflecting the light that hits it and does not absorb any of the 266 nm light, thus does not fluoresce. It was found that other types of LIF filters, Edmund Longpass filters (N-WG-320 nm and N-WG-295 nm), absorb the 266 nm light and produce a lot of fluorescence light which significantly increased the LIF background. The LIF PMT (Hamamatsu R7056) was mounted on top of the filter and it was enclosed in a RF shielding box.

3.2 Data Acquisition

A high speed, dual-channel, digitizer card with on-board signal processing (Agilent U1084A) was used for the data acquisition for the CELIF experiment. The digitizer can operate in two acquisition modes: the normal mode with simultaneous acquisition and readout using the two channels, or the combined channels, Peak TDC (Time to Digital Conversion and Analysis) mode for the real-time signal peak detection and analysis. The Peak TDC mode has a powerful built-in peak detection algorithm which allows the creation of a histogram of peak position versus time for successive acquisitions, where the histogram bins contains peak counts.

The Peak TDC mode was used to record the photon counted LIF signals. The digitizer cannot operate in Peak TDC and normal acquisition simultaneously. Thus, a home-made analog integrator was built for CRD data acquisition to measure the time integrated CRD signals, S^{CRD}.

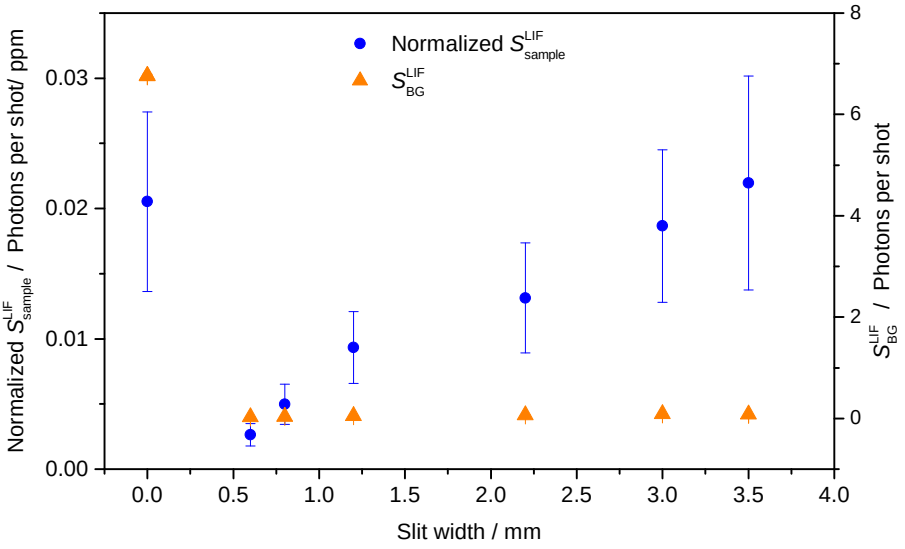

Figure 3.4: Comparison of the background LIF (orange triangles), and the acetone LIF signals (blue circles) measured without a slit, and with slits of different widths. The acetone LIF signals were measured using the same gas mixture and the signal was normalized to the acetone concentration to account for any variation in the acetone concentration. Each measurement was an average of 10000 laser shots, and was recorded while filling the cavity with 1 bar of nitrogen for background data, and with 1 bar of the acetone–nitrogen mixture for the acetone data. The error bars are from 1 standard deviation.

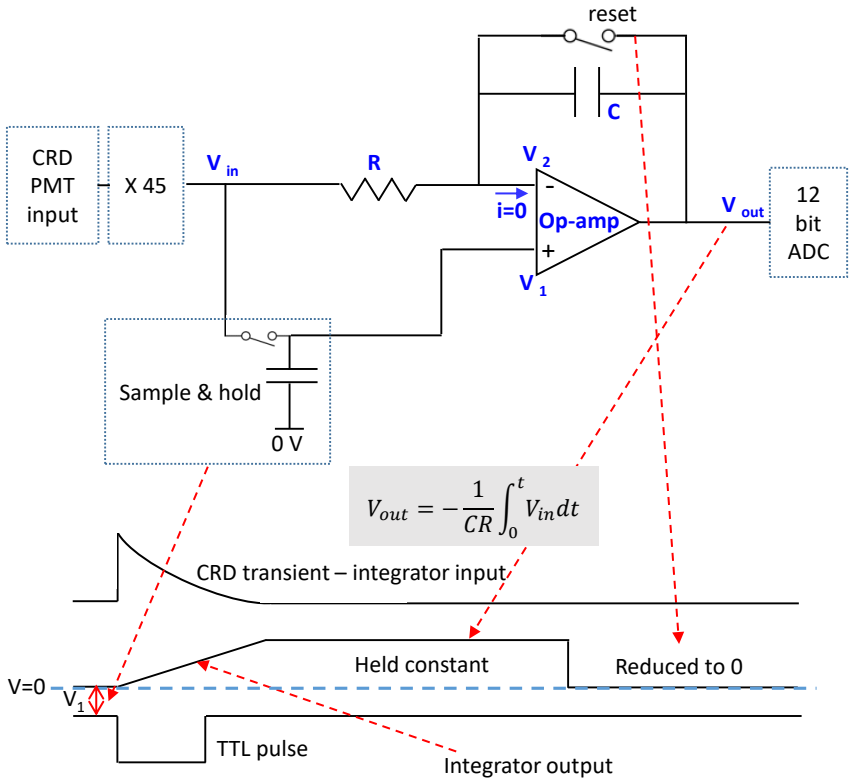

Figure 3.5: A schematic of the main integrator circuit and an example of a trigger and a ring-down pulses and the resulting integration signal.

3.2.1 The Analog Integrator

Principle of Operation

A home-made integrator was designed and built by the electronics workshop in the chemistry department at Durham University. The analog integrator is an electronic integration circuit based on an operational amplifier (op-amp), which performs the mathematical operation of integration with respect to time. Its output voltage is proportional to the amplitude and duration of the input signal. A schematic of the basic integrator circuit is shown in figure 3.5. The main components are the resistor (R), the op-amp and the capacitor (C) which is connected across the op-amp. Once the CRD signal is fed into the integrator input, the offset of the baseline of the CRD input signal (V_1) is acquired and then subtracted from the CRD signal voltage, such that only the CRD signal is integrated. The CRD signal is amplified 45 times before passing through R to improve the signal to noise ratio. The inverting input of the

amplifier (−) is a virtual ground ($V_1 = V_2$). When a voltage is applied across R, the current starts to flow through the resistor and the capacitor begins to charge up by the input voltage. The charging rate is determined by the RC time constant of R and C. The op-amp virtual earth gets obstructed and the negative feedback will produce an output voltage across the op-amp to maintain the virtual earth condition across the input. After 20 µs, the zero switch opens which discharges the capacitor and resets the integration output to zero, before the next CRD signal arrives.

Two TTL pulses (5 V) are produced at the trigger output connectors (TTL 1) and (TTL 2). TTL 1 signal is used to trigger the pulsed laser, and TTL 2 is used to trigger the acquisition in the digitizer. The resulting ring down signal from the CRD PMT is connected to the CRD input connector (CRD In). This signal is then amplified and is available at the CRD output connector (CRD Out). The output from the first stage of amplification is then integrated and is available at the signal output connector (Sig Out). The integrated signal level is held constant for 20 µs after the trigger pulse.

The integration signal is sent to an ADC (analog-to-digital converter) with a microprocessor to measure the integration output level, which is the time integrated CRD signal (S^{CRD}) within the constant part of the integration signal. The point at which the measurement is made may be varied using a PC interface. The ADC send the integration result in RS232 format, which is then converted into a USB and could be read using a PC interface. The resolution of the integrator is 1 in 4095, *i.e.* the integration result can be any value between 0–4095. The integration signal is then reduced to zero between integration measurements.

Controlling the Integrator

Data from the integrator is transferred using RS232 protocol via an USB connection. The integrator was interfaced with the PC and was controlled using a LabView program. Figure 3.6 presents a diagram of the data acquisition setup. The following parameters could be adjusted using LabView:

- Pulse frequency:

  The trigger pulse frequency may be adjusted between 10 and 15,000 Hz. The

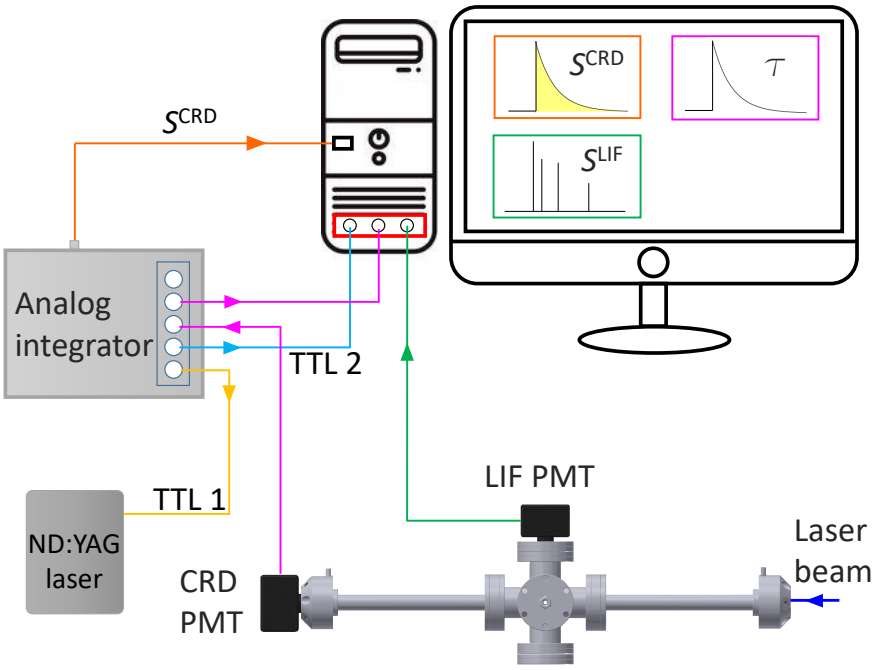

Figure 3.6: Schematic diagram of the data acquisition setup. The synchronized TTL pulses from the integrator triggers both the laser and the digitizer. The CRD signal is fed to the integrator CRD input where it is amplified and becoming available at the integrator CRD output. It is then fed to one of the digitizer inputs. The integration result is bussed to the PC by USB. The LIF signal is directly fed to the second digitizer input. A labView program was programmed to first acquire the CRD transits using the normal mode of the digitizer to measure the ring-down time using an exponential fit, then simultaneously the photon counted LIF signal using the Peak TDC mode of the digitizer, and the integration result. Then, the program calculates the CELIF signal and the acetone concentration.

Elforlight laser was running at 15,000 Hz.

- TTL 2 pulse delay:

  The second trigger pulse may be positioned relative to the first trigger pulse. A range of ±3.12 μs is possible. TTL 2 was always synchronised with TTL 1 for the CELIF measurements.

- Number of segments:

  The ADC value which is output by the integrator is produced after integrating a single ring-down event (1 segment), or the microprocessor in the integrator could be programmed to integrate several successive CRD segments then average and output the result. The number of averaged segments may be set between 1 and 10,000.

- Measurement delay:

  The ADC measurement period (5 μs) may be positioned relative to the trigger signal. A range of 1 to 13.5 μs may be set. This was normally set to 5.38 μs (about 5 times the ring-down time).

Performance of the Integrator

Integrator Gain

The area under CRD segments recorded directly from the CRD PMT was compared to that of an amplified CRD segments recorded from the integrator CRD output to measure the integrator gain. Each segment was an average of 10,000 segments of length 2.5 μs. The ratio of the amplified CRD segments to the trapezoid area of the normal CRD segments was 22.

Linearity of the Integration Result

Amplified CRD segments from the integrator CRD output were recorded simultaneously with the associated integration result S_0^{CRD}, to test the linearity of the integrator output. Each amplified CRD segment was an average of 10,000 segments of 1 μs length, and was recorded while filling the cavity with 1 bar of N_2. The

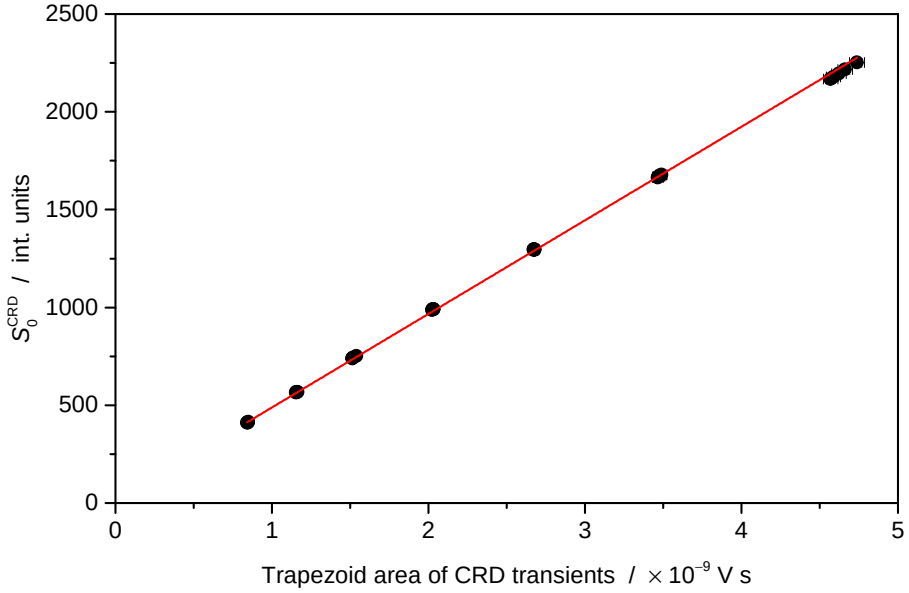

Figure 3.7: The time-integrated CRD signal, acquired from the integrator, compared to the trapezoid area of the CRD transients. The errors in x and y are from one standard deviation and are smaller than the symbols.

voltage of the CRD PMT power supply was varied between 300-240 V to vary the area of the CRD segments. S_0^{CRD} was plotted against the trapezoid area under the CRD transients after correcting for the integrator gain. As shown in figure 3.7, the integration result is linearly proportional to the area under CRD transients.

A straight line was fitted to the data giving a slope of $4.78 \times 10^{11} \pm 1.28 \times 10^{9}$. From that, the integration result unit, which we call "int. units", is

$$1 \text{ int. units} = 0.21 \times 10^{-11} \text{ V s}.$$

For the rest of this thesis, time integrated CRD signals S_0^{CRD} and S^{CRD} will be expressed in int. units. From the slope of the straight line fit and the error in the fit, the fractional error in the determination of S^{CRD} by the analog integrator is $f = 2.7 \times 10^{-3}$.

3.2.2 LabView Programs

A LabView program, provided by Agilent, which uses the digitizer as an oscilloscope was used to aid alignment of the laser through the cavity. The program was modified

by adding a first order exponential fitting function to the trace on the CRD channel. The cavity was aligned by optimising the ring-down time, and flattening the fitting residuals while looking at the PC screen in real-time. Other LabView programs were written to communicate with the digitizer and the integrator to acquire CRD and LIF data.

Photon Counting Parameters

The peak counting algorithm within the Peak TDC mode in the digitizer identifies a peak using nine samples; the sample with the highest amplitude along with four samples before and after that sample. As shown in figure 3.8, a sample will be considered to be a peak if within the nine samples analysed: a rising edge is found before the sample that exceeds the programmable ΔRise, a falling edge is found after the sample that exceeds the programmable ΔFall, and the sample is the maximum of all points between the two defined rising and falling edges. ΔRise and ΔFall are the minimum difference, in Volts, between two successive samples to identify the rising and falling edges of a peak respectively.

Before using the Peak TDC counting mode for the CELIF measurements, the correct counting thresholds, ΔRise and ΔFall, needed to be found. The Peak TDC mode does not yield all the LIF transients within which the photons where counted. It only gives the last LIF transient for testing purposes. Thus, to analyse the LIF transients and determine the thresholds, the normal mode of the digitizer was used to acquire thousands of LIF transients. Then, a photon counting algorithm was written in LabView to analyse the transients.

First, the optical cavity was filled with a mixture of acetone in nitrogen. Then, a LIF measurement was made and 4000 LIF segments were recorded. Each segment was of 10752 sample length, and was recorded with a time interval of 0.5 ns. The vertical full scale on the LIF channel in the digitizer was set to 100 mV. The LIF PMT voltage was 1400 V. The measurement was made before optimising the LIF optics setup described in section 3.1.2, and with different LIF filters. Two LIF filters were used for this test: Semrock filter (325 nm RazorEdge long-pass filter, LP03-325RS-25) and Edmund filter (N-WG-320 nm, Longpass filter). Next, the

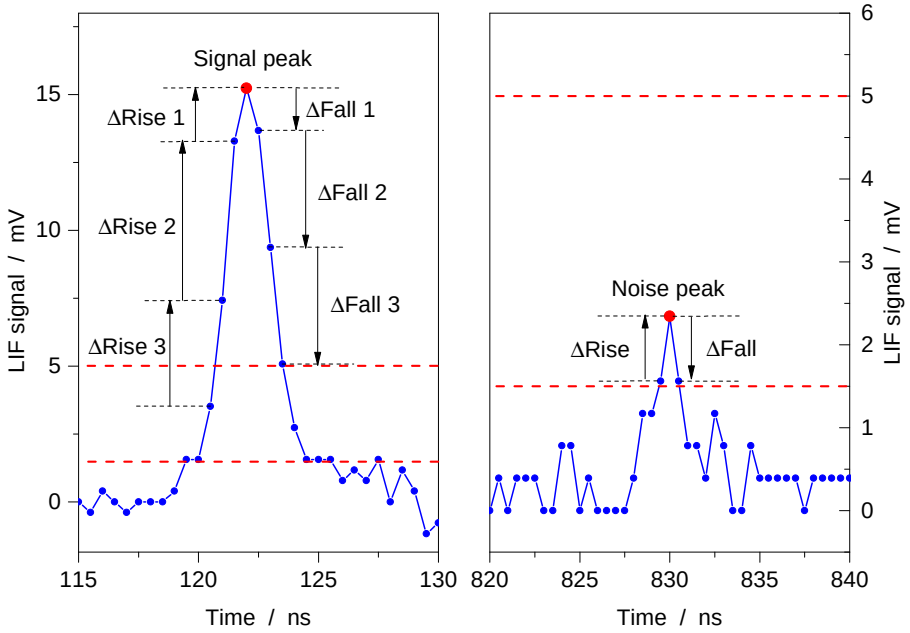

Figure 3.8: Determination of a signal peak and a noise peak by our LabView photon counting algorithm. The dashed red lines represents the higher and lower amplitude thresholds.

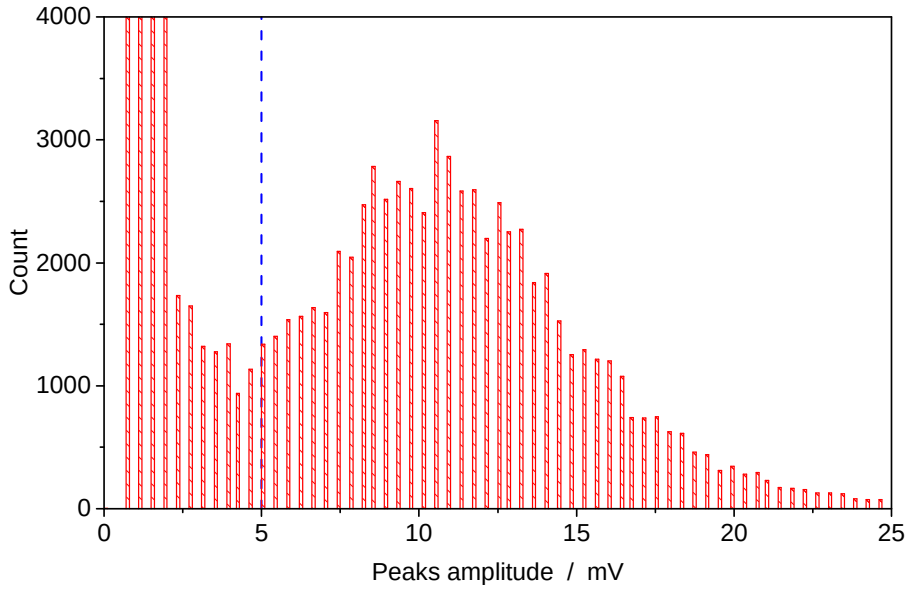

Figure 3.9: Histogram of the amplitude distribution of the noise and signal peaks, taken from 4000 laser shots. The dashed blue line represents the amplitude threshold which is used later for the separation of noise and signal peaks.

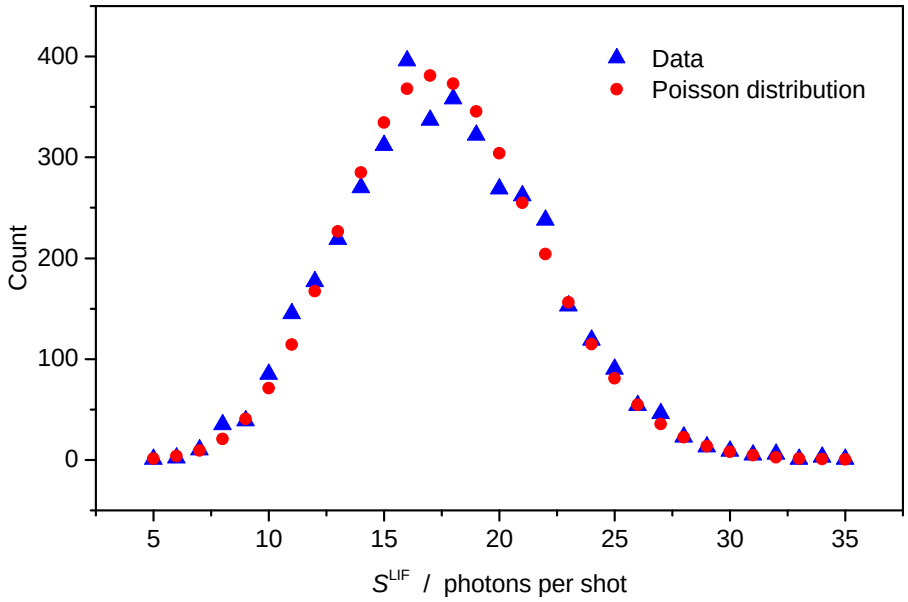

Figure 3.10: The blue triangles are the number of signal photons per shot, taken from 4000 laser shots. The red circles are the Poisson probability distribution of the number of photons per shot, with an average of 17.6 photons per shot.

LIF transients were analysed, and all the peaks above a low amplitude threshold were counted and their amplitudes were recorded. This low amplitude was set to 0.5 mV and was chosen to avoid analysing the samples which form the baseline of the LIF signal. Then, a histogram of all the peak amplitudes was plotted as shown in figure 3.9. The histogram shows two overlapping distributions: the distribution at the higher amplitudes is for the signal photons, and the distribution at the lower amplitude is for the noise peaks. From that, an amplitude threshold (5 mV) was chosen to separate noise peaks from signal photons. After that, the data were reanalysed by counting photons using 5 mV as a higher amplitude threshold to count the signal photons, along with a lower amplitude threshold (1.5 mV). All peaks between 1.5–5 mV were considered noise peaks.

To test whether the written photon counting algorithm is correct and yield a Poisson distribution of photon events, the histogram of number of photons per laser shot in all the 4000 LIF segments was fitted using a Poisson probability distribution. As shown in figure 3.10, the data matches the Poisson fit, which confirms that the photon counting is correct. Also, the arrival time of the signal photons was

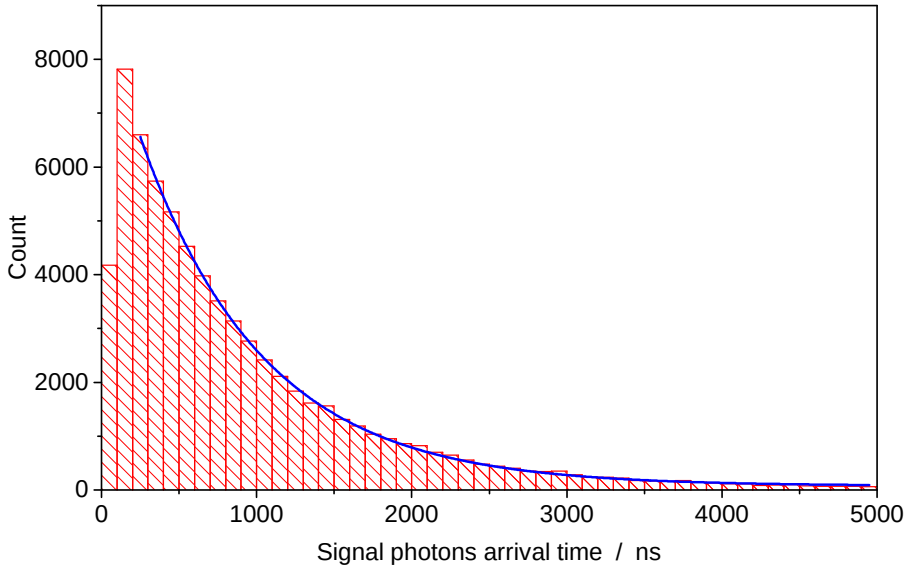

Figure 3.11: Histogram of the arrival time of the signal photons, taken from 4000 laser shots. The blue curve is a first order exponential fit.

histogramed and was fitted to a first order exponential decay. As shown in figure 3.11, the fit was perfect and matches the ring-down decay with a time constant 793 ± 5 ns.

After that, the noise and signal peaks were reanalysed, as shown in figure 3.8, by determining the sample which forms the maximum of the peak, then measuring three ΔRise before the sample, and three ΔFall after the sample. Only one ΔRise and one ΔFall where considered for noise peaks, as it was seen that the first delta of a noise peak was the largest. Next, the maximum of all three ΔRise and ΔFall was chosen for each signal peak, and from that, histograms of the maximum ΔRise and ΔFall for signal peaks and the first ΔRise and ΔFall for noise peaks were plotted. As shown in figure 3.12 (a) and (b), the noise and signal delta distributions are overlapping, with a delta value of about 2.5 mV enough to separate noise from signal photons. This value is what is needed to be used with the Peak TDC mode as the ΔRise and ΔFall threshold.

After optimising the LIF setup and using the setup described in section 3.1.2, similar measurements were made to determine the appropriate ΔRise and ΔFall threshold. These measurements, and the rest of the measurements in this thesis, were made using a vertical full scale of 100 mV for the LIF channel, and with

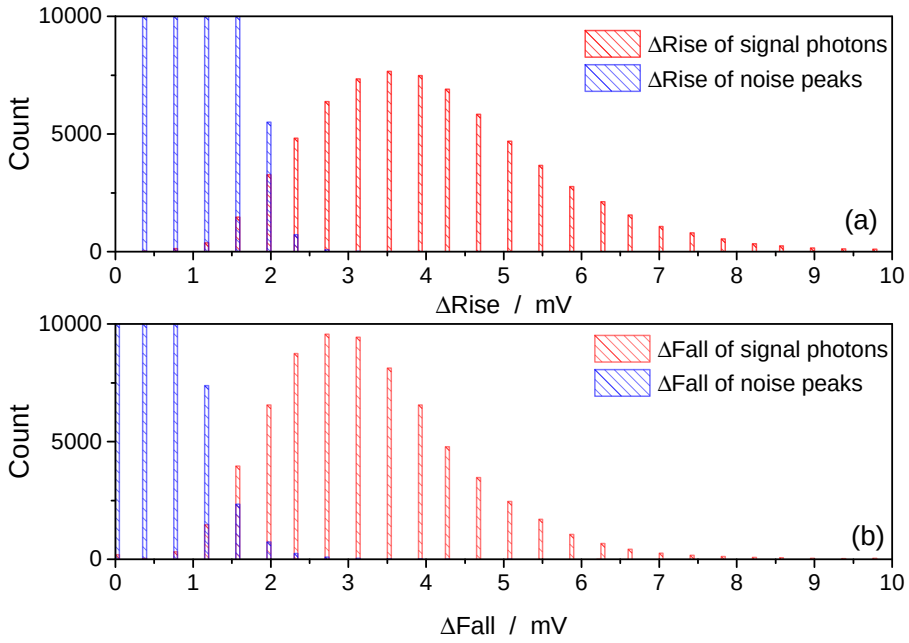

Figure 3.12: Histograms of the ΔRise and ΔFall thresholds for the noise peaks (blue) and signal peaks (red). Data were from 4000 laser shots.

sampling resolution of 1 ns with each segment being 5216 sample length. The 100 mV vertical full scale was chosen because it was seen that with any value below that, some photon signals saturate at the beginning of the LIF transients. The minimum available sampling resolutions of the digitizer was 0.25 ns, however this was not chosen as it takes a lot of computer memory and makes the selection of ΔRise and ΔFall thresholds more tight. Furthermore, the 1 ns sampling resolution was enough to resolve a full photon event. The segment length was chosen to be 5216 samples (5216 ns) to cover about five times the ring-down time of an empty cavity, and because the maximum number of samples to acquire and store 10000 segments is 5239 in the dual-channel mode of the digitizer. The number of samples must be a multiple of 32 (32 bit), and the nearest multiple of 32 for 5239 is 5216. The segment length which the digitizer acquires must also be close to the segment length which the integrator acquires. The integrator has pre-programmed segment lengths, and the closest to 5215 ns in the integrator is 5380 ns.

The ΔRise and ΔFall threshold for this setup was determined to be 1.9 mV. The digitizer accepts only certain increments of the entered delta values, depending on the vertical full scale, and most required values will be adapted by the digitizer.

Thus, the nearest value to 1.9 mV was 1.953 mV and was achieved by entering 1.8 mV in the LabView program.

CELIF LabView Program

A LabView program was written to be used for CELIF calibration measurements, to acquire LIF and CRD data and calculate the acetone concentration. An example of CRD and LIF signals acquired with this program is shown in figure 3.2. This program:

- Sets the integrator parameters (laser frequency, number of segments, measurement delay).
- Runs the digitizer in normal mode and acquires CRD transients and keeps them in the memory.
- Switches to the combined channels, Peak TDC mode, then simultaneously starts data acquisition for S^{LIF} and reads out the integration result S^{CRD}.
- Analyses CRD data by averaging all the CRD segments, then fitting a first order exponential decay to the averaged CRD trace and finding the ring-down time.
- This program runs first with the laser blocked to get the light independent LIF background, γ. Then, runs a second time with the laser unblocked while flowing N_2 through the cavity to calculate the CELIF background signal. Then, runs a third time while flowing a sample of acetone–nitrogen gas mixture.
- Next, it calculates the sample CELIF signal from the total and background CELIF signals using Eqn 2.3.15, and the acetone concentration using Eqn 2.3.18, along with the measurement errors.

Details of the calibration measurement steps is presented in chapter 4. Each measurement using this program lasts for about 30 seconds, this is due to the time the digitizer takes to switch between acquisition modes, and also the time needed for data analysis after the acquisition.

Real-time CELIF LabView Program

This LabView program was simplified from the previous one. It only runs the digitizer in the Peak TDC mode to record S^{LIF} and reads from the integrator to record S^{CRD}, and plots them in real-time. It does not acquire CRD traces, thus, does not yield the ring-down time. It was created to make fast CELIF measurements every 100 ms. It was used in testing the response time of the CELIF measurement in chapter 4, and for the breath measurements in chapter 5. Using this program to measure acetone concentration will require having a valid CELIF calibration using the previous program.

A CELIF device to measure acetone concentration in gas samples has been built. The laser system has been characterised and the optical setup for the telescope and the LIF optics has been optimised. An analog integrator, a digitizer card and a set of LabView programs were implemented in the experiment for CELIF data acquisition and analysis. In the next chapter, the CELIF measurements are described in detail, including discussing static vs. flow CELIF measurements, different flow-body designs and performance, the response time of the CELIF measurements and the validation of the CELIF instrument against the SIFT-MS.

Chapter 4

CELIF Measurements

To allow the CELIF device to perform online, real-time breath acetone measurements, CELIF measurements must not be made while filling the whole volume of the cavity with stagnant breath samples. Instead, breath samples must flow quickly through the middle of the cavity perpendicular to the cavity axis and the LIF PMT axis. The width of the sample must be short and not fill the total length of the cavity for the measurement to be quick enough to follow the real-time breath pattern.

Flow of the samples also eliminates acetone sticking to the cavity walls and mirrors by flowing the sample perpendicular through the cavity rather than along it. Keeping the cavity mirrors clean is essential for sensitive CRD measurements and reduces the frequency of cleaning. Keeping the cavity walls clean from acetone buildup is important to prevent acetone desorption during the CELIF measurements.

A flexible sheet of a non-stick PTFE material that is chemical, electrical and thermal resistant was considered for the purpose of coating the stainless steel walls of the cavity to prevent acetone adsorption during CELIF measurements. However, after testing the sheet by exposing it to the 266 nm laser, a noticeable fluorescence glowed from the sheet. This meant causing more background LIF signal. Thus, PTFE coating was not suitable to be used on the cavity walls.

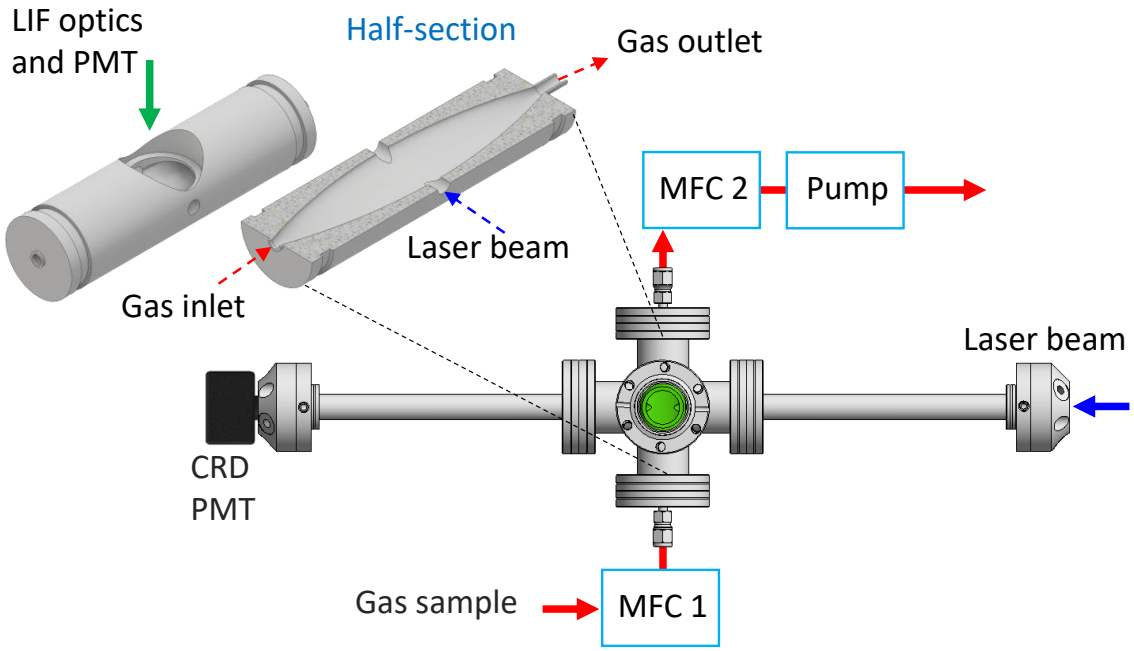

Figure 4.1: Schematic diagram of the CELIF experiment setup, using two mass flow controllers and flow-body-1.

4.1 Initial Flow-body

To allow CELIF measurements of flowing samples, an insert for the middle section of the cavity was made, which we called a flow-body. The flow-body was designed so that it delivers the gas from the 1/4 inch tubing system before the cavity inlet, to the measurement region at the middle of the cavity with gradual increase in diameter, which matches the width of the sight of view of the LIF optics. Then, gradually decrease the width of the flow-body to matches the 1/4 inch tubing system at the cavity exit. As seen in figure 4.1. The flow-body was made of a 125 mm long aluminium cylinder, with an outer diameter of 33.8 mm. In the middle section there were two 6 mm holes opened to the cavity arms which were required to allow the laser beam to pass and interact with the sample, whilst minimising the mixing between breath samples and the stagnant air in the cavity. As seen in the half-section view of the flow-body in figure 4.1, when viewed from the top, the 1/4 inch OD (4 mm ID) gas inlet tube concavely expands to 25 mm in the middle section where the laser beam interacts with the sample, in a sample width within the field of view of the

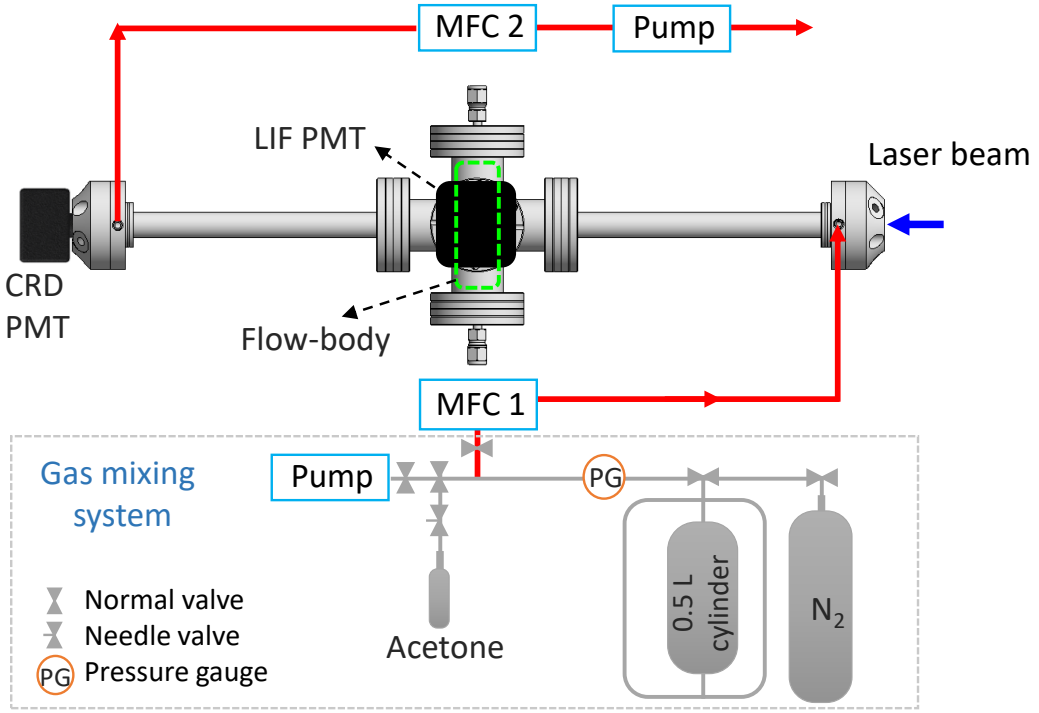

Figure 4.2: Schematic diagram of the CELIF experiment setup showing the acetone–nitrogen gas mixing system and the longitudinal flow setup.

LIF PMT, and then returns to the initial diameter at the gas outlet. When viewed from the side, the gas inlet concavely expands to only 8 mm in the middle section then returns to the initial diameter at the exit. At the top of the flow-body there was a 25 mm hole for the LIF optics to be fitted.

The flow-body was placed inside the 6-way cross, with the LIF optics fitted in it and the LIF PMT extends out from the top flange of the 6-way cross (not shown in figure 4.1). The flow of the gas samples was created by attaching the inlet of the flow-body with a mass flow controller (Alicat, MC-5SLPM) (MFC 1) that controls the pressure of the inlet and keeps it at 1 bar, and the gas outlet of the flow-body is connected to a second mass flow controller (MFC 2) that controls the mass flow rate of the flowing gas. The upstream of MFC 1 was connected to the pressurised gas samples, and the downstream of MFC 2 was connected to a rotary pump.

4.2 Flow CELIF Measurements

4.2.1 Static vs. Flowing Gas CELIF Measurements

Before testing the transverse flow measurements through the flow-body it was essential to first compare CELIF measurements of static gas samples which fill the whole volume of the cavity with CELIF measurements of flowing gas samples through the cavity axis, which fill the same volume, to test whether the flow of gas affects the concentration measurements. Figure 4.2 shows the experiment setup for this test, which was done while the flow-body was inside the chamber, but without actually using it to flow samples transversely. A mixture of acetone–nitrogen was prepared in a 0.5 L gas cylinder by first pumping down the cylinder, then releasing a small amount of gas acetone into it (less than 1 mbar), then topping up the cylinder with 9 bar of gas N_2. The mixture then was left to mix for about 15 minutes with the help of the heated side arms of the mixing cylinder. Next, a CELIF background measurement was made by filling the cavity with 1 bar of N_2. Then, some of the acetone–nitrogen mixture was extended to the cavity and kept stagnant inside at 1 bar and a CELIF measurement was taken. After that, the cavity was cleaned with flushes of N_2. Next, the same gas mixture was flowed through the CELIF device through the cavity axis (longitudinally) and a series of CELIF measurements were taken at different gas flow rates, in the range between 0.3–1 standard litre per minute (slpm).

The results of these measurements are shown in figure 4.3. Although the sample length in the static and longitudinal flow measurements was the same, the CRD and LIF signals of the same gas mixture got stronger with the flow of the gas. The CELIF signal measured while the gas was stagnant in the cavity was clearly smaller than the CELIF signals recorded while the gas was flowing. Also, the CELIF signal started to plateau at a flow rate of at least 0.5 slpm.

To further examine this, two CELIF calibrations were made, one with static samples and one with longitudinally flowing gas samples, at 0.5 slpm flow rate, without changing the LIF or CRD setup between the calibrations. The calibrations were made with a series of dilutions of acetone–nitrogen gas mixtures. The two

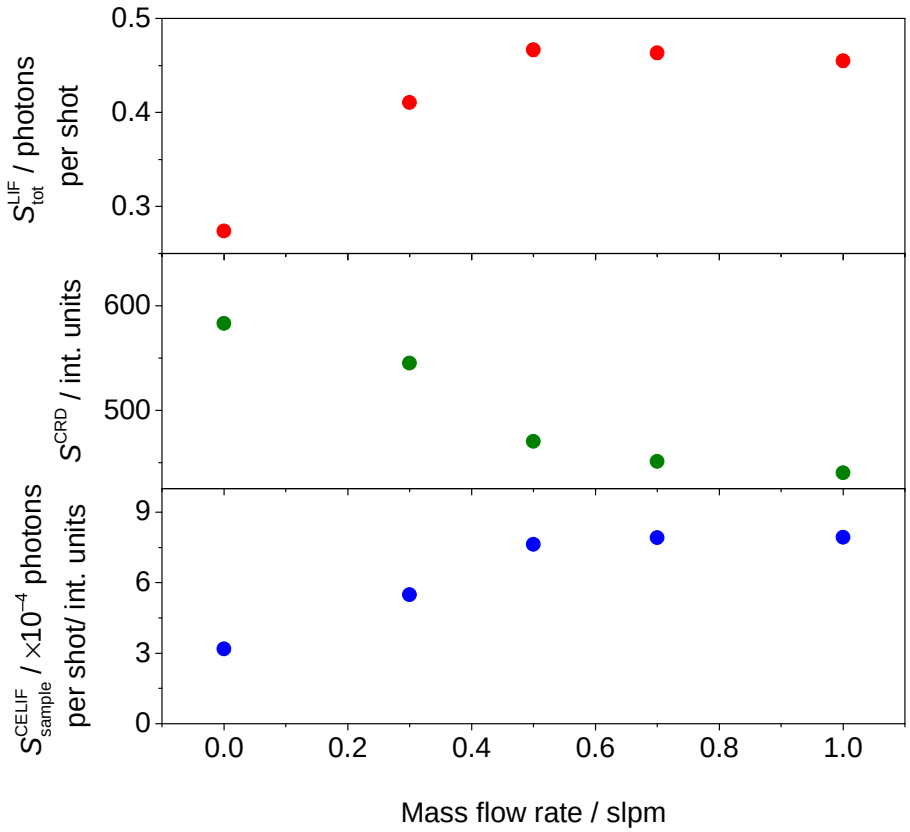

Figure 4.3: LIF, CRD and CELIF signals from static gas versus longitudinally flowing gas samples. Each measurement was an average of 10000 shots. The error bars are from one standard error and are smaller than the symbols.

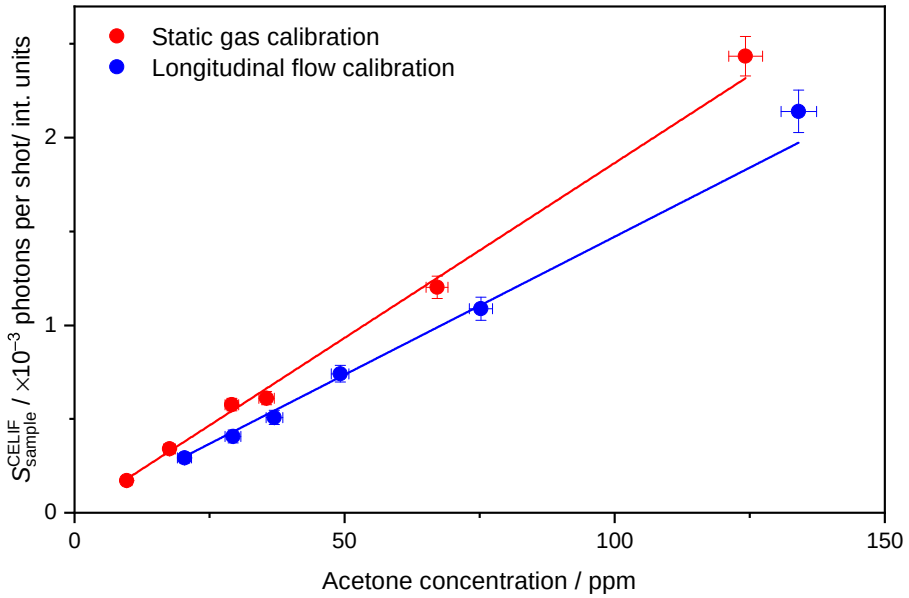

Figure 4.4: CELIF calibration with static samples (red circles) with longitudinally flowing samples (blue circles), with a flow rate of 0.5 slpm. The lines are straight line fit of the data. Each measurement is an average of 1500 shots. The error bars are from one standard error.

calibrations are shown in figure 4.4. The calibration factor measured with the static gas samples was $1.87 \times 10^{-5} \pm 5 \times 10^{-7}$, while the calibration factor measured with the longitudinally flowing gas samples was $1.47 \times 10^{-5} \pm 4 \times 10^{-7}$. The two calibrations disagree with each other.

These tests showed that static CELIF measurements do not reflect the real acetone concentration in a sample. This may be due to optical bleaching of the stagnant acetone molecules in the cavity, which does not occur while flowing the sample as the molecules that interact with the laser get replaced quickly preventing bleaching. Thus, CRD and CELIF measurements must be made with flowing gas samples, which is confirmed by the validation measurements presented in section 4.4.

For the real-time CELIF measurements to be quick and to minimize the residence time of the samples in the CELIF device, gas samples should flow transversely through the flow-body and not through the cavity axis. CELIF signals with longitudinally flowing gas are equal to CELIF signals with transversely flowing gas, although the constituent CRD and LIF signals are different. To confirm this, CELIF

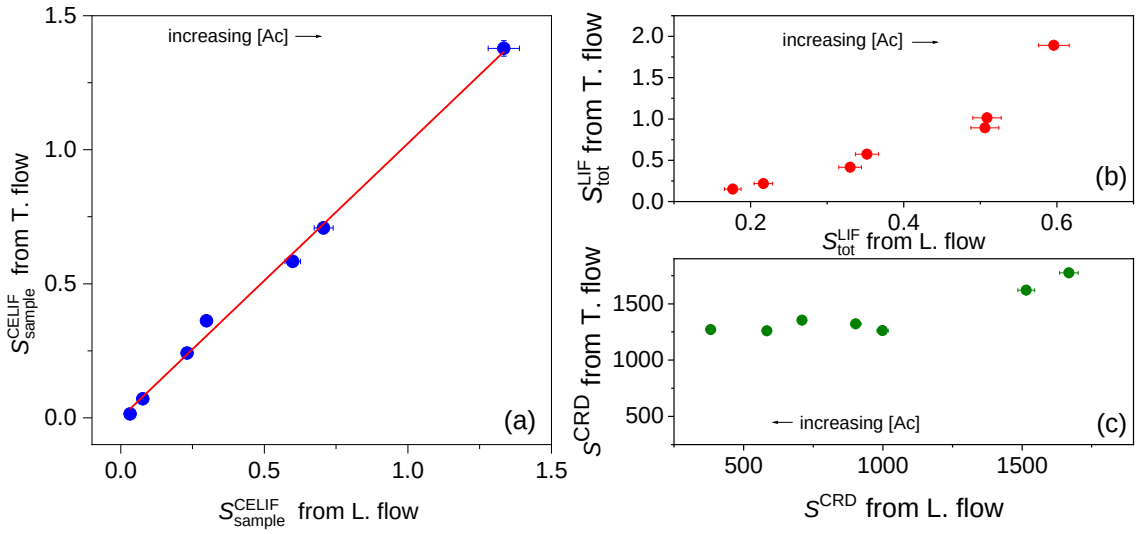

Figure 4.5: Comparison between transverse flow through the flow-body and longitudinal flow of the same gas samples. (a) The blue circles are the CELIF signals, and the red line is a straight line fit of the data. (b) The red circles are the LIF signals. (c) The green circles are the CRD signals. The data were recorded with a sample flow rate of 0.5 slpm, and each measurement was an average of 1500 laser shots. The error bars are from one standard error.

signals of different standard acetone–nitrogen gas mixtures were measured once with longitudinal flow and once with transverse flow, with a flow rate of 0.5 slpm in each flow direction. The measurements of each gas mixture were compared and are shown in figure 4.5 (a). The CELIF signals from transverse flow was plotted together with the CELIF signals from longitudinal flow of the same gas. A linear fit with a slope of 1.02 ± 0.03 proves the agreements between transverse and longitudinal flow CELIF measurements. Figure 4.5 (b) and (c) shows a comparison of the LIF and CRD signals between transverse and longitudinal flow of the same gas samples. It is shown that reducing the sample length with transverse flow preserves the laser intensity at the LIF probe region because there is less absorption in the side arms which strengthens the LIF signal for the same gas sample. It also strengthens the CRD signal which makes it possible to measure the time integrated CRD signals at high acetone concentrations. This makes transverse flow ideal to extend the dynamic range of CELIF measurements.

CRD and CELIF measurements must be made with flowing gas samples. CRD measurements for CELIF calibration must be made with longitudinal flow. Because the flow-body is required to have two holes open to the cavity axis, the sample length at the middle section where the gas interacts with laser beam is not defined, which makes measuring the ring-down time when transversely flowing the gas impossible. Also, the sample length with transverse flow is very small compared to the total length of the cavity which makes transverse CRD measurements not sensitive. On the other hand, as shown above, CELIF measurements benefit from the transverse flow by reducing the residence time of the samples in the device and by extending the dynamic range of the CELIF measurements.

4.2.2 CELIF Dynamic Range

CELIF calibration followed by CELIF measurements of different samples were made to explore the lower and higher limits of detection, dynamic range, of the CELIF device. The experiment setup for the CELIF calibration measurements is shown in figure 4.6. Standard acetone–nitrogen gas mixtures of acetone concentration in the range between 2–100 ppm were used to do the CELIF calibration. The outlet

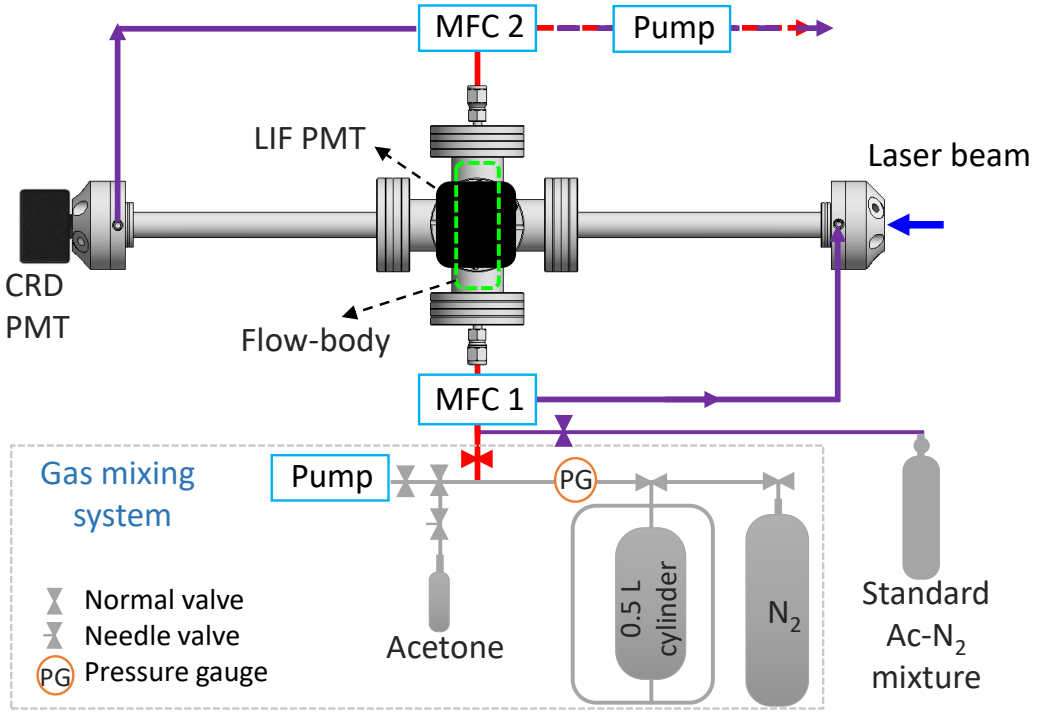

Figure 4.6: Schematic diagram of the CELIF dynamic range experiment setup. The longitudinal flow setup was used in the calibration measurements with standard acetone–nitrogen gas mixtures, and the transverse flow setup was used for the CELIF measurements of various concentrations of acetone–nitrogen gas mixtures.

of the standard gas bottles was connected to the mass flow controller that controls the pressure at the cavity inlet. The outlet of the CELIF device was connected to the second mass flow controller that controls the flow rate of the gas through the cavity. Each CELIF calibration measurement was made by first measuring the laser independent background, γ, by blocking the laser then recording the LIF signal. Then measuring the background CELIF signal for an acetone-free sample, which was measured by longitudinally flowing 1 bar of N_2 at 0.5 slpm. Then, the sample CELIF signal was measured by longitudinally flowing some of the acetone–nitrogen gas mixture at a pressure of 1 bar and a flow rate of 0.5 slpm. The sample CELIF measurement was recorded after 1 minute of the gas flow to ensure that the cavity pressure which was controlled by the mass flow controller was stable. Each background and sample CELIF measurement was an average of 1500 laser shots. The cavity was flushed with flowing N_2 after each measurement.

Next, to produce a calibration curve, as shown in figure 4.7, the CELIF signals were plotted against the acetone concentration as measured by CRD. Then, a straight line with zero intercept was fitted to the data, yielding a calibration factor $\mathcal{K}' = 1.49 \times 10^{-5} \pm 3 \times 10^{-7}$. The 3σ limit of detection of the cavity ring-down measurements was calculated using Eqn 2.2.5, and was 2 parts per million (ppm), when averaging over every 1500 laser shots in 100 ms. The higher limit of detection of the CRD measurements was estimated from the ability to fit a CRD transient to a one-phase exponential decay to measure the ring-down time, which gave acetone concentration of 390 ppm as the higher limit.

Next, a high concentration acetone–nitrogen mixture was prepared in a 0.5 L gas cylinder by first pumping down the cylinder, then releasing some of the gas acetone into it, then topping up the cylinder with 9 bar of gas N_2. The mixture then was left to mix for about 1 hour with the help of the heated side arms of the mixing cylinder. The gas line was connected to the mass flow controller and the flow-body inlet, and the flow-body exit was connected to the second mass flow controller. Then, γ was measured by blocking the laser and recording the LIF signal, and the background CELIF signal was measured by transversely flowing 1 bar of N_2 through the flow-body at 0.5 slpm. After that, 1 bar of the acetone–nitrogen mixture was released

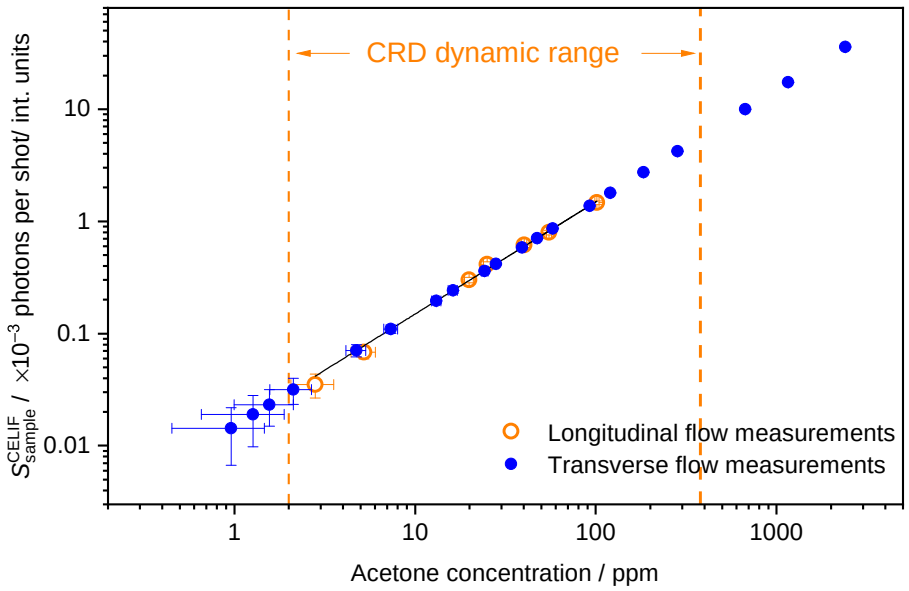

Figure 4.7: The open orange circles are the CELIF calibration measurements taken with longitudinal flow of standard acetone–nitrogen gas mixtures. The acetone concentrations for these measurements were take from CRD. The blue circles are the CELIF measurements taken with transverse flow of acetone–nitrogen gas mixtures. The acetone concentrations for these measurements were take from the CELIF calibration. Each measurement was an average of 1500 laser shots. The error bars are from one standard error.

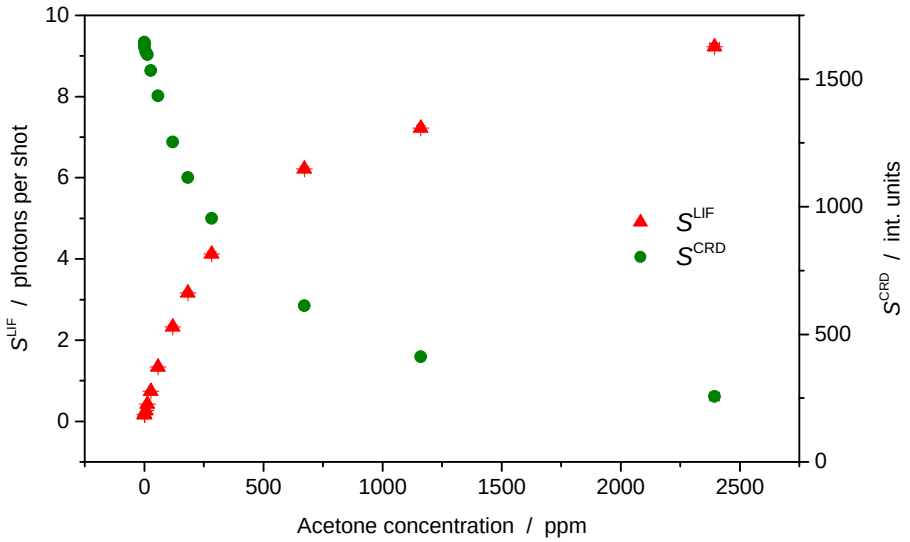

Figure 4.8: The photon counted LIF signals (red triangles), and the time integrated CRD signals (green circles) of the CELIF dynamic range measurements, plotted against the acetone concentration. The measurements shows that even at acetone concentrations as high as 2000 ppm, the photon counting is still valid with the under-counting correction, and the CRD signal is still integratable.

into the cavity through the flow-body with a flow rate of 0.5 slpm, and after 1 minute of the gas flow a CELIF measurement was recorded which was an average of 1500 laser shots. Next, the cavity was flushed with N_2, and the rest of the gas mixture was diluted by topping it up with N_2 and was left to mix for about 15 minutes. Then, another set of background and sample CELIF measurements were taken as above. The procedure was repeated many times until the limit of detection was reached.

Each CELIF signal from the transverse flow of the samples was converted into acetone concentration using the calibration factor, $\mathcal{K}'$, and was appended to the CELIF calibration graph as shown in figure 4.7. The acetone concentration CELIF limit of detection was calculated from Eqn 2.3.36, and was 1.6 ppm, which agrees with the dilution measurements as the error bars started to overlap at acetone concentrations below 2 ppm. Figure 4.8 presents the LIF signals in units of photons per shot and the time-integrated CRD signals in units of int. units, the measurement unit of the analog integrator, for the transverse CELIF measurements. It shows

that even at acetone concentration as high as 2000 ppm, the CRD signal was still integratable and the LIF signal was still in the photon counting regime after applying the under-counting correction as detailed in chapter 2. Thus, the transverse flow of the gas through the flow-body gives a higher limit of detection of the CELIF device of more than 2000 ppm, winning over the cavity ring-down measurement and covering the required dynamic range for the CELIF device.

The Elforlight laser used in these measurements was not performing very well, as the averaged laser power was decaying over time. Also, the laser beam shape was not a single Gaussian spot, which meant throwing away a large portion of the laser energy when focusing the beam into the cavity. By the time the CELIF dynamic range measurements were taken, the laser pulse energy was reduced to only about 0.02 μJ per pulse. Increasing the laser pulse energy will lower the limit of detection of the CELIF measurements. Chapter 6 presents the work with another more powerful laser which was used to investigate the limit of detection of the CELIF device.

4.3 Response Time of the CELIF Instrument

For this device to be clinically accepted, the acetone CELIF measurement must be able to follow the real-time breathing pattern, by responding quickly to any change in the acetone concentration. The CELIF signal must rise and reach the maximum acetone concentration in less than 1 s, then fall and return to the baseline level before the next breath arrives. This section presents the modifications made to the flow-body design and the sampling method to improve the response time (rise and fall time) of the CELIF measurement. The rise time of the measurement is defined as the time taken for the signal to rise from 10% to 90% of the steady state signal, and the fall time of the measurement is the time taken for the signal to fall from 90% to 10% of the steady state of the signal.

4.3.1 Performance of Flow-body-1

The performance of the flow-body shown in figure 4.1, flow-body-1, was tested using a mixture of acetone in air. The gas sampling setup was changed to be able to create

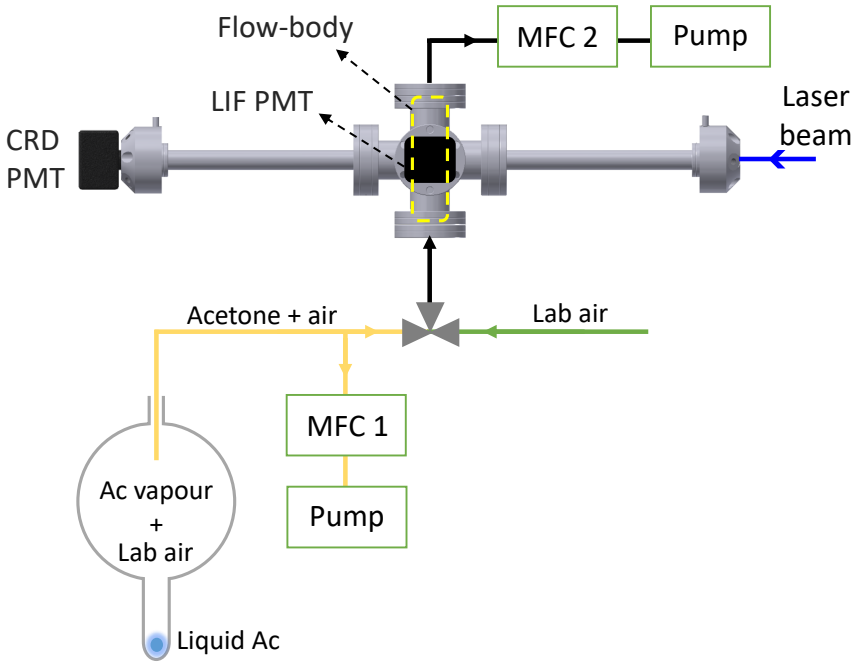

Figure 4.9: Schematic diagram of the acetone–air gas sampling method using a flow system and a 3-way valve to switch between air and the acetone–air mixture.

a continuous stream of gas mixture at atmospheric pressure, without the need for premixing or worrying about controlling the pressure of the flow-body inlet. As shown in figure 4.9, a mixture of acetone vapour and air was created by putting a few drops of liquid acetone in a 3 L glass bulb which was open to the atmosphere. A sampling tube was inserted into the glass bulb, while the other end of the tube was connected to a T-piece. One side of the T-piece was connected to a mass flow controller (MFC 1), which was connected to a pump, to give a continuous flow of 5 slpm through the sampling tube, and prevent accumulation of acetone vapour in the tube. The other side of the T-piece was connected to a 3-way valve, which allowed either lab air or a gas sample to flow through the flow-body, with a flow rate of 0.5 slpm controlled by the mass flow controller at the exit of the flow-body (MFC 2).

CELIF Response Time with Flow-body-1

A CELIF background measurement was made by measuring the laser independent background, γ, by blocking the laser then recording the LIF signal. Then measuring

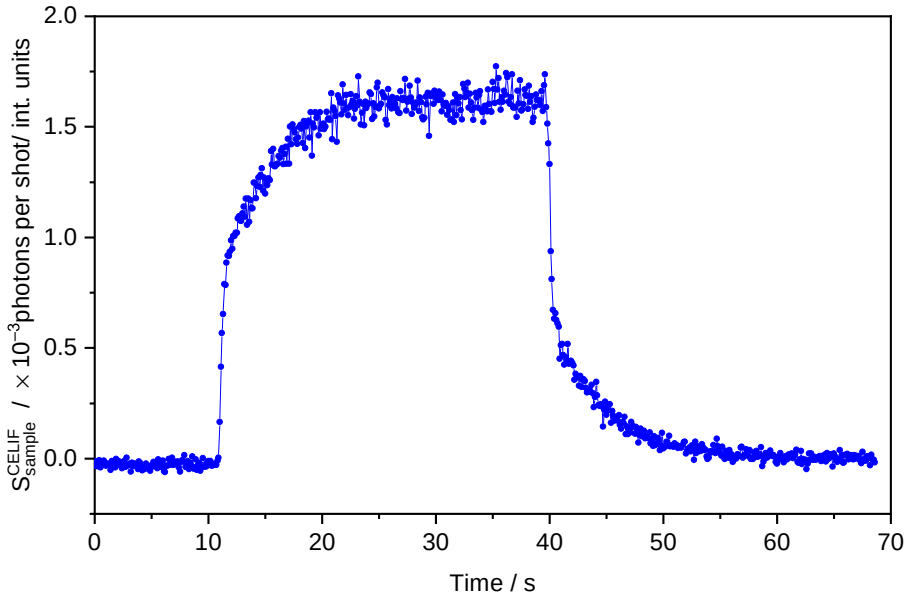

Figure 4.10: Real-time CELIF signal taken using flow-body-1. Each measurement was an average of 1500 laser shots and was recorded with a 100 ms time interval.

the background CELIF signal by flowing lab air through the flow-body. Next, the LabView program was set to record the CELIF signal every 100 ms by averaging 1500 laser shots, while the 3-way valve was set to flow lab air to record a baseline for the measurement, then after a few seconds, the 3-way valve was turned to the sample side and allowing the sample to flow for a few seconds before turning the 3-way valve back to the lab air side. The CELIF measurement was stopped when the baseline turned to the initial value.

The result of this measurement is shown in figure 4.10. The baseline from 0–12 s indicates air flow, while the rise in the CELIF signal followed by the plateau indicates the acetone–air sample flow. Then the fall of the signal at 40 s and the baseline after that indicates the switching of the 3-way valve to the lab air side. The steady state of the acetone CELIF signal confirms that the gas sampling method shown in figure 4.9 provides constant concentration of acetone in air and proves that this method is usable.

The rise time of the CELIF signal was 6.2 ± 0.2 s and the fall time was 6.6 ± 0.2 s. Therefore, at least 12 s was needed for a single acetone measurement to be made using this flow-body. The rise and fall time values are likely to be linked as they are

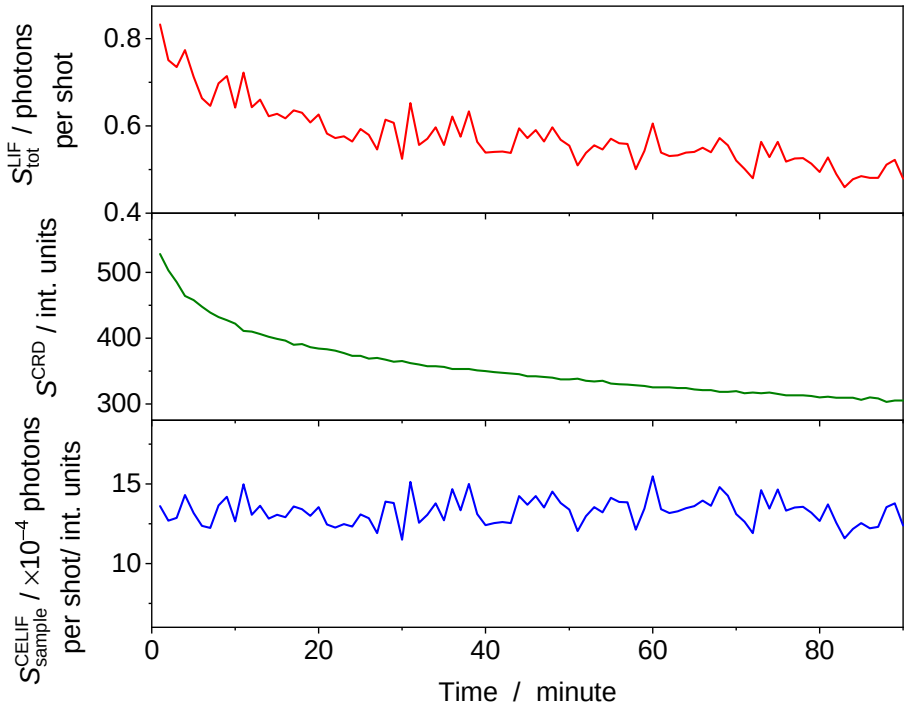

Figure 4.11: Time lapse acetone CELIF measurement made using flow-body-1 with a sample flow rate of 0.5 slpm. The measurements were recorded with a 1 minute time interval and each measurement was an average of 1500 laser shots.

similar within experimental errors. The manual switching of the 3-way valve from acetone–air sample to lab air, and vice versa, takes less than 1 s. Also, the sampling method used in this measurement provided constant acetone concentration. Therefore, the long response time of the CELIF measurement was likely to be caused by issues of the flow system, particularly, the design of the flow-body. An investigation of this issue is presented in section 4.3.2.

Sample Diffusion Through Side Arms with Flow-body-1

Time lapse acetone CELIF measurements were made to test whether the gas samples flowing thought the flow-body diffuse into the side arms of the cavity, or if the samples being diluted by the stagnant air in the cavity side arms. A mixture of acetone in air was made using the method shown in figure 4.9. The mixture was flowed through the flow-body at flow rate of 0.5 slpm for more than 1 hour, while the LabView program was recording the CRD, LIF and CELIF signals every 1 minute,

averaging 1500 laser shots for each measurement.

The results are shown in figure 4.11. Both, the time-integrated CRD signal and the LIF signal decayed with time. As the gas extended into the side arms through the two laser holes in the flow-body, the sample length increased and the light intensity at the middle section of the cavity decreased, which caused both the CRD and LIF signals to decay with time. Even though the sample diffused into the side arms of the cavity, the CELIF signal was constant for the entire period of the experiment, which also confirms that the sampling method used in figure 4.9 is reliable.

Having two holes in the middle of the flow-body is necessary for the laser to pass through, however, this causes the sample to diffuse through these two holes and extend into the side arms of the cavity. This issue must be considered when designing the flow system, and doing acetone breath measurement.

4.3.2 Computational Fluid Dynamics Simulations

To investigate the reason behind the long rise and fall time of the CELIF measurement made using flow-body-1, and to find a suitable solution to this issue, Computational Fluid Dynamics (CFD) simulations were performed to visualise the theoretical flow through the flow-body. Autodesk CFD was used for this purpose. These CFD simulations of the different designs of the flow-body were made by another group member [62].

To run a CFD simulation for an object, a CAD drawing of this object must be created and imported into the CFD software. The materials of the various parts of the CAD object must be assigned including the flow volume. The boundary conditions of the flow system must be set including the volume flow rates of the sample gas at the inlets and the static pressure on the outlets. The samples used in the CELIF experiment contained only a small concentration of acetone, which would have a negligible impact on the flow of the gas. Thus, the fluid material "air" was used in all of the simulations. The following step was to create a mesh for the system for the 3D simulation. The mesh is where the simulation is actually performed, which is a series of tetrahedral elements which approximate the geometry of the CAD object. The partial differential equations used by the CFD software to

describe the flow of fluid do not have solutions for complex systems, therefore the system is divided into smaller subsystems within which analytical solutions can be found. A fine mesh will match the geometry and result in an accurate simulation, however this costs a large amount of computer memory and long computational time. A coarse mesh will result in a fast simulation, but inaccurate results.

The general method used to create a mesh for an object in the CFD software for the simulations performed in this project is as follows: first, using the auto-size function a simple coarse mesh was created. Then, the size adjustment was used to refine the mesh, which increases or decreases the size of the mesh elements by up to a factor of 5. Using this, the mesh was refined to give an element count between one and two million. Next, "surface refinement" and "gap refinement" were enabled to refine the mesh on the surfaces and between gaps in the CAD geometry. The final step was to adjust the wall layer settings. A wall layer is a mesh along the wall of the flow volume used to simulate the boundary layer. Therefore, it is important that the wall layer is thick enough and contains enough layers to resolve the whole boundary layer. The number of layers within the wall layer settings was set to 9, the layer factor, which determines the layer thickness, was set to 0.2 and the layer gradation, which controls the rate of growth of the wall layers, was kept at the automatic setting. This method generated the initial mesh for each CFD simulation.

Certain control settings had to be chosen to run the CFD simulations, such as if the flow is laminar or turbulent and if the fluid is incompressible. A flow is characterized to be laminer (smooth) or turbulent (rough) by a dimensionless parameter called Reynolds number: $Re = (\rho\, d\, \nu)/\eta$, where ρ and η are the fluid's density and viscosity, d is the diameter of the flow channel, and ν is the flow velocity. Values of $Re < 2000$ predict a laminar flow, whereas values of $Re > 2500$ usually indicate that flow will be turbulent [63]. In a laminar flow system, some vortices, or localized swirling, can separate from the central streamlines within a flow channel, which unlike turbulent flow, fluid in vortices is composed of slowly moving currents and streamlines. The Mach number M is a dimensionless quantity representing the ratio of flow velocity to the speed of sound. At values of $M < 1$, the compressibility of the fluid can be ignored [64].

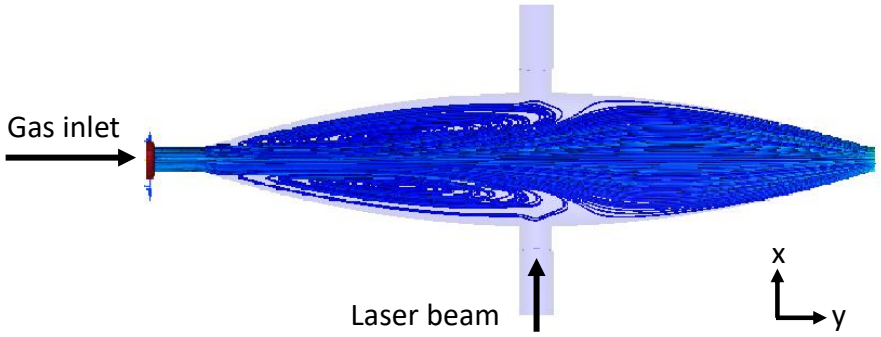

Figure 4.12: The trace profile mapping the paths the sample gas takes in flow-body-1, with a sample flow rate of 0.5 L/min.

The values of the Mach and Reynolds numbers of our flow system are significantly lower than the Mach and Reynolds number at which a fluid beings to show compressibility and turbulence, respectively. Therefore, it was determined that the simulations will use the approximations that the flow is laminar and incompressible to reduce the computational cost.

The simulation results must be mesh independent. Thus, mesh adaptation was enabled to ensure this was true for the simulations. This is a program which analyses the results and refines the mesh where needed. The results after running mesh adaptation were always mesh independent.

CFD Simulation of Flow-body-1

In order to identify the origin of the long rise and fall times of the CELIF signal measured with flow-body-1, a CFD simulation was performed on this flow-body. The CAD geometry used for this simulation is found in figure 4.1, except the holes for the LIF optics were removed as only the basic shape of the flow-body was being studied, and closed arms were added to simulate the optical cavity. The simulation was performed as described in the previous section. The boundary conditions for the flow were a volume flow rate of 0.5 L/min placed on the inlet, and a static gauge pressure of 0 Pa placed on the outlet.

A set of traces spread evenly over the inlet were plotted to see the path the gas takes as it enters the flow-body. The traces are a packet of data points which enter the system and map out the path the gas takes based on the velocity of the fluid.

The path of the traces of flow-body-1 are shown in figure 4.12. The traces show that large vortices formed either side of the main flow. The vortices formed here due to the sharp increase in the width of the flow-body after the inlet, resulting in boundary layer separation. No vortices formed in the perpendicular plane as the width increases much more gently. The boundary layer split the sample flow into three distinct regions: the two vortices and the main flow tube, where the flow is laminar, and is shaped by both the walls of the flow-body and the vortices. The widest section of the flow tube was positioned at about 3 cm to the right of the middle of the flow-body. Within the vortices, the traces had an average residence time of 24.6 $\pm$ 0.9 s, with the residence time defined as the time a trace stays in the system before exiting through an outlet. This is about twice as much as the measured rise and fall time of the CELIF measurement made with flow-body-1. This is likely to be caused by the simplification of the design made for the simulations. The long residence time of the traces in the vortices is most likely the source of the long rise and fall times of the acetone CELIF measurement. Therefore, by removing these vortices, the CELIF measurement should be fast.

4.3.3 Flow-body-2 Design

Based on the CFD simulation of flow-body-1, another flow-body, flow-body-2, was designed. Flow-body-2 was designed with an inner volume similar to the shape of the main flow tube found in the simulation of flow-body-1. The CAD drawing for this new design is shown in figure 4.13. In the x-y plane, there is a smooth widening of the flow-body, with a convex shape, in order to prevent boundary layer separation. In the z-y plane, flow-body-2 was kept unchanged from flow-body-1 as no vortices were found in this plane. There is a smooth concave increase in the flow width, with the widest point lying in the middle of the flow body. This flow-body includes two side flow channels to be used to flow air to remove any sample that would get trapped in a vortex in order to maintain a smooth flow profile, and to prevent the sample from diffusing into the side arms of the cavity. Adding these two channels required the modification of the main flow tube found in the simulation of flow-body-1. This included increasing the width of the flow volume after the

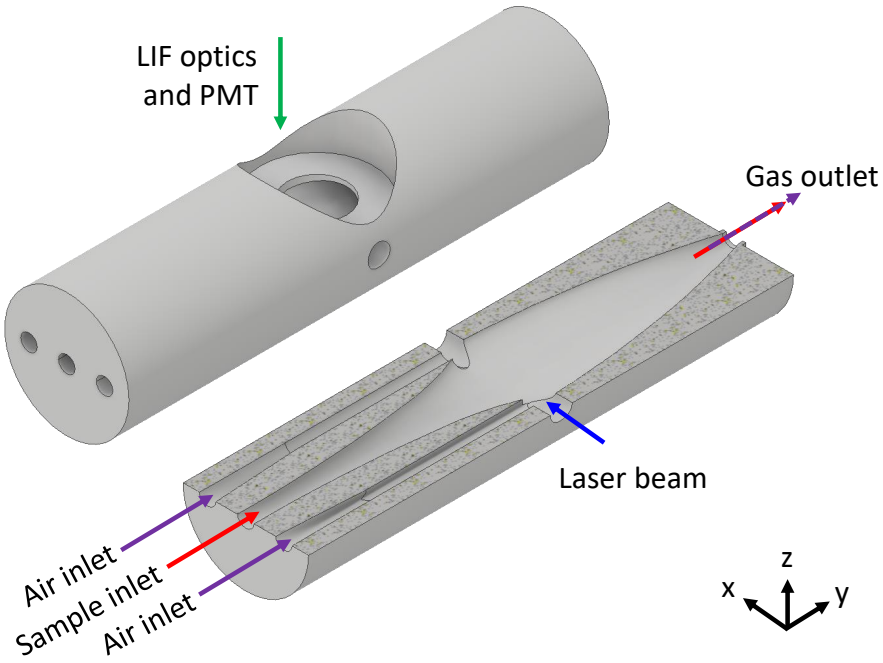

Figure 4.13: CAD drawing showing a full view and a half section view of flow-body-2.

cavity. They were designed so that the air flow in the side channels would join the sample flow next to the cavity holes. This is so that at the point of measurement, minimal mixing would occur, reducing any effect the side channel flow would have on the sample concentration. This flow-body prototype was 3D printed from a plastic material (PLA polylactic acid) after being studied with CFD simulations.

4.3.4 CFD Simulation of Flow-body-2

The design of flow-body-2 shown in figure 4.13 could not be meshed with the CFD software because of the complex design of the side channels. Thus, for the CFD simulation only, the geometry of flow-body-2 was simplified as shown in figure 4.14. This included using cylindrical side channels and increasing the gap between the side channels and the main flow at the point they meet. To fit the side channels into the system, their diameter had to be reduced to 3 mm and the width of the flow body after the cavity had to be increased.

Similar CFD simulation to that of flow-body-1 was performed on the simplified flow-body-2. First, only the main flow tube was being studied, so no volume flow rate boundary condition was placed on the side channel inlets. The trace profile

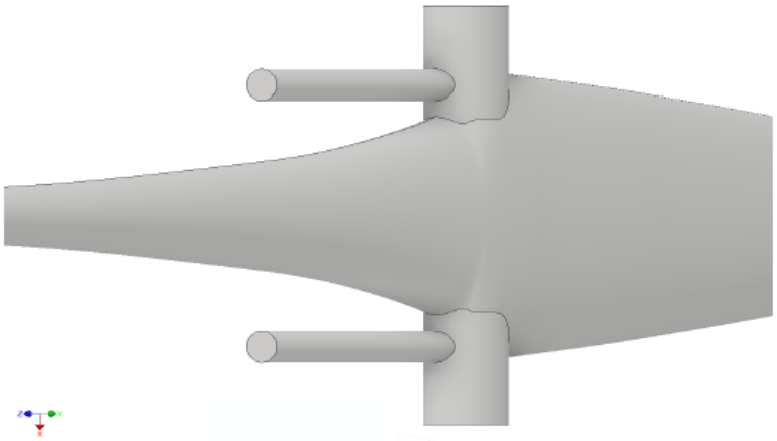

Figure 4.14: CAD drawing showing a simplified design of flow-body-2 for the CFD simulations.

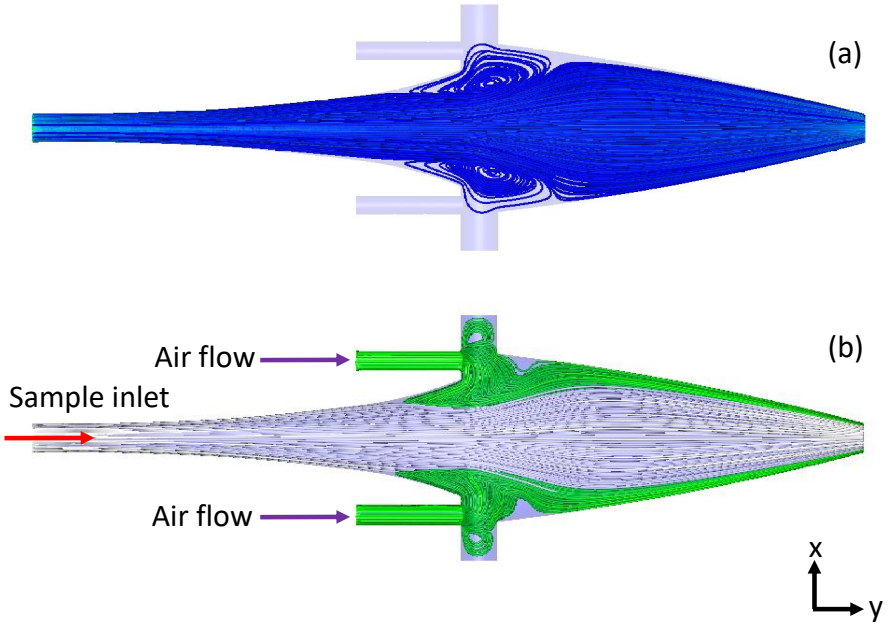

Figure 4.15: The trace profile mapping the paths the sample gas takes in flow-body-2, with a sample flow rate of 0.5 L/min, (a) with no side channel flows, and (b) with side channel flow rate of 0.013 L/min through each channel.

mapping the flow through flow-body-2 is shown in figure 4.15 (a). It shows that small vortices form in the edges of the flow at the middle of the flow-body. This is likely to be caused by the modification of the design and by increasing the width of the flow region after the cavity. However, the actual 3D printed flow-body does not have the steep increase in the width, thus should have smaller vortices.

Next, the effect of air flow through the side channels was studied using CFD simulations. The magnitude of the side channel flow rate was chosen so that the average velocity of the sample at the middle of the flow matches the velocity of the air in the side channels. From the previous simulations it was found that the averaged velocity of the sample at a sample flow rate of 0.5 L/min was 3 cm/s. Using this and the cross section area of the side channel, the flow rate at the inlet of each side channel was set to 0.013 L/min. The trace profile mapping the flow through the main flow tube and the side channels of flow-body-2 is shown in figure 4.15 (b). It shows that the side channel flow allows the sample to flow smoothly through the system by preventing the formation of vortices in the sample flow by filling the region where boundary layer separation would occur. This should correspond to a faster rise and fall times of CELIF signals. Because the width of the sample flow was reduced by the side channel flows, the width of the LIF optics hole in flow-body-2 was reduced to 16 mm (compared to 25 mm in flow-body-1). This is to reduce the sight of view of the LIF PMT so that only fluorescence from the acetone molecules can be detected.

4.3.5 Performance of Flow-body-2

CELIF Response Time with Flow-body-2

A CELIF response time test was made using flow-body-2, first without flowing air through the side channels, and using the same experiment and sampling method as what was used with flow-body-1. The inlets of the side channels were covered to prevent any flow through them. The CELIF signal from this measurement was plotted together with the CELIF signal measured with flow-body-1 as shown in figure 4.16.

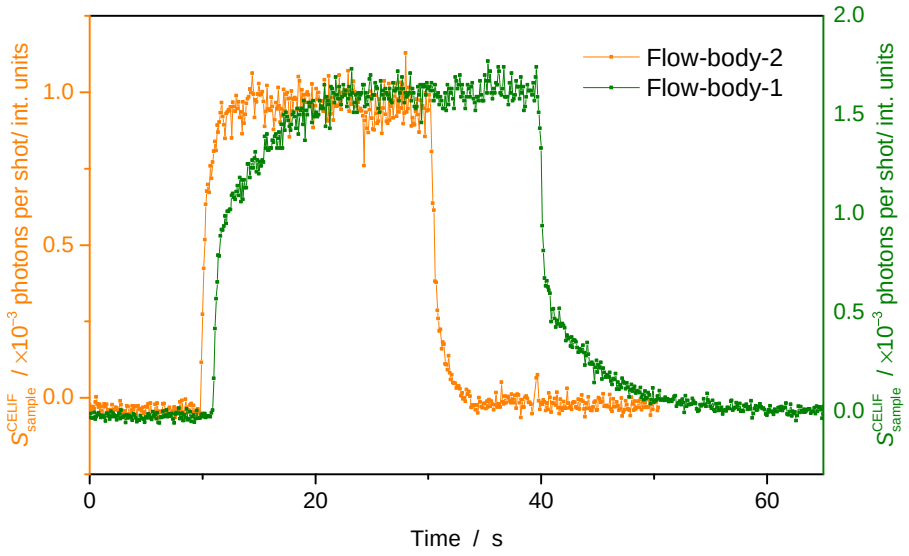

Figure 4.16: Real-time CELIF signal taken using flow-body-2 (orange curve) compared to the similar measurement taken with flow-body-1 (green curve), both with no side channel flows. Each measurement was an average of 1500 laser shots and was recorded with a 100 ms time interval.

The rise and fall times of the CELIF signal when measured with flow-body-2 were 1.5 ± 0.1 s and 1.6 ± 0.2 s respectively, which is despite not flowing any air through the side channels, a significant improvement from flow-body-1.

The Effect of the Side Channel Flows

In order to test the effect of the side channel flows, the sampling method presented in figure 4.9 had to be slightly modified. As shown in figure 4.17, (MFC 1) was attached to the inlet of the side flow channels of flow-body-2 and was set to flow air at a flow rate of 0.05 slpm (0.025 slpm through each channel). The continuous sample gas flow from the glass bulb was maintained by connecting the sampling tube to a shut off valve, valve (b), followed by the pump. Valve (b) was partially open to set the flow rate to about 5 slpm. It was found that turning the 3-way valve from air to sample and vice versa, causes a quick pressure drop in the cavity as the middle of the 3-way valve is a dead volume. This causes a delay of a few seconds for the cavity to recover the atmospheric pressure. Thus, another shut off valve, valve (a), was added to the lab air side and was slightly restricting the air flow to aid in

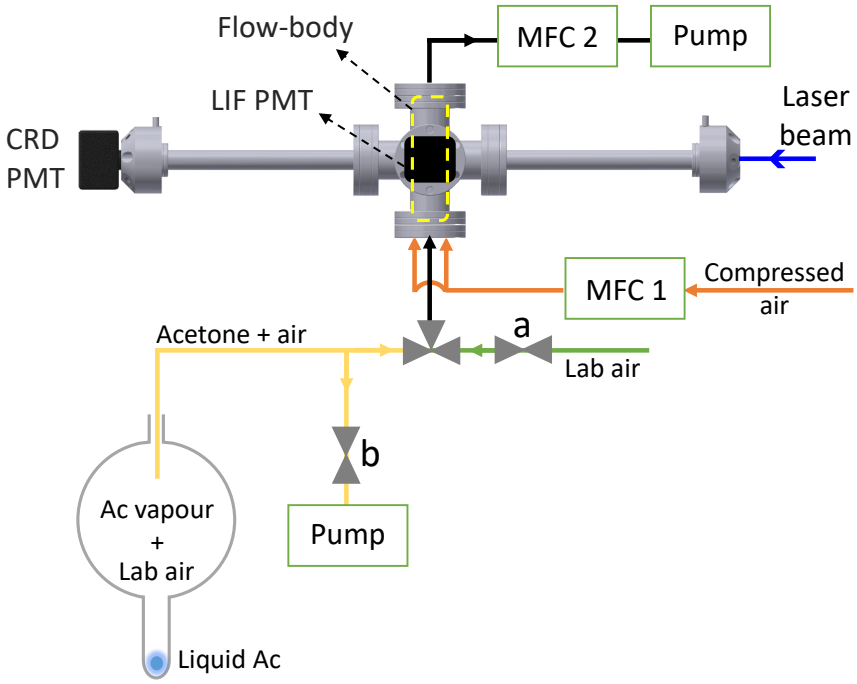

Figure 4.17: Schematic diagram of the acetone–air gas sampling method using a flow system and a 3-way valve to switch between air and the acetone–air mixture. The inlet mass flow controller was used to control the flow rate of the side channel flows.

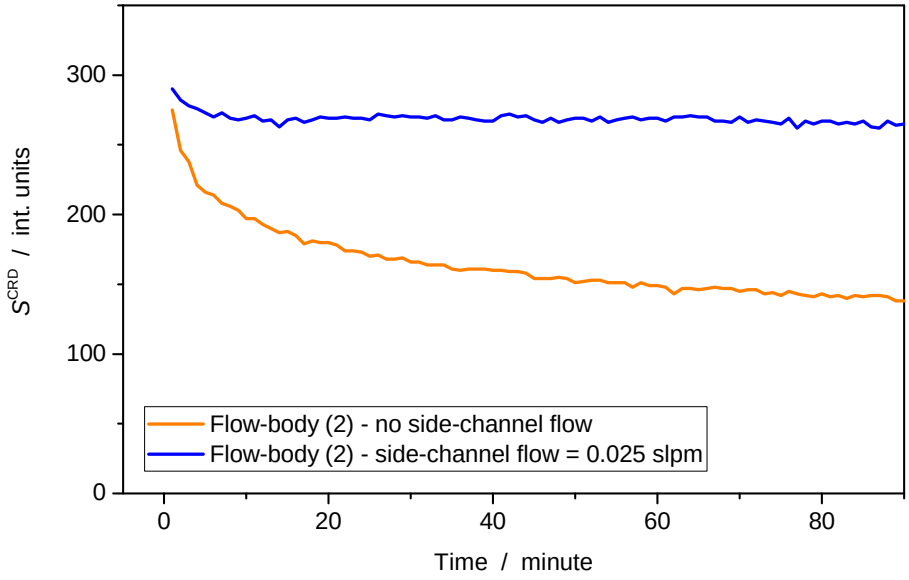

Figure 4.18: Time lapse acetone CELIF measurement made using flow-body-2 with a sample flow rate of 0.5 slpm, with no side channel flows (orange curve), and with 0.025 slpm through each channel (blue curve). The measurements were recorded with a 1 minute time interval and each measurement was an average of 1500 laser shots.

maintaining stable pressure when turning the 3-way valve. The flow-body exit mass flow controller (MFC 2) was set to flow the gas at flow rate of 0.55 slpm, where the main 0.5 slpm is for the sample flow, and 0.05 slpm is for the side channel flows.

Time lapse acetone CELIF measurements were made to test whether the gas samples flowing through flow-body-2 diffuse into the side arms of the cavity. A mixture of acetone in air was made and was flowed through the flow-body at a flow rate of 0.5 slpm, first with no side channel flows, for more than 1 hour, while the LabView program was recording the CRD, LIF and CELIF signals every 1 minute, averaging 1500 laser shots for each measurement. This measurement was repeated with flowing air through the side channels at a flow rate of 0.025 slpm through each channel.

The results are shown in figure 4.18. Similar to what happened with flow-body-1, when there were no side flow channels, the CRD signal quickly decayed as the gas extended into the side arms through the two laser holes in the flow-body. However, when flowing the sample along with flowing air through the side channels the CRD

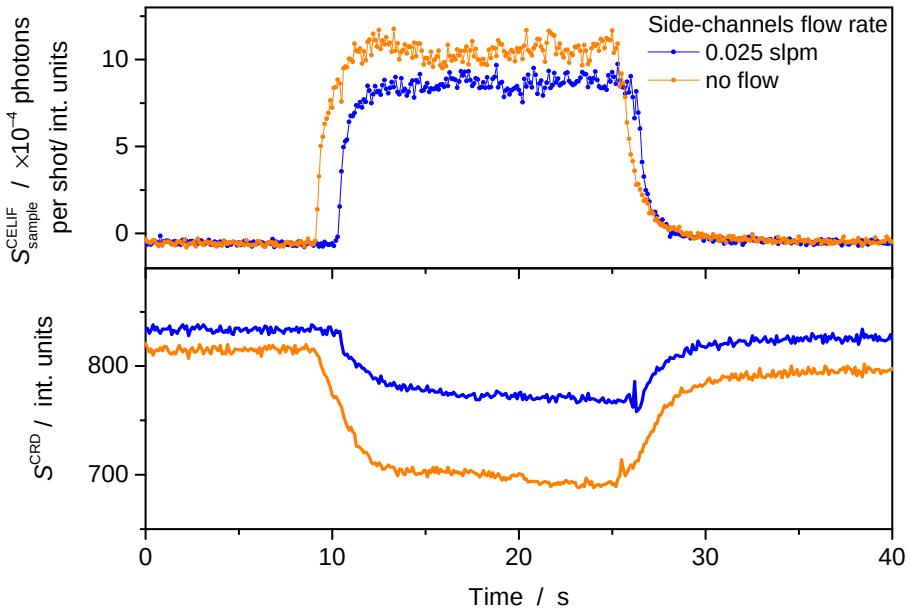

Figure 4.19: Real-time CELIF and CRD signals taken using flow-body-2, once with side channel flow of 0.025 slpm through each channel (blue curve), and once with no side channel flows (orange curve), both with no side channel flows. Each measurement was an average of 1500 laser shots and was recorded with a 100 ms time interval.

signal decayed for only the first 10 s of the sample flow then maintained a smooth flow with constant CRD signal. This suggests that the side channel flow helps in constraining the sample in the middle of the flow-body but not completely preventing the diffusion into the side arms. Faster flow rate through the side channels caused mixing of the air with the sample and reducing the sample concentration.

Next, the effect of the side channel flow on the CELIF measurement was tested. Using the sampling method shown in figure 4.17, two CELIF response time measurements were made, one with side channel flow, and the other one with no side channel flows. Both measurements were made using the same gas mixture and were made successively. These two measurements are plotted together as shown in figure 4.19. While the side channel flow did not improve the rise and fall time of the CELIF measurement, it clearly caused a reduction in the acetone concentration as measured by the CELIF signal. This is likely to be caused by how the side channel flows joins the sample flow and then mixing with and diluting the sample. Further-

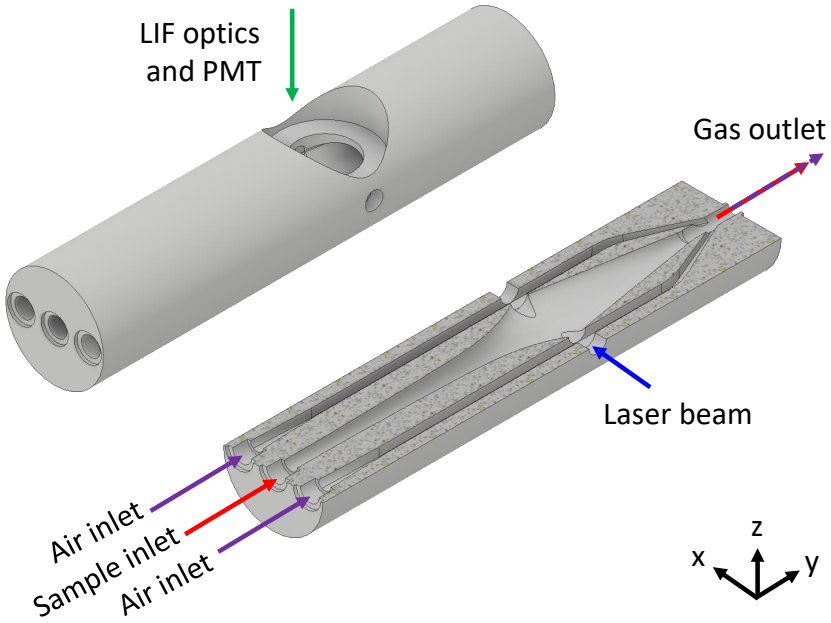

Figure 4.20: CAD drawing showing a full view and a half section view of flow-body-3.

more, the CRD signal of the measurement with side channel flows recovers faster than the CRD signal of the measurement without side channel flows when switching the 3-way valve to air after flowing the acetone mixture. This suggests that the side channel flows helps in reducing the amount of the sample gas diffusing into the side arms of the cavity, and agrees with the results of the diffusion test. Also, shown in the CRD signals, at about $t = 26$ s the effect of the 3-way valve switching on the pressure of the cavity, which should be taken into account when measuring the response time of the CELIF instrument.

The speed of the CELIF measurement with flow-body-2 showed significant improvement compared to flow-body-1, however, the required fast response time (less than 1 s) was not achieved. Even though the side channel flow proved to reduce the amount of the sample diffusing into the side arms, it caused reduction of the sample concentration. Taking these issues into account, a third flow-body was designed as discussed in the following section.

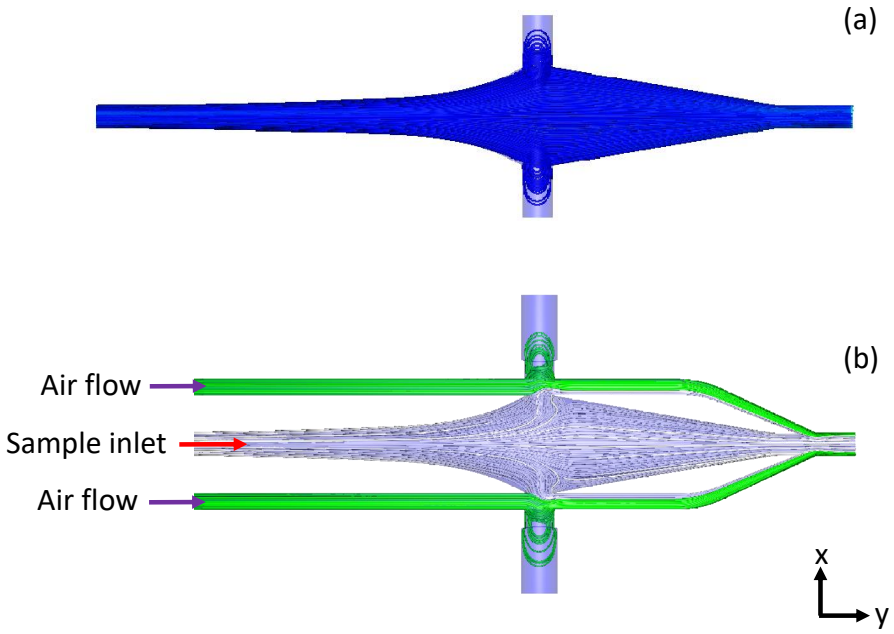

Figure 4.21: The trace profile mapping the paths the sample gas takes in flow-body-3, with a sample flow rate of 0.5 L/min, (a) with no side channel flows, and (b) with side channel flow rate of 0.02 L/min through each channel.

4.3.6 Flow-body-3 Design

The vortices free flow shape found in the CFD simulations of flow-body-1 was modified in flow-body-2 to fit in the side flow channels, which caused the formation of vortices in the sample flow in flow-body-2. The design of the new flow-body, flow body-3, is shown in figure 4.20. This new flow-body was designed from the exact vortices free flow shape found in figure 4.12. To prevent the sample flow from diffusing into the side arms of the cavity, this flow-body also included side channels to create a barrier between the main sample flow and the cavity arms. The side flow channels were designed to run parallel to the main sample flow, and join the sample just before the gas outlet to reduce the chances of mixing between the air and the sample at the measurement region.

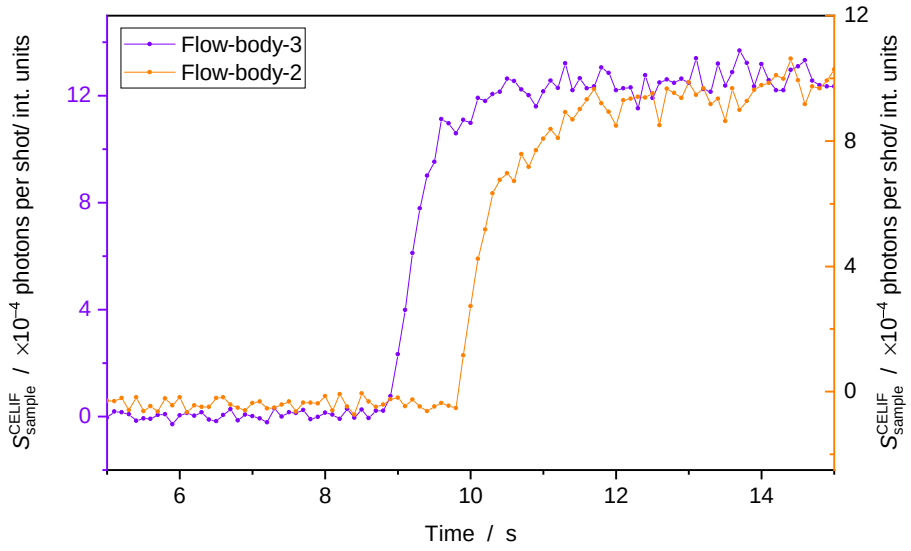

Figure 4.22: Real-time CELIF signal taken using flow-body-3 (purple curve) and compared to the similar measurement taken with flow-body-2 (orange curve), both with no side channel flows. Each measurement was an average of 1500 laser shots and was recorded with a 100 ms time interval.

4.3.7 CFD Simulation of Flow-body-3

CFD simulation similar to the previous simulations was run for this flow-body. The flow rate boundary condition for the sample inlet was set to 0.5 L/min, and the side channel flow rate was determined using the same method used with flow-body-2 and was set to 0.02 L/min through each channel. The boundary condition for the gas outlet was set to 0 Pa gauge pressure. Figure 4.21 shows the traces which map the paths for the sample and side channel flows. The traces show that no vortices are formed in the sample flow, and that no mixing occurs between the sample flow and the side channels flow at the middle of the flow-body. The traces show that the sample would fill the total width of the main flow volume, thus, when this flow-body was 3D printed from PLA plastic the LIF optics hole was set to be 19 mm.

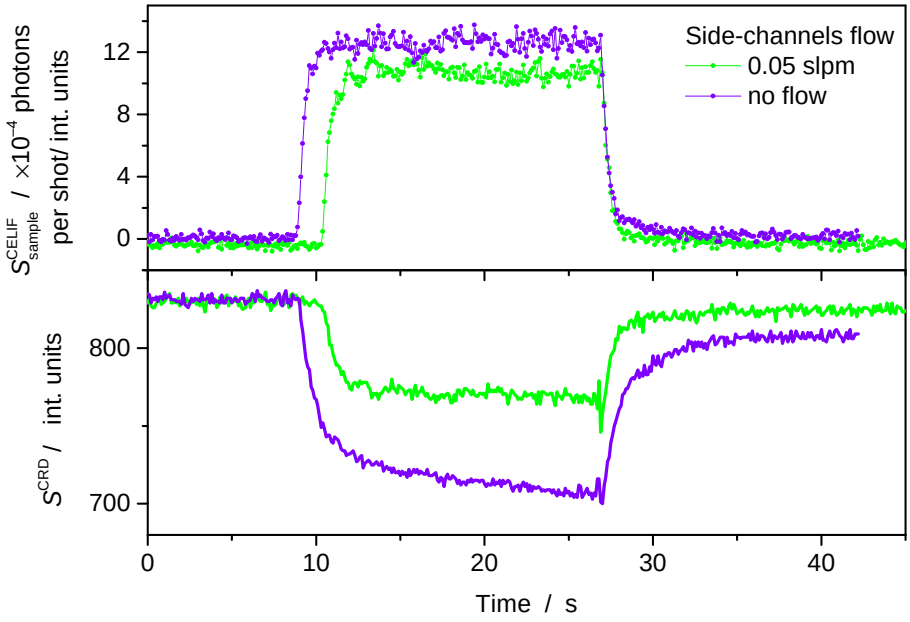

Figure 4.23: Real-time CELIF and CRD signals taken using flow-body-3, once with side channel flow of 0.05 slpm through each channel (green curve), and once with no side channel flows (purple curve). Each measurement was an average of 1500 laser shots and was recorded with a 100 ms time interval.

4.3.8 Performance of Flow-body-3

CELIF Response Time with Flow-body-3

Similar to previous flow-body designs, a CELIF response time test was made using the sampling method presented in figure 4.17. The measurement was made first with no side channel flows, and was compared with the similar measurement made with flow-body-2, as shown in figure 4.22. The rise and fall times of the CELIF measurement taken with flow-body-3 with no side channel flows were 0.8 ± 0.1 s and 1 ± 0.2 s respectively. This is faster than the CELIF measurement made by flow-body-2. Taking into account the pressure drop caused by the manual switching of the 3-way valve, which may cause a slower response of the CELIF measurement, this design of the flow-body is promising. However, a better sampling method must be considered, which is discussed in section 4.3.9.

The Effect of the Side Channel Flows

Two CELIF response time measurements were made with flow-body-3 using the same gas mixture. The first measurement was made with no side channel flows, and the second one was made with 0.05 slpm air flow through each channel. The two measurements are plotted together in figure 4.23. Despite the simulations showing that no mixing occurs between the air in the side channels and the sample, the experiment shows that the side channel flows dilute the acetone concentration in the sample. The slope in the CRD signal for the measurement without side channel flows, compared to the flat CRD signal in the measurement with side channel flows suggests that the side channel flows act as barriers between the flow regions and reduce the amount of the sample gas that diffuse into the side arms.

Time lapse acetone CELIF measurements were made with flow-body-3 at different side channel flow rates. A mixture of acetone in air was made and was flowed through the flow-body at a flow rate of 0.5 slpm for 15 minutes, while the LabView program was recording the CRD, LIF and CELIF signals every 1 minute, averaging 1500 laser shots for each measurement. This measurement was repeated flowing air through the side channels at flow rates of 0.025, 0.05 and 0.1 slpm through each channel.

The results are shown in figure 4.24. Similar to what happened with previous flow-bodies, when there was no side channel flows, the CRD signal quickly decayed as the gas extended into the side arms through the two laser holes in the flow-body. However, when flowing the sample along with flowing air through the side channels the rate of the decay decreased with increasing side channels flow rate. Side channel flow rate of 0.1 slpm through each channel was able to prevent the diffusion of the sample into the side arms, however, as shown in the acetone concentration plot, flowing air through the side channels with even a small flow rate caused dilution of the sample. Even with the improved design of the side flow channels, mixing between the sample and the side channel flows occurred, thus, the use of side channel flows should be avoided.

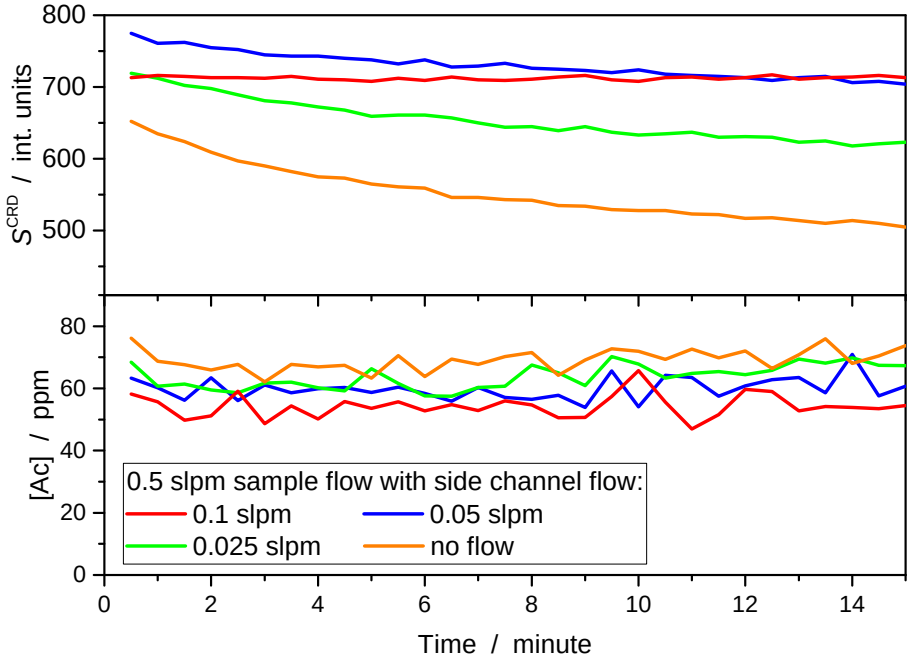

Figure 4.24: Time lapse acetone CELIF measurement made using flow-body-3 with a sample flow rate of 0.5 slpm, with different side channel flow rates. The measurements were recorded with a 1 minute time interval and each measurement was an average of 1500 laser shots.

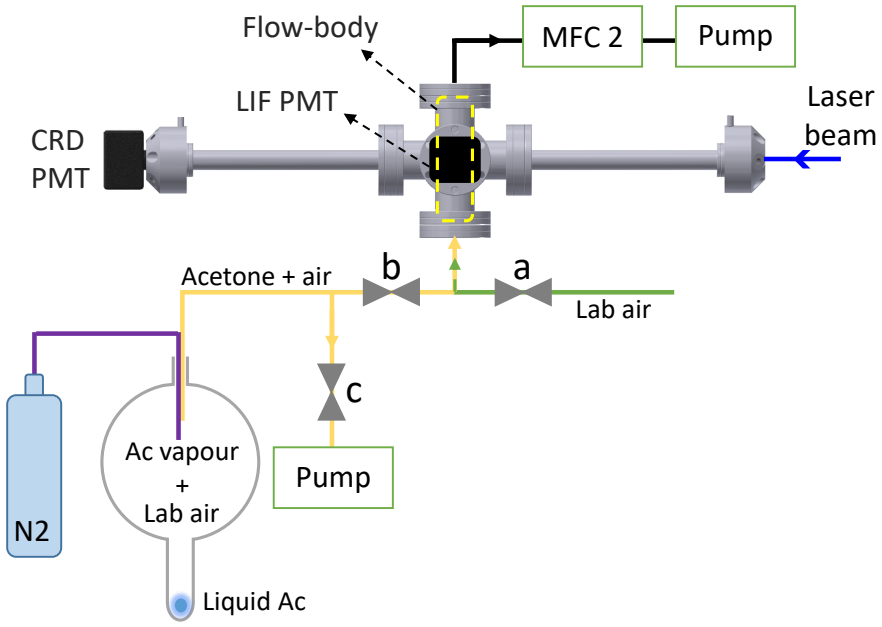

Figure 4.25: Schematic diagram of the acetone–air gas sampling method using a flow system and shut off valves instead of the 3-way valve. Valve a was normally open while valve b was open along with valve a only to allow some of the acetone–air mixture to flow through the flow-body.

4.3.9 CELIF Response Time

At this stage of the project, no trials were made on patients. The response time of the CELIF measurement could not be tested with breath acetone signals. Thus, a gas sampling method which does not involve using a 3-way valve and interrupting the pressure inside the cavity was implemented. Figure 4.25 shows the sampling method. Similar to the previous methods, a few drops of acetone were put in a 3 L glass bulb, which was open to the atmosphere. A nitrogen gas was supplied continuously into the glass to dilute the acetone–air mixture. A sampling tube was inserted into the glass bulb, and the other end of the tube was connected to a T-piece. One end of the T-piece was connected to the pump through a shut off valve, valve c, and the other end of the T-piece was connected to another shut off valve, valve b. Valve c was partially open to allow a continuous stream of sample gas with a flow rate of about 5 slpm, to prevent the acetone vapour from accumulating inside the tube. Valve b is connected through another T-piece to a third shut off

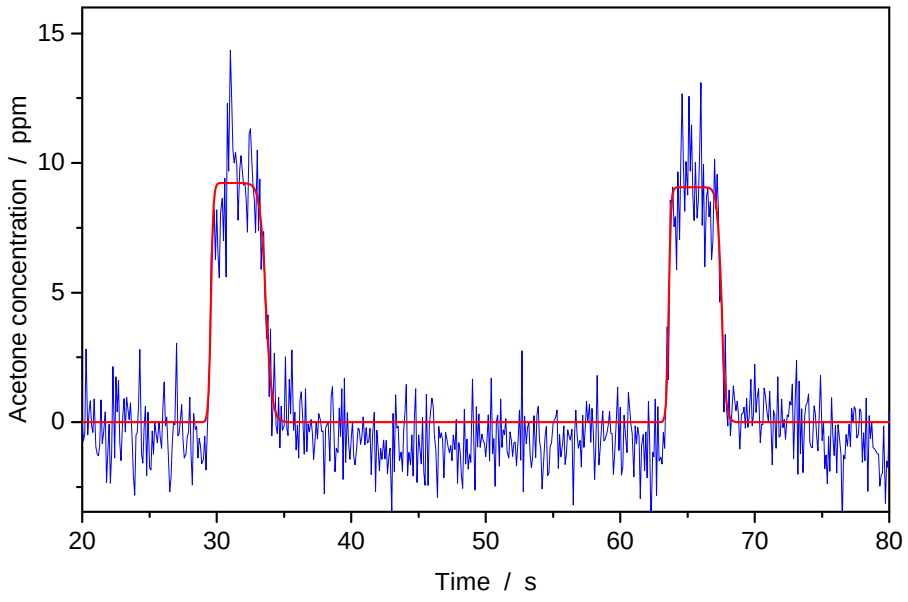

Figure 4.26: The blue curve is a real-time acetone concentration signal recorded using flow-body-3 with a sample flow rate of 0.5 slpm and without side channel flows. The red curve is a fit of the data using Eqn 4.3.1. Each CELIF measurement was an average of 1500 laser shots and was recorded every 100 ms.

valve, valve a, which was always open to lab air. The other end of the T-piece is connected through a short tube to the sample inlet of flow-body-3. The inlets of the side channels in the flow-body were blocked. While valve a was always open, a sample could be flowed through the flow-body by opening valve b. by doing this the pressure inside the cavity remained undisturbed.

The CELIF response time measurement was made by first allowing the lab air only to flow through the system, then valve b was open for a few seconds and then quickly closed to allow the sample to join the air flow into the system. This was repeated a second time, while the LabView program was recording the CRD, LIF and CELIF signals every 100 ms, averaging 1500 laser shots in each measurement.

The result is shown in figure 4.26. The blue line is the real time acetone concentration as measured by CELIF. The red line is a fit of the data of the form:

$$y = \frac{A_1}{(1+\exp(-\frac{t-t_{r1}}{\tau_{r1}})) \times (1+\exp(\frac{t-t_{f1}}{\tau_{f1}}))} + \frac{A_2}{(1+\exp(-\frac{t-t_{r2}}{\tau_{r2}})) \times (1+\exp(\frac{t-t_{f2}}{\tau_{f2}}))}, \tag{4.3.1}$$

where, for the first acetone peak, A_1 is the acetone concentration, t_{r1} is the centre

of the rising edge, τ_{r1} is the time constant of the rising edge, t_{f1} is the centre of the falling edge and τ_{f1} is the time constant of the falling edge. The rest of the constants are the same for the second acetone peak. From that the 10% rise time of the signal peak, t_{10}, is

$$\frac{1}{1+\exp(-\frac{t_{10}}{\tau_r})} = \frac{1}{10}\,,$$

$$\exp(-\frac{t_{10}}{\tau_r}) = 9\,,$$

$$t_{10} = -\,\tau_r \ln(9)\,.$$

And the 90% rise time of the signal peak, t_{90}, is

$$\frac{1}{1+\exp(-\frac{t_{90}}{\tau_r})} = \frac{9}{10}\,,$$

$$\exp(-\frac{t_{90}}{\tau_r}) = \frac{1}{9}\,,$$

$$t_{90} = \tau_r \ln(9)\,.$$

Thus, the 10–90 % rise time of the signal is

$$2\,\tau_r \ln(9)\,,$$

and the same follows for the 90–10 % fall time of the signal,

$$2\,\tau_f \ln(9)\,.$$

From the fit it was found that the 10–90% rise time of the CELIF measurement was 370 ± 15 ms, and the 90–10% fall time was 850 ± 21 ms, where the errors are from one standard deviation. The rise and fall time of the CELIF measurement are fast enough to follow a real breath pattern. While the two times should be equal, the longer fall time is likely to be caused by some acetone sticking into the tube fittings before the flow-body which takes some time to clear up.

4.3.10 Cavity Cleaning Between CELIF Measurements

To test how long it takes the cavity to return to CELIF background level after introducing a sample of high acetone concentration, a CELIF measurement was made by allowing lab air to flow into flow-body-3 without side channel flows, flowing

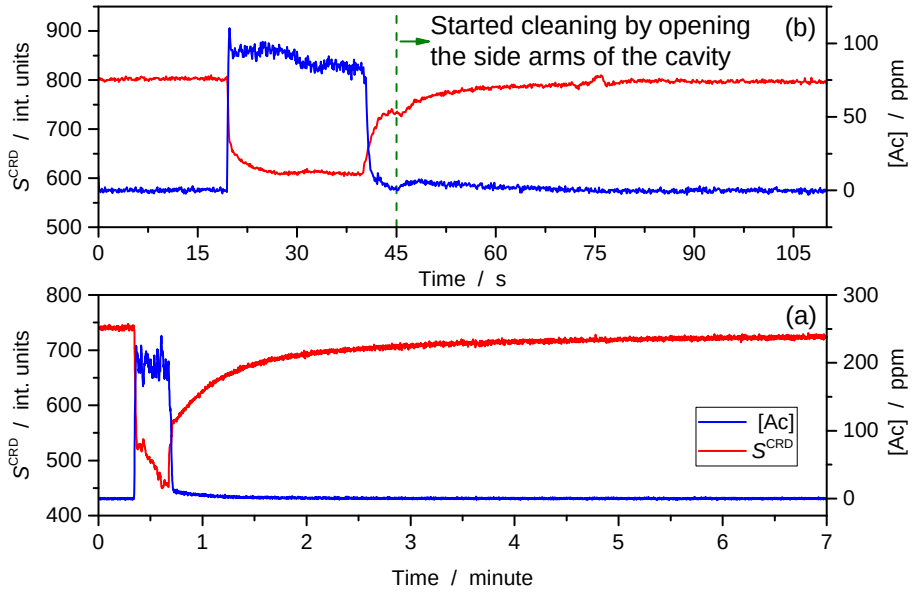

Figure 4.27: Real-time CRD measurements testing how long it takes the system to recover the background after flowing acetone–air sample, (a) without opening the side arms, and (b) with opening the side arms.

an acetone–air mixture for about 20 s, then turning the flow back to only lab air, as shown in figure 4.27 (a). The CRD signal shows that there was acetone build up in the side arms. The slow (several minutes) decay of the signals back to the baseline level after flowing a sample of acetone was probably caused by the fact that a high acetone concentration has been flowing through the flow-body for about 20 s. This decay is not seen in figure 4.26 where the "breaths" are much shorter (< 5 s) and more representative of a real breath.

Next, the same measurement was repeated as in figure 4.27 (b), but this time the air inlets in the side arms of the cavity, near the cavity mirrors, were open after the acetone CELIF measurement was made to allow air to flow through the system from 3 inlets: the flow-body inlet and from both side arms of the cavity and exit the system through the flow-body outlet, flushing any acetone residuals that were stuck on the cavity walls. By doing this, the signals decayed back to the background level within only 30 s, presenting a quick method to clean the cavity and removing any acetone from the system after breath measurements.

While monitoring real patients breath, we could tolerate some acetone build up in the side arms as long as it does not affect the CELIF measurement. However,

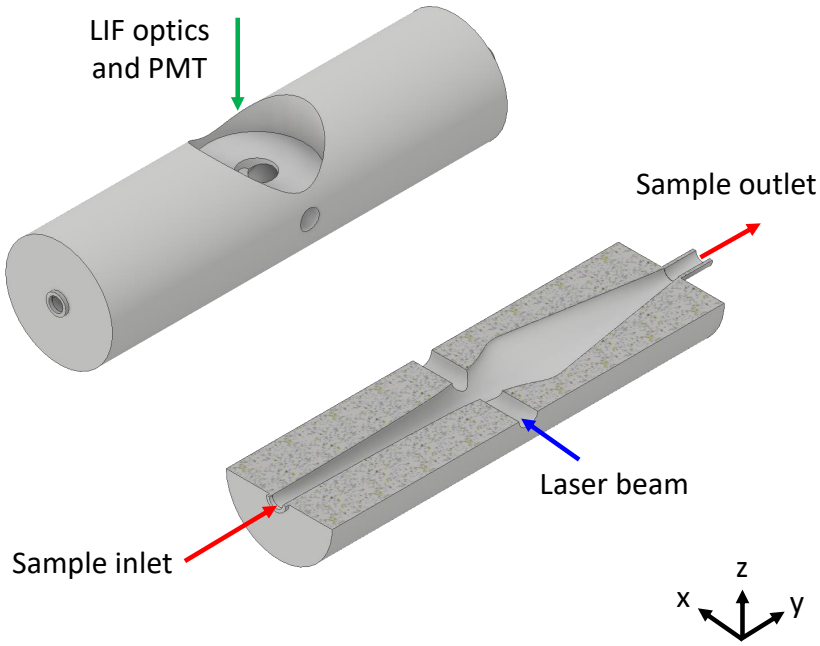

Figure 4.28: CAD drawing showing a full view and a half section view of the final flow-body design.

eventually the build up will become intolerable, and the cavity will need to be flushed by the method described above. The time after which the cavity will need to be cleaned depends on the amount of acetone concentration being monitored. The proposed cleaning method is quick (about 30 s), does not require any change in the setup and could be automated in the final version of the device. Therefore, it is recommended to clean the cavity at least every 1 minute while monitoring a real patient's breath with acetone concentration of more than 30 ppm, and every 2 minutes if the acetone concentration is less than that. It is also required to clean the cavity between the measurements of different patients to prevent cross contamination.

4.3.11 Final Flow-body

As the required response time of the CELIF measurements was achieved by the design of flow-body-3 without side channel flows, and the diffusion of the sample into the cavity was overcome by cleaning the cavity by flowing air from the three gas inlets and out from the flow-body outlet, the final flow-body was made identical

to flow-body-3 but taking out the side channels. The design of the final flow-body is shown in figure 4.28. The 3D printed flow-body-3 extended out from the 6-way cross and was printed with a flange as one piece. The final flow-body was made to be fully fitted inside the 6-way cross, thus, the total length of the flow-body was shorter than flow-body-3. Because of that, the laser holes (6 mm diameter) were no longer at the widest flow width and were shifted to the left. The diameter of the LIF optics hole was made only 10 mm to fit the width of the sample. The total length of the flow-body and the outer diameter of the flow-body were not changed from the first and second designs and were 125 mm and 33.8 mm respectively. The sample inlet and outlet were 1/4 inch to fit with the other tubing system of the experiment. The final flow-body was machined from aluminum, as the PLA 3D printing material caused an increase of the background LIF signal. The flow-body was painted with an optical absorber coating (Alion MH2200) which was proved to reduce the amount of the LIF background level by absorbing the scattered light inside the system.

4.4 Validation of the CELIF Instrument

In order to investigate the accuracy of the CELIF instrument and to fulfill the requirement for the CELIF instrument to be medically approved, the concentrations of acetone measured by the CELIF instrument must be compared with an analytical technique. A selected ion flow tube mass spectrometer (SIFT-MS) instrument (Voice200Ultra - Syft Technologies) was provided by Anatune to the department of chemistry at Durham University and was used to validate the CELIF instrument.

SIFT-MS is a new analytical technique for the simultaneous, real-time quantification of several trace compounds in air or breath samples [24–26]. A mixture of positive ions (H_3O^+, NO^+, O_2^+) is created in a microwave discharge, and a current of a chosen ionic species is obtained using a quadrupole mass filter. The selected ions are injected into fast flowing carrier gas, usually helium at a pressure of 1 Torr, via a Venturi orifice (1 mm diameter) where they travel along the reaction flow tube by convection. The air/breath sample to be analysed is introduced at a known flow rate into the carrier gas and only a small fraction of it enters the flow tube via a heated,

calibrated capillary. The compounds of the trace gas react with the reagent ions for an accurately defined time in the carrier gas resulting in characteristic product ions which are detected and counted by a down-stream mass spectrometer.

4.4.1 SIFT-MS Analysis

The concentrations of individual compounds in the sample gas is calculated using the count rates of the reagent and product ions, and the reaction rate coefficients. The SIFT-MS instrument can run in either a Full Scan mode to scan across a chosen range of ion mass-to-charge, m/z, ratio to produce a conventional mass spectrum to identify the reagent and product ions and to determine their count rates. The rate coefficients and the product ions of the particular reagent ion/trace gas compound reactions have been calculated by this mode for hundreds volatile compounds, from which a kinetics library has been constructed and used in the analysis computer. After appropriate corrections for mass discrimination and differential diffusion, the online computer immediately calculates the concentrations of the trace gas compounds present in the gas sample.

The other mode of SIFT-MS analysis is the Multiple Ion Monitoring mode, which after recognizing the m/z values of interest with the Full Scan mode, a rapid switch procedure for each of the ions is used to accumulate each ion's signal count rates. The manufacturer claims that this mode is very rapid and allows real-time following of the temporal changes in the concentrations of trace compounds and allows accurate quantification to the parts per billion (ppb) level.

4.4.2 CELIF Validation Measurements

A SIFT-MS instrument (Voice200Ultra - Syft Technologies) was provided by Anatune and was used for the CELIF validation measurements. It was brought in the lab next to the CELIF device. The gas sampling setup was modified as seen in figure 4.29. A T-piece was added after the gas cylinder outlet to split the gas sample between the CELIF and the SIFT-MS instruments to allow simultaneous measurements by both instruments. The gas flow path in the CELIF device was made such that it can be

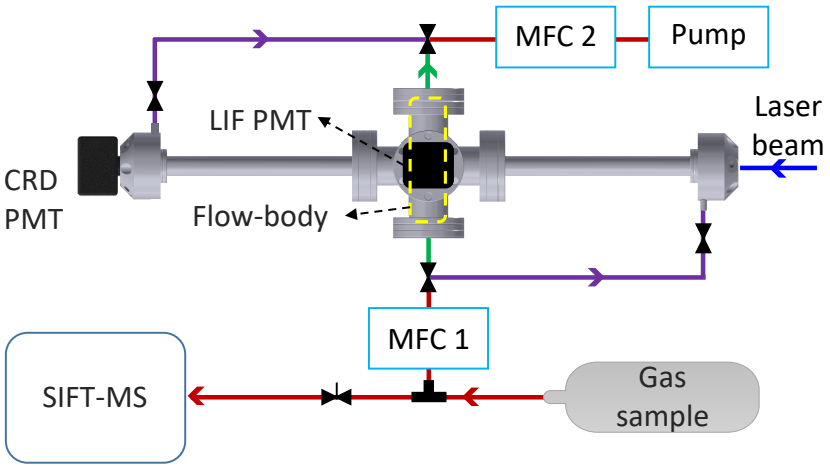

Figure 4.29: Schematic diagram of the experiment setup for the CELIF validation by the SIFT-MS. Gas samples are split by a T-piece between the CELIF and the SIFT-MS instruments. Sample flow to the SIFT-MS is restricted by a needle valve. The purples lines indicate the gas flow direction for the CRD measurements, and the green lines indicate the gas flow direction for the CELIF measurements through the flow-body.

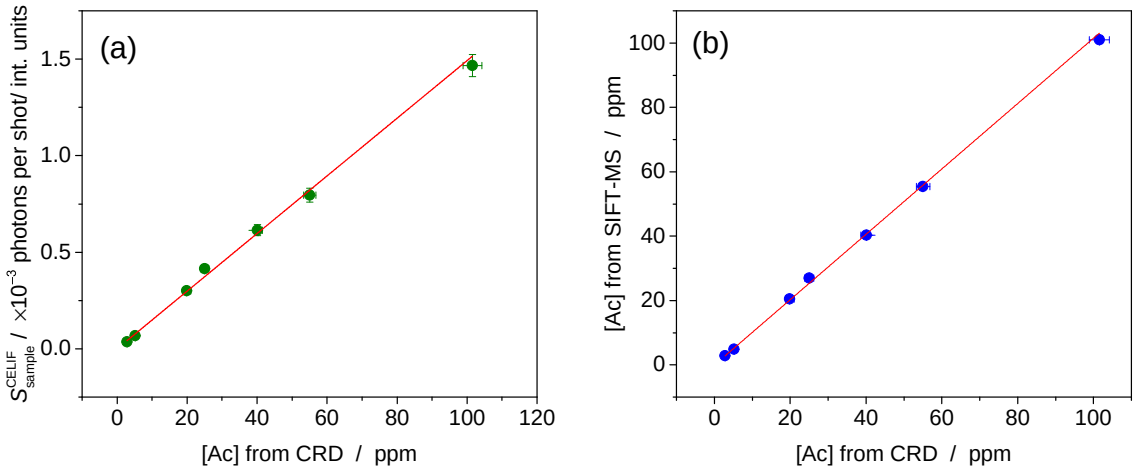

Figure 4.30: (a) Calibration of the CELIF instrument using standard acetone–nitrogen gas mixtures. Each measurement was an average of 1500 shots and was taken while flowing the sample longitudinally through the cavity axis. (b) Comparison between acetone concentrations measured simultaneously by CRD and by the SIFT-MS. The slope 1.02 ± 0.02 in the fitting equation proves the agreement between the two methods. The error bars in the CRD measurements are from one standard error, and in the SIFT-MS measurements are from one standard deviation and are smaller than the symbols.

easily switched between the longitudinal CRD measurements along the cavity axis and the transverse CELIF measurements through the flow-body. A needle valve was used to restrict the flow to the SIFT-MS instrument.

The CELIF device was first calibrated by using standard acetone–nitrogen gas mixtures in the range of 1–100 ppm (SIP Analytical, SIPCYL 110 LTR non-refillable can filled certified grade acetone in nitrogen). Each gas mixture was measured simultaneously by the two instruments. CRD and LIF measurements were recorded for CELIF calibration by flowing the gas longitudinally through the cavity axis and simultaneously the acetone concentration in the sample was measured by the SIFT-MS. Both the CELIF cavity and the SIFT-MS were flushed between the measurements. Each CELIF measurement was an average of 1500 laser shots and was recorded using a 0.5 slpm sample gas flow. Each SIFT-MS measurement was an average of acetone concentrations measured over 20 s of gas flow, with a measurement interval of 140 ms.

Table 4.1: A summary of the SIFT-MS instrument (Voice200Ultra - Syft Technologies) method used for the validation of the CELIF device.

Carrier gas type	Helium
Reagent ion	NO^+ (30 amu)
Product ion	$NO^+CH_3COCH_3$ (88 amu)
Carrier Flow (tls)	5.0057
Sample Flow (tls)	0.3
Tube Temp (C)	123.75
Tube Pressure (Torr)	0.6348
Reaction Time (ms)	8.203

Next, to validate the CELIF measurements with the SIFT-MS measurements, the procedure above was repeated using the same standard gas bottles but flowing the gas samples transversely through the flow-body and using the previous CELIF calibration to calculate the acetone concentration. More validation measurements were also made using a home-made acetone–nitrogen mixture and a series of dilutions where each concentration was measured by CELIF and the SIFT-MS simultaneously. The SIFT-MS instrument was not optimised to measure acetone concentrations above about 100 ppm, thus the validation measurements were restricted to acetone concentrations between 1 ppm (CELIF limit of detection)–100 ppm.

The used SIFT-MS method is summarised in table 4.1. Surprisingly, a SIFT-MS instrument dependent correction factor was needed to correct for the acetone reaction rates which was important for accurate quantification of our validation measurements. In the (Anatune) lab, a gas sample that should give 6 ppm acetone was generated and measured with SIFT-MS using all the possible reagent ions, and from the data generated the reaction rates were amended. This yielded that a correction factor of 1.519 must be multiplied by the acquired SIFT-MS validation data.

The CELIF calibration measurements and the comparison between CRD and SIFT-MS measurements of acetone concentration are presented in figure 4.30 (a) and (b) respectively. The slope 1.02 ± 0.02 in the fitting equation suggests that the obtained acetone concentrations using both methods are consistent. The CELIF

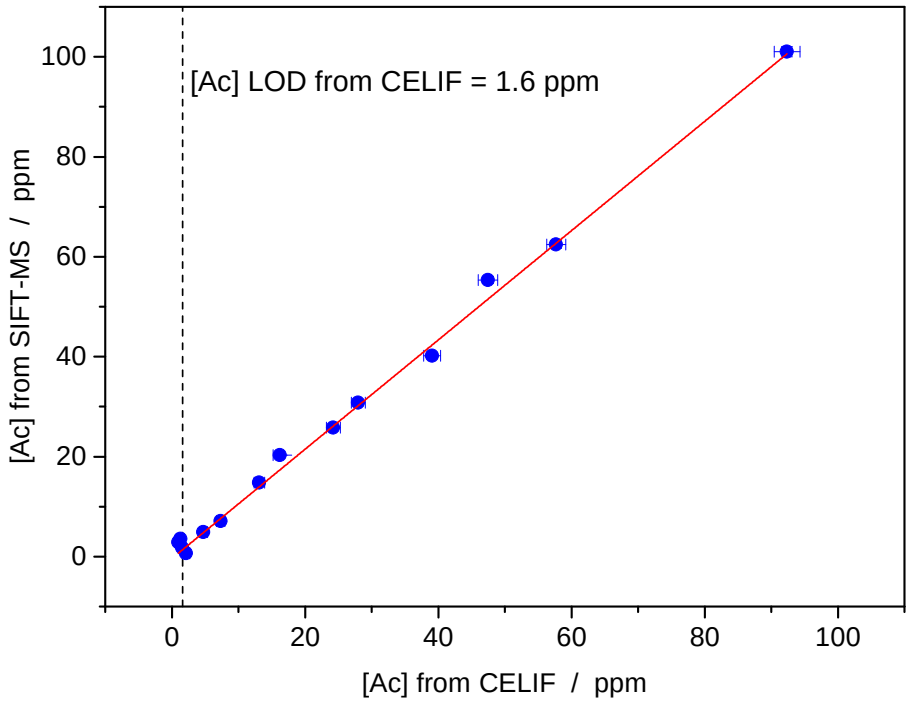

Figure 4.31: Validation of the acetone concentration measurements by the CELIF instrument with the SIFT-MS instrument. The slope 1.1 ± 0.1 in the fitting equation proves the agreement between the two methods. The error bars in the CELIF measurements are from one standard error, and in the SIFT-MS measurements are from one standard deviation and are smaller than the symbols.

validation measurements using both the standard gas mixture and the home-made mixtures are shown in figure 4.31. The acetone concentration simultaneous measurements with the CELIF device and the SIFT-MS instrument agree with each other with a linear fitting slope of 1.1 ± 0.1. This SIFT-MS validation test proves that the acetone concentration measurements by the CELIF device are reliable and fast and can be used for measurements of breath samples.

The acetone CELIF measurement procedure, the flow-body design and the response time of the CELIF measurements were optimised. We achieved an acetone concentration dynamic range between 1.6–2000 ppm, covering the range of breath acetone concentration a DKA patient might have. The CELIF device was validated with the SIFT-MS. In the next chapter, breath acetone measurements made with our home-built buffered end-tidal breath sampler will be presented.

Chapter 5

Breath Acetone Measurements

This chapter describes the breath acetone measurements made with the CELIF instrument. It was necessary to consider what other molecules exist in the exhaled breath and whether they affect the CELIF measurements or not. The main molecules detected in the exhaled breath which exist in high abundance are oxygen (16%), water vapour (6%) and carbon dioxide (5%) [28, 65].

Of more than 1000 major volatile organic compounds (VOCs), acetone and isoprene are two of the highest abundance present in human breath gas. Sahay *et al.* conducted ring-down absorption measurements of varying concentrations of acetone, isoprene and 5% CO_2 gas at 266 nm, and compared the results with actual human breath gas [66]. The results implied that, at 266 nm, between all the VOCs acetone in breath causes most of the reduction in the ring-down time. The study showed that isoprene absorbs at 266 nm however, the absorption cross section of acetone at 266 nm is approximately 32 times larger than the absorption cross section of isoprene at 266 nm. Furthermore, CO_2 has minimal absorption at 266 nm, and most of other VOCs do not have a strong absorption at 266 nm. In another study, Wang *et al.* concluded that acetone is the largest contributor of absorption at 266 nm, and all the contributions from other VOCs or atmospheric compounds in a normal human breath are negligible [28].

While the absorption of these molecules at 266 nm, and hence their fluorescence, is negligible, their effect on the acetone CELIF measurements, due to Rayleigh scattering or acetone fluorescence quenching should be tested.

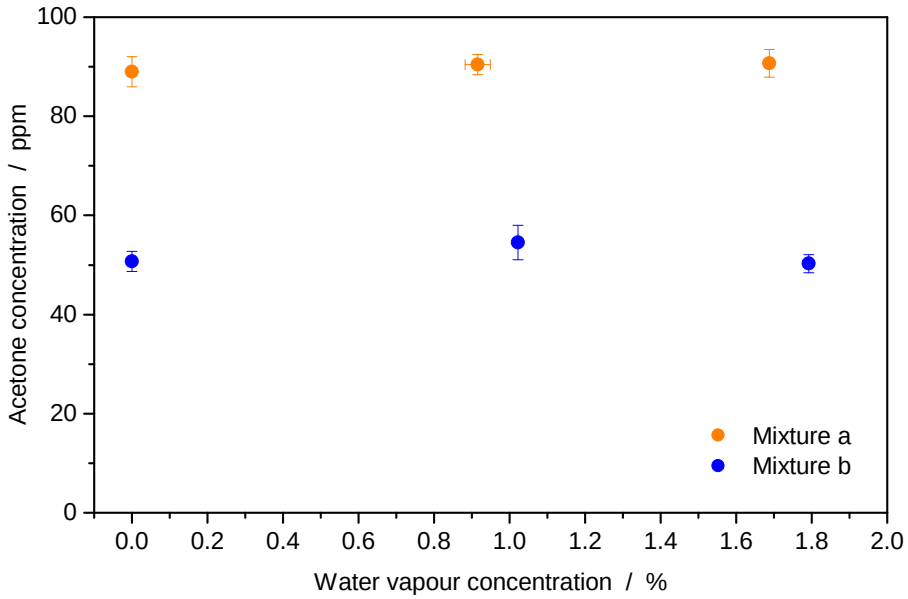

Figure 5.1: The effect of water vapour on acetone concentration as measured by CELIF. The mixtures were made by adding water vapour to standard acetone–nitrogen gas mixtures. Each data point is an average of 6 and 3 data points for mixtures a and b respectively. The error bars are one standard deviation.

5.1 Effect of Oxygen

While oxygen is a possible quencher of acetone fluorescence, due to the short fluorescence lifetime of acetone the effect of oxygen quenching on acetone is negligible [67]. The concentration of oxygen in exhaled breath (16%) is less than what is in the air (21%) [28]. Our measurements showed that using air as a gas bath to mix with acetone instead of nitrogen does not affect the fluorescence of acetone at atmospheric pressure, which is also confirmed by the work done by Thurber *et al.* [68,69]. Thus, the existence of oxygen in the exhaled breath is not considered an issue when measuring acetone concentration by CELIF.

5.2 Effect of Water Vapour

Standard acetone–nitrogen gas mixtures (SIP Analytical, SIPCYL 110 LTR non-refillable can filled certified grade acetone in nitrogen) were used for this test to ensure reproducibility of the mixing ratios. A small liquid water reservoir was added

to the gas mixing setup. The mixtures were made by first pumping down a 0.5 L mixing cylinder, then expanding water vapour (23 mbar) into it followed by the standard acetone–nitrogen mixture up to about 2.3 bar. This gives about 1% of water vapor in the gas mixture. The mixture was allowed to mix for about 15 minutes with the help of heating the side arms of the mixing cylinder to create a convection current. The CELIF measurement was then taken by transversely flowing the gas sample into the flow-body in the cavity at a flow rate of 0.5 slpm, and averaging 1500 laser shots. Because the water vapour pressure at room temperature is small (23 mbar), making higher concentrations of water vapour in the 0.5 L mixing cylinder was not possible; as a minimum total pressure of 2 bar in the mixing cylinder was needed to make a single CELIF measurement. Thus, the 0.5 L mixing cylinder was replaced with a 3 L glass bulb. The required minimum total pressure of the gas was reduced to 1.25 bar with the glass bulb. The extra gas volume allowed a higher water vapour concentration, about 1.8 %, in the acetone–nitrogen mixtures, and a longer flow time enough for CELIF measurements to be taken. Making higher than 1.8 % water vapour in a mixture of acetone–nitrogen was not possible in our setup.

The CELIF measurements were made using two different standard gas mixtures. Each measurement was repeated 5 times with gas mixture (a), and only 3 times with gas mixture (b). Figure 5.1 shows that the presence of water vapour in the acetone–nitrogen mixtures does not change the measured CELIF signal and hence the acetone concentration. Thus water does not have to be removed from the breath sample.

5.3 Effect of CO_2

CO_2 might increase Rayleigh scattering which will have an impact on both the CRD and the LIF measurements, but not on the CELIF signal. However, because a LIF filter is used, which blocks Rayleigh scattering, if CO_2 causes scattering then only the CRD measurements will suffer. This will change the air–CO_2 CELIF signal compared to the background, air, CELIF signal.

To investigate whether CO_2 affects the background CELIF, a CO_2 sensor (GSS,

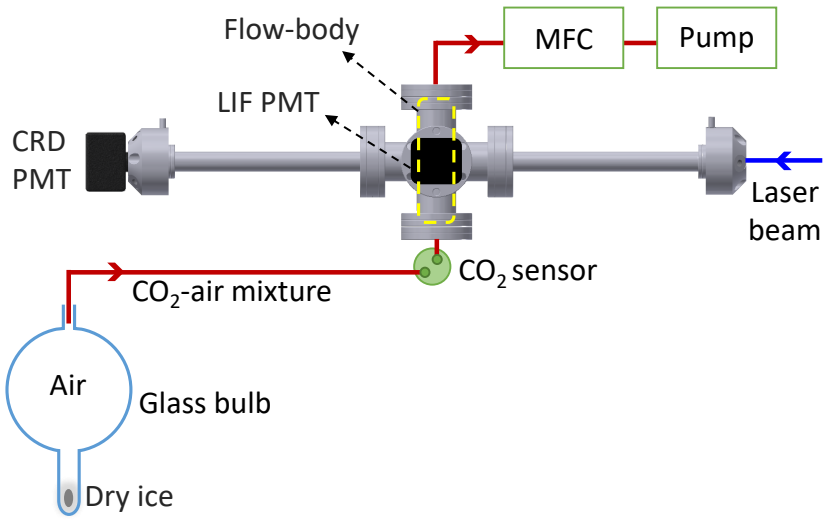

Figure 5.2: Schematic of the CELIF experiment setup for the CO_2 test. The CO_2 concentration is measured before the gas enters the flow-body.

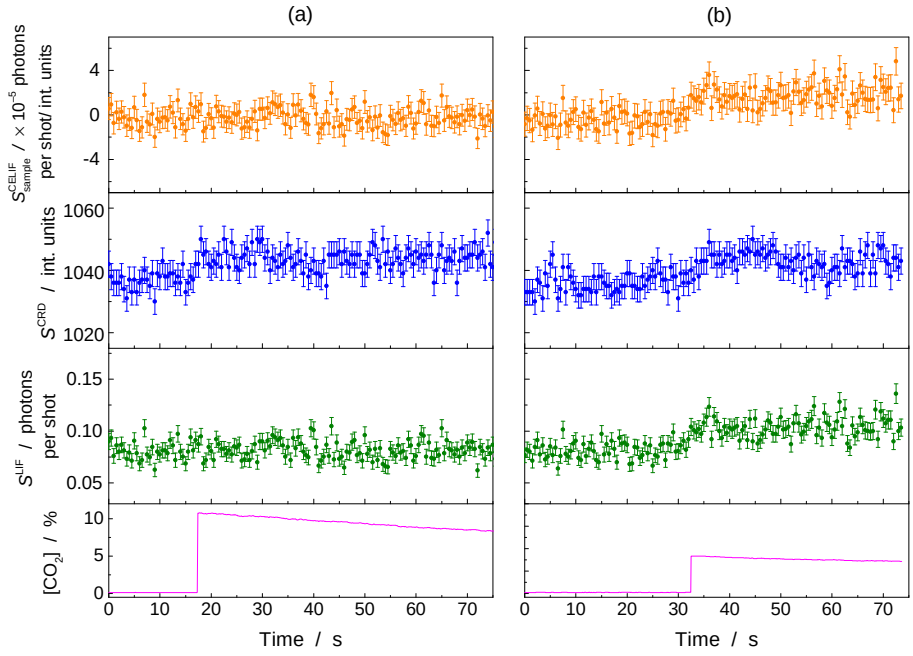

Figure 5.3: The effect of CO_2 on the background CELIF measurement, using a LIF filter (a), and without LIF filter (b). Each measurement is an average of 1500 laser shots, with a measurement interval of 0.5 s. The statistical error bars are from 1 standard error. The CO_2 measurement is time shifted due to the CO_2 sensor sampling position being before the CELIF measurements.

SprintIR) was added to the setup at the inlet of the flow-body, as shown in figure 5.2, to measure the concentration of the CO_2 in a sample while measuring the CELIF signal. A small piece of dry ice was put in a glass bulb, which was open to the atmosphere. The dry ice was left to evaporate to create air–CO_2 mixture at room temperature. A sampling tube was attached to the flow-body inlet, before the CO_2 sensor. The LabView program was set to record CELIF signals for 80 s, with each measurement being an average of 1500 shots. During the first couple of seconds only lab air was allowed to flow into the flow-body using the sampling tube. Then, the sampling tube was brought next to the glass bulb inlet to sample the air–CO_2 mixture. The measurement was done by flowing the sample transversely through the flow-body at flow rate of 0.5 slpm. The inlet of the flow-body was open to the atmosphere i.e. without the inlet mass flow controller (MFC). The MFC is gas sensitive, which means it changes the flow rate based on the gas composition flowing through it. Interchanging the flowing gases without changing the gas selection in the MFC introduces a pressure difference and disturbs the measurement. Thus, when flowing lab air the exit MFC was set to "air", but when flowing air–CO_2 the MFC was set to "air containing 7% CO_2". The results of these measurement are presented in figure 5.3 (a) with LIF filter, and (b) with the LIF filter removed. Removing the LIF filter increases the detected fluorescence signal coming from Rayleigh scattering. Which causes the CELIF signal to increase compared to the background, air, CELIF signal. The increase in CRD signal is attributed to the pressure difference that the MFC causes before switching the gas type. With the LIF filter in place, there is no detected effect of the Rayleigh scattering of CO_2 on the background LIF or CELIF signal.

Non-polar molecules such as CO_2 are unlikely to quench acetone fluorescence. However, to check whether CO_2 affects the acetone CELIF signal, a mixture of acetone–air and CO_2 was created by adding a small piece of dry ice in a glass bulb containing acetone–air mixture. First, lab air was sampled for a couple of seconds, then the sampling tube was inserted gradually in the glass bulb to gradually increase the CO_2 concentration. The results in figure 5.4 show that, even though the CO_2 concentration was increased to about 20 %, the acetone concentration was

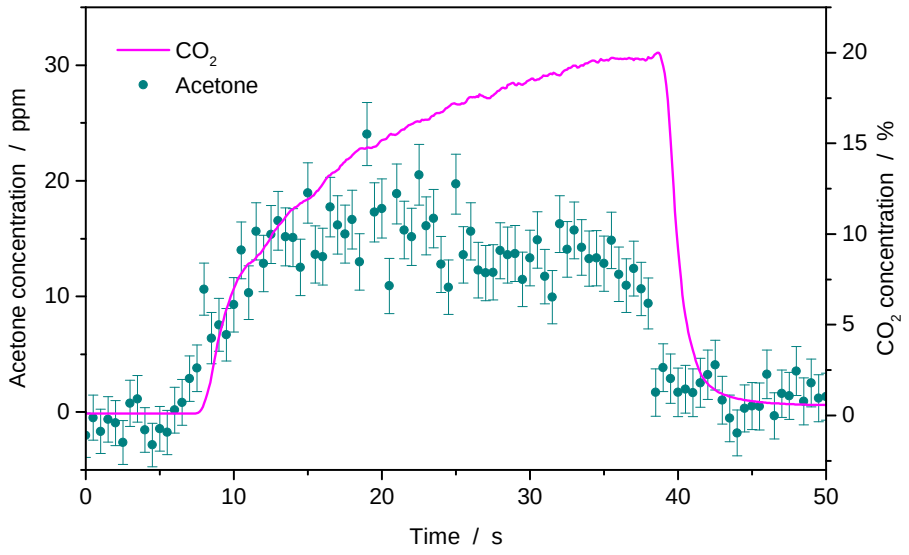

Figure 5.4: The effect of CO_2 on the acetone CELIF measurement. Each measurement is an average of 1500 laser shot, with a measurement interval of 0.5 s. The statistical error bars are from 1 standard error. The CO_2 measurement is time shifted due to the CO_2 sensor sampling position being after the CELIF measurements.

not affected by the existence of CO_2. The acetone–air mixture began running out after 25 s of flow causing a small reduction in the measured acetone concentration.

Our measurements confirmed that the existence of CO_2 in the exhaled breath does not affect the acetone CELIF measurements due to Rayleigh scattering or acetone fluorescence quenching, and thus CO_2 does not have to be filtered out during acetone CELIF measurements.

5.4 Buffered End-Tidal Breath Sampler

A cost effective, online, buffered end-tidal breath sampler was developed to measure breath acetone concentration with the CELIF instrument. The design of the sampler was based on the breath samplers by both Herbig *et al.* [15] and Righettoni *et al.* [70]. The sampler detailed here was built by another group member [71].

In buffered end-tidal breath sampling the subject is required to exhale at a controlled flow into a sampling buffer tube, then withdraw to allow normal breathing. The typical flow rate of an exhalation is much higher than the continuous sampling

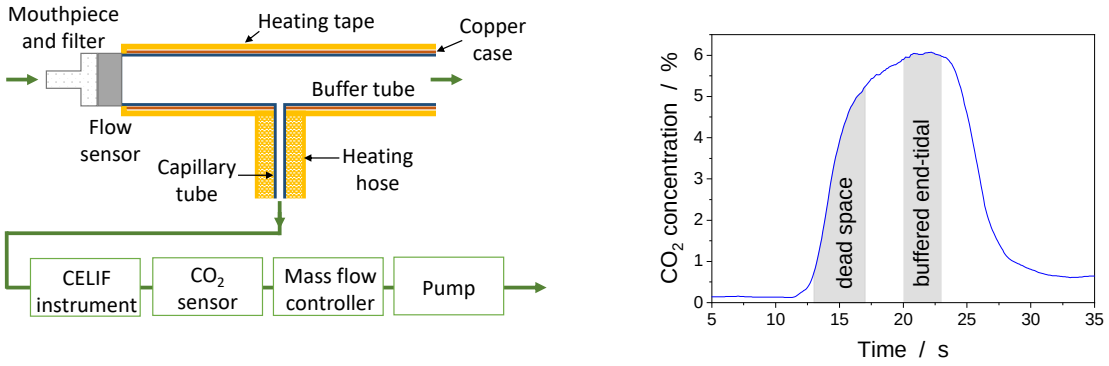

(a) (b)

Figure 5.5: (a) Schematic of the buffered end-tidal online breath sampler. The end-tidal fraction is buffered in the heated buffer tube. The CELIF instrument draws the sample gas through from the middle of the buffer tube. Exhalation is monitored by the flow and CO_2 sensors. (b) Typical exhalation profile for buffered end-tidal sampling measured with the CO_2 sensor.

flow into the CELIF instrument. The initial fraction of the breath is quickly expelled through the other end of the buffer tube, and the end-tidal fraction remains and buffered through a smaller sampling tube into the flow-body in the CELIF instrument. The buffered end-tidal sampling increases the sampling time to several seconds compared to normal online breathing, and removes the need for sub-second instrument response time; as at the time we made the breath measurements the flow-body design has not been optimised yet, and we didn't know if real-time measurement was possible.

5.4.1 Design

Referring to figure 5.5 (a), the sampling buffer tube was constructed from a 30 cm long PTFE tube of 19 mm inner diameter. In the middle of the buffer tube a 1.5 m long, 4 mm inner-diameter PTFE tube housed in a heating hose continuously draws gas from the middle of the buffer tube. The heating hose (Eltherm Heated Sample Lines) provided consistent temperature in the range 20–100 °C. The buffer tube was evenly heated by placing it in a copper casing which was wrapped with a heating tape. Heating the sampler eliminated problems related to condensation of

breath gas, and therefore acetone onto the walls of the sampler. A typical sampler temperature used in our measurements was 50 °C.

As seen in figure 5.5 (b), a CO_2 sensor (SprintIR) was added to the setup which allowed the end-tidal fraction of the breath to be measured without the need for acetone being present; this was important as the sampler was intended to be used for the first breath measurement with the CELIF instrument, so measuring another component of the breath gas was essential. The sensor was placed at the outlet of the flow-body so that the acetone and the CO_2 measurements could be taken at similar times.

A flow sensor (Sensiron SFM3000) was added to the inlet of the buffer tube, and was attached to a box with an array of LED lights. This allowed a set target exhalation flow rate to be maintained by the subject which enhanced reproducibility of exhalation patterns. Typical exhalation flow rates were set to 10 L m^{-1}, much higher than the 0.5 slpm continuous flow of the CELIF instrument.

A disposable mouthpiece with bacterial filter (Intersurgical, Clear-Guard) was attached to the flow sensor to act as an interface between the test subject and the breath sampler. A fresh mouthpiece and filter was used for each test and disposed of after every subject.

5.4.2 Testing the Sampler with Acetone Samples

It was important to test whether the breath sampler alters the acetone concentration in a gas sample before doing any breath measurement. A standard acetone–nitrogen gas mixture was used for this test to ensure reproducibility of the acetone concentration. The concentration of acetone in the gas sample was measured first by CRD using longitudinal flow, then by CELIF using transverse flow of 1 bar of the gas at 0.5 slpm, and recording an average of 1500 shots. Both measurements were taken at room temperature and repeated three times. The CRD measurement gave $[\mathrm{Ac}] = 36 \pm 1\,\mathrm{ppm}$, and the CELIF measurement gave $[\mathrm{Ac}] = 37 \pm 4\,\mathrm{ppm}$, where the error is one standard deviation. Next, the standard gas was sampled using the breath sampler by attaching the standard gas bottle to the mouthpiece in the breath sampler, allowing the gas to flow through the sampling tube and then transversely

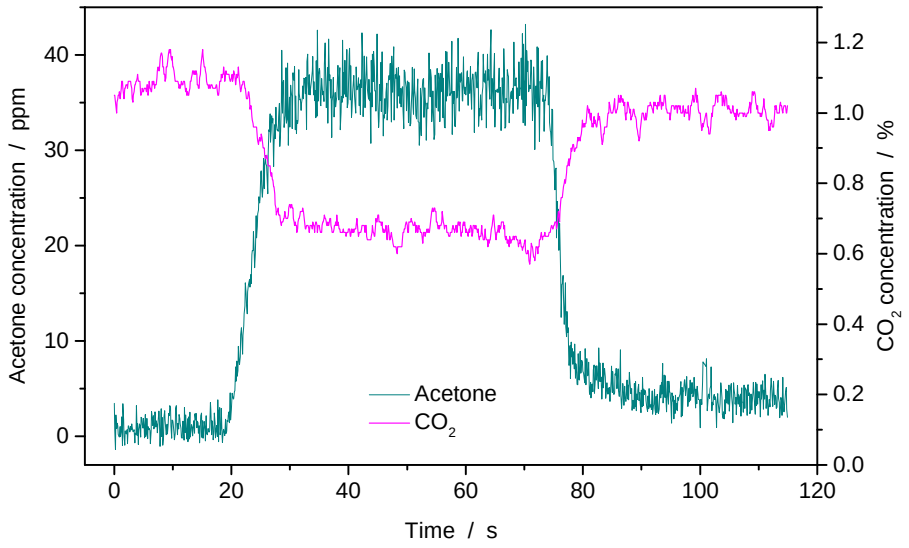

Figure 5.6: Real-time CELIF measurement of a standard acetone–nitrogen gas sample. Each measurement is an average of 1500 laser shots, with a measurement interval of 100 ms. The measurement was taken using 1 bar of the gas mixture at 0.5 slpm transverse flow.

through the flow-body at 0.5 slpm. The sampler was kept at room temperature, as it was the temperature of the standard gas. Then, a real-time CELIF measurements of the gas sample were recorded, as seen in figure 5.6. An average value was taken for all the acetone concentration measurements between 30 to 70 s giving a concentration of $[\mathrm{Ac}] = 36 \pm 2\,\mathrm{ppm}$. All three measurements were in agreement insuring that the breath sampler does not interfere with the acetone concentration.

5.4.3 Breath Measurements

Breathing Pattern

A comparison was made between normal online breathing into the sampler and end-tidal breathing. A healthy test subject was asked to breathe normally through their mouth into the breath sampler. After resting for a couple of minutes, the same subject provided a single end-tidal exhalation through the sampler at a controlled flow rate of 10 L m^{-1}, then withdrew and breathed normally, then provided a second single end-tidal exhalation. The two measurements were compared using the subject's CO_2 concentration as no detectable acetone was present in their breath. Figure 5.7

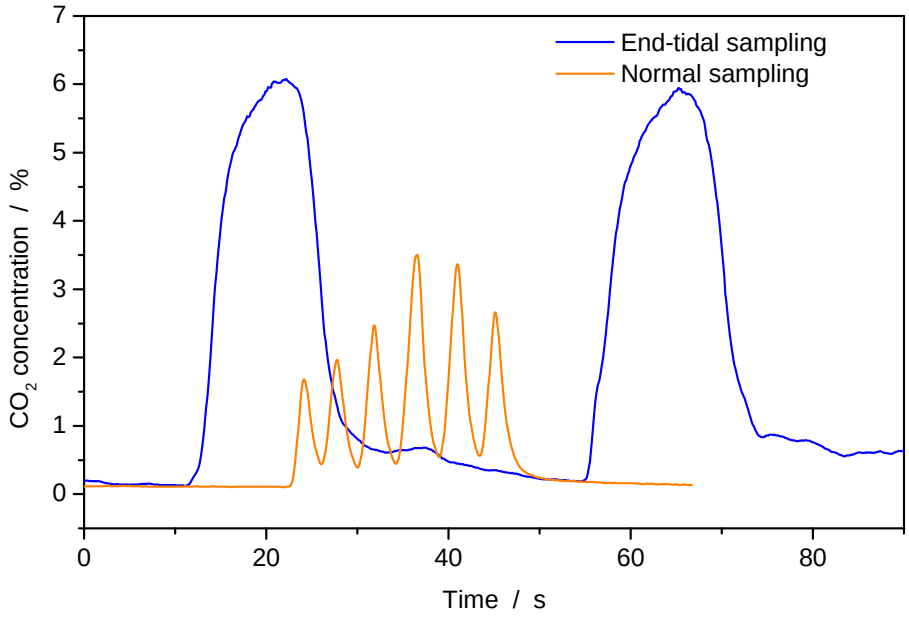

Figure 5.7: CO_2 signal measured by end-tidal breath sampling (blue curve) compared to normal mouth breathing through the sampler (orange curve). End-tidal sampling extends the time available for measurements for a couple of seconds. Normal breathing through the sampler underestimate the end-tidal CO_2 concentration. The measurements were taken at sampler temperature of 50 °C, breathing flow rate of 10 L m^{-1} and sampling flow of 0.5 slpm.

shows the difference between the two methods. In the normal online sampling the subject inhaled again through the sampling tube before the full signal maximum was reached resulting in an underestimation of the end-tidal concentration. Since in buffered end-tidal online sampling the end-tidal fraction remains in the buffer tube for a much longer period, the full signal can be reached and the measured concentrations were therefore not affected. This meant that the breath sampler that we built was only suitable for end-tidal breathing, and therefore, another breath sampler for real time breath-by-breath resolution is required for the next prototype of the CELIF instrument.

Breath Acetone Measurement

Typical breath acetone concentration in healthy humans is below the current CELIF limit of detection. Thus, a healthy test subject fasted for 18 hours to elevate the breath acetone level to above the CELIF limit of detection. The next morning, the subject was asked to provide end-tidal single exhalation at a controlled flow of 10 L m^{-1}. The subject withdrew and breathed normally away from the sampler, then provided a second end-tidal single exhalation at the same flow rate. The CRD, LIF, CO_2 and the acetone concentration signals from the subject's breath are shown in figure 5.8. The averaged end-tidal breath acetone concentration was 2 ± 1 ppm. The CRD signal showed a spike in response to replacing the lab air with breath sample; this was due to a sudden change in the flow-body inlet pressure caused by the mass flow controller which changes the set value of the flow rate in response to a quick change in the flowing gas compositions. Furthermore, as these measurements were made with a flow-body without side channel flows, the breath sample CRD signal was not constant, and as a result of the breath gas leaving the flow-body into the cavity side arms the sample length increased and reduced the CRD signal with time. However, this reduction does not change the CELIF signal and hence does not affect the measured acetone concentration as discussed in chapter 4.

We have shown that breath acetone concentration could be measured using CELIF without the need to remove other breath gas components from the sample. The buffered-end tidal breath sampler was useful for sampling breath of fasted

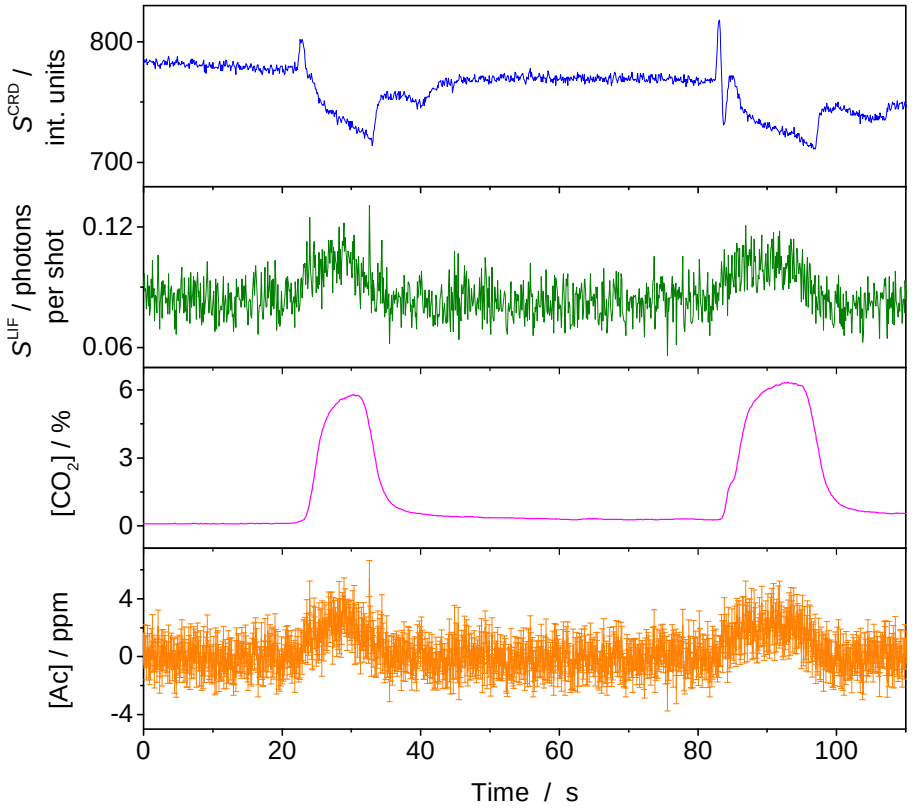

Figure 5.8: Breath acetone signal measured using the end-tidal breath sampler from a healthy test subject that fasted for 18 hours. The measurements were taken at sampler temperature of 50 °C, breathing flow rate of 10 L m^{-1} and sampling flow of 0.5 slpm.

healthy subjects. However, we were unable to test the effect of different sampler temperatures or different breath flow rate on the breath acetone concentration, as at this stage normal breath acetone concentration of healthy subjects could not be measured. In the next chapter, a high pulse energy laser is used to explore the ability to lower the CELIF LOD and expand the CELIF dynamic range.

Chapter 6

CELIF Measurements with High Laser Pulse Energy

An Elforlight laser with a 15 kHz repetition rate and a pulse energy of 0.02 μJ was used to measure acetone concentration, [Ac], as low as 1.6 ppm when averaging 1500 laser shots in 100 ms. As discussed in chapter 2, the limit of detection (LOD) of the CELIF measurement of the acetone concentration scales with the laser energy and the background LIF signal as

$$\alpha_{\mathrm{LOD}}^{3\sigma} = \frac{3}{\mathcal{K} S_0^{\mathrm{CRD}}} \sqrt{2 \frac{S_{\mathrm{bg}}^{\mathrm{LIF}}}{n}} \,. \tag{6.0.1}$$

A more powerful laser, Surelite pulsed Nd:YAG laser (SL I-10), with a 10 Hz repetition rate, and pulse energy 10–200 μJ was used to investigate the limit of detection of acetone concentration and to determine the dynamic range of the CELIF measurement at higher laser pulse energies. Laser pulse energies higher than 200 μJ were achievable, however, we were limited by the damage threshold of the optics. The power consumption of this large Surelite laser is 2.2–2.4 kW, and it requires water cooling, compared to 100 W power consumption, and air cooling of the previously used, portable, Elforlight laser.

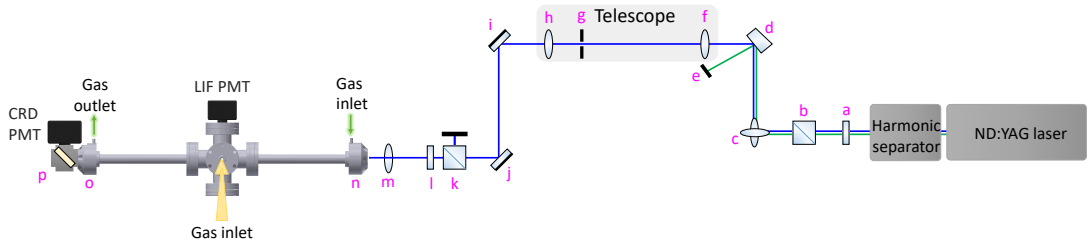

Figure 6.1: A schematic of the experimental setup using the 10 Hz, 266 nm laser.

6.1 Laser Setup

Before doing any measurement with this new laser, we needed to choose the right optics for the telescope and the optics components needed to couple the laser beam into the optical cavity. Figure 6.1 shows the CELIF experimental setup with the Surelite laser. First, the 266 nm beam is passed through a half wave plate, which helps to get the desired pulse energy, followed by a Glan-laser prism, which allows only the horizontal polarisation of the beam. Next, the beam is directed through a set of periscope mirrors that rotate the polarisation to vertical and send the beam to a Pellin-Broca prism to separate the remaining 532 nm beam. The beam is then directed to a set of telescope lenses, a focusing lens (f = 500 mm), and a collimating lens (f = 50 mm). Finally, the beam is sent to the cavity using the two dichroic mirrors as described in section 3.1.

6.1.1 Energy Reducing Surface

The CRD PMT must not be exposed to high laser pulse energy to prevent both the PMT and the integrator from signal saturation. Two different surfaces were used for this purpose. Each surface was mounted at 45° from the cavity axis inside a cube mount. The CRD PMT is connected on the other side of the cube at 90° from the cavity axis, as shown in figure 6.1. We used a glass plate, which reflects 14% of the light with laser pulse energies lower than 50 μJ. The CRD PMT supply voltage

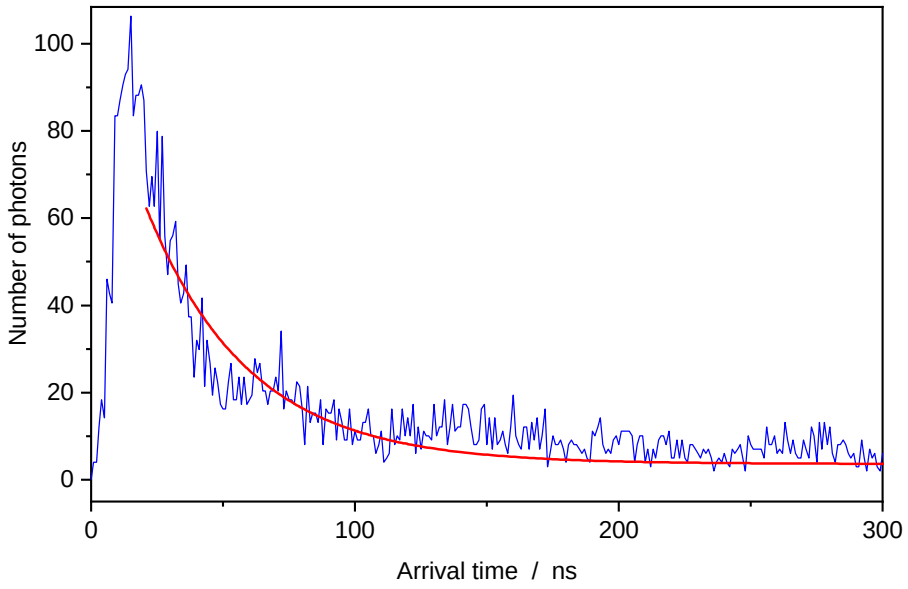

Figure 6.2: The blue curve is a histogram of the arrival time of background photons taken from 512 laser shots, and a laser pulse energy of 2900 int. units. The red curve is a fit to a single exponential decay.

was 350 V. A UVFS coated plano-convex lens, f = 1000 mm, reflected 5% of the light with pulse energies from 200 down to 50 μJ and CRD PMT supply voltage was set to 550 V. Laser pulse energies of more than 200 μJ were above the damage threshold of the dichroic mirror after the telescope.

6.1.2 The Error in Ring-Down Time

Our procedure for the CELIF measurements made with the Surelite laser was slightly different than the procedure used with Elforlight laser. With the Elforlight laser, the cavity was pumped down and left under vacuum between different CELIF measurements, which caused vibrations on the cavity mirrors and yielded a fractional error in the ring-down time of 0.02, as discussed in section 3.1.1. With the Surelite laser, after each acetone CELIF measurement, the flow was diverted into a flow of pure gas nitrogen without disturbing the pressure of the cavity. This eliminated the effect of pumping down the cavity on cavity mirrors vibrations and reduced the statistical error on the ring-down time, and hence the CRD limit of detection.

While this procedure would have been beneficial for the previous CELIF mea-

surements which we made with the low power Elforlight laser, it was not possible to repeat the low power measurements during the last months left to finish this poject.

Each CRD transient recorded with the Surelite laser was an average of 512 CRD transients. To find the fractional error in τ, 100 CRD transients were recorded using 1 bar of N_2, each was averaged over 512 laser shots. Each averaged transient was fitted to a single exponential decay to find τ_0 and the standard deviation. This standard deviation is the same as the standard error when recording a single CRD measurement where the CRD transient is an average of 512 transients. The statistical error in τ_0 and τ is then calculated from the fractional error:

$$\frac{\delta\tau}{\tau} = 0.004\,.$$

6.2 Investigating the Dependence of $S_{\mathbf{bg}}^{\mathbf{LIF}}$ and $S_{\mathbf{bg}}^{\mathbf{CELIF}}$ on the Laser Pulse Energy

To investigate the dependence of $S_{\mathrm{bg}}^{\mathrm{LIF}}$ and $S_{\mathrm{bg}}^{\mathrm{CELIF}}$ on the laser pulse energy as measured by S_0^{CRD}, background CELIF measurements were taken at different laser pulse energies. Each measurement was an average of 512 laser shots and was taken while longitudinally flowing 1 bar of N_2 gas at a mass flow rate of 0.5 slpm. The CRD and LIF transients and the arrival time of the photons were recorded for all the measurements. Figure 6.2 shows the histogram of arrival time of background photons when using a high laser pulse energy of 2900 int. units. The histogram does not follow a single exponential decay as expected. Thus, the under-counting correction using Eqn 2.3.52 cannot be done. The number of photons in each time bin should be corrected separately. This could be done using Eqn 2.3.46, which gives

$$S_{\mathrm{cor}}^{\mathrm{LIF}} = n\left(-\ln\left(1-\frac{S_{\mathrm{c}}^{\mathrm{LIF}}}{n}\right)\right)\,, \tag{6.2.2}$$

where $S_{\mathrm{cor}}^{\mathrm{LIF}}$ is the corrected number of photons in each time bin, $S_{\mathrm{c}}^{\mathrm{LIF}}$ is the counted number of photons in each time bin, and n is the number of laser shots.

We expect $S_{\mathrm{bg}}^{\mathrm{LIF}}$ to be linearly proportional to S_0^{CRD}, however, as seen in figure 6.3, it is not. Thus, $S_{\mathrm{bg}}^{\mathrm{CELIF}}$ is not constant with changing laser pulse energy as shown in figure 6.4 (a). We examined the linearity of $S_{\mathrm{bg}}^{\mathrm{LIF}}$ depending on the arrival time

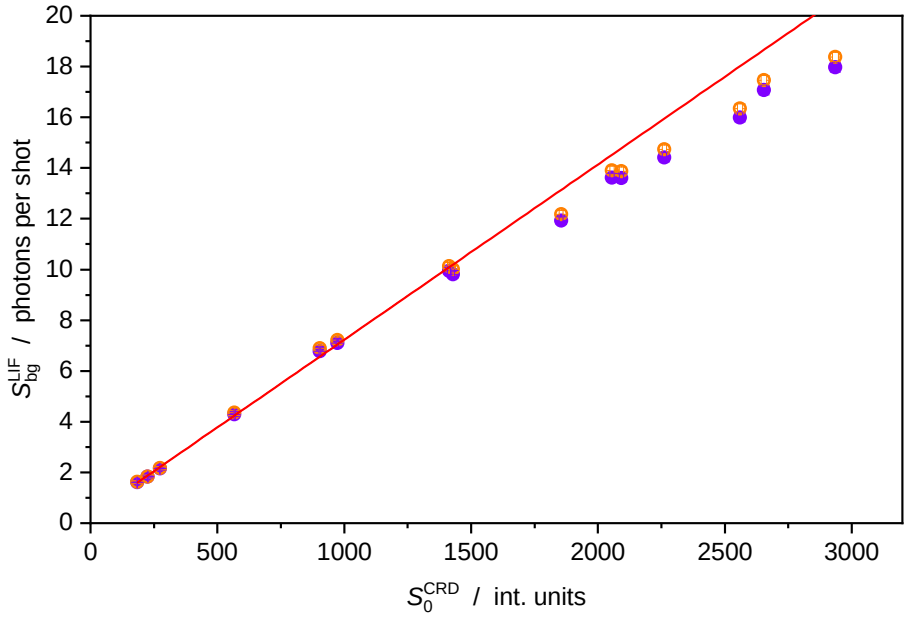

Figure 6.3: Dependence of the background LIF signal on the laser pulse energy, as measured by the time-integrated ring-down signal. The purple filled circles are the counted number of photons. The orange empty circles are the under-counting corrected number of photons using Eqn 6.2.2. The orange line is a linear fit of the corrected data. The statistical error bars are smaller than the symbols. Each measurement was taken from an average of 512 laser shots, using 1 bar of N_2 at 0.5 slpm. The ring-down time, τ_0, in these measurements was 695 ± 15 ns.

of the photons. Background photons were counted from the beginning of the LIF signal, $t = 0$, to the ring-down time of the equivalent ring-down transient, $t = \tau_0$, which gives $S^{\mathrm{LIF}}_{\mathrm{bg}\,t<\tau_0}$, and from $t = \tau_0$ onward, which gives $S^{\mathrm{LIF}}_{\mathrm{bg}\,t>\tau_0}$. As shown in figure 6.5, $S^{\mathrm{LIF}}_{\mathrm{bg}\,t>\tau_0}$ is linearly proportional to S_0^{CRD} as expected. However, $S^{\mathrm{LIF}}_{\mathrm{bg}\,t<\tau_0}$ is not linear with laser pulse energy. This implies that all of the photons after τ_0 are coupled into the cavity, but at the beginning of the decay there are extra, uncoupled photons which cause the non-linearity. These extra photons, ϕ, come from the high energy laser hitting the cavity mirrors that cause detectable fluorescence, which decays faster than the rest of the background photons.

To calculate $S^{\mathrm{CELIF}}_{\mathrm{bg}}$ which comes from the coupled light, ϕ needs to be calculated first. For that, we count photons (and correct for under-counting if needed) in all the time bins of the LIF transients, $S^{\mathrm{LIF}}_{\mathrm{bg\,all}}$, including coupled and uncoupled photons,

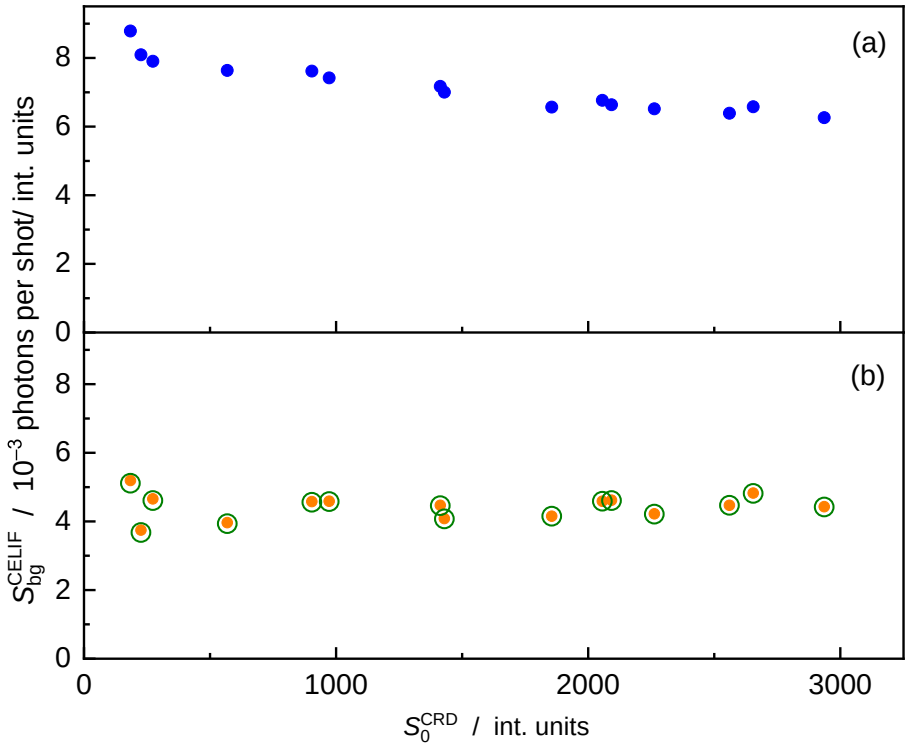

Figure 6.4: Dependence of the background CELIF signal on the laser pulse energy as measured by the time-integrated ring-down signal. (a) The background CELIF signal is calculated from the counted and corrected number of photons per shot in the exponential decay of the LIF transient without subtracting ϕ. (b) The orange circles are the background CELIF signals as calculated from Eqn 6.2.7, and the green circles are the background CELIF signals as calculated from Eqn 6.2.8. Each measurement is taken from an average of 512 laser shots, using 1 bar of N_2 at 0.5 slpm.

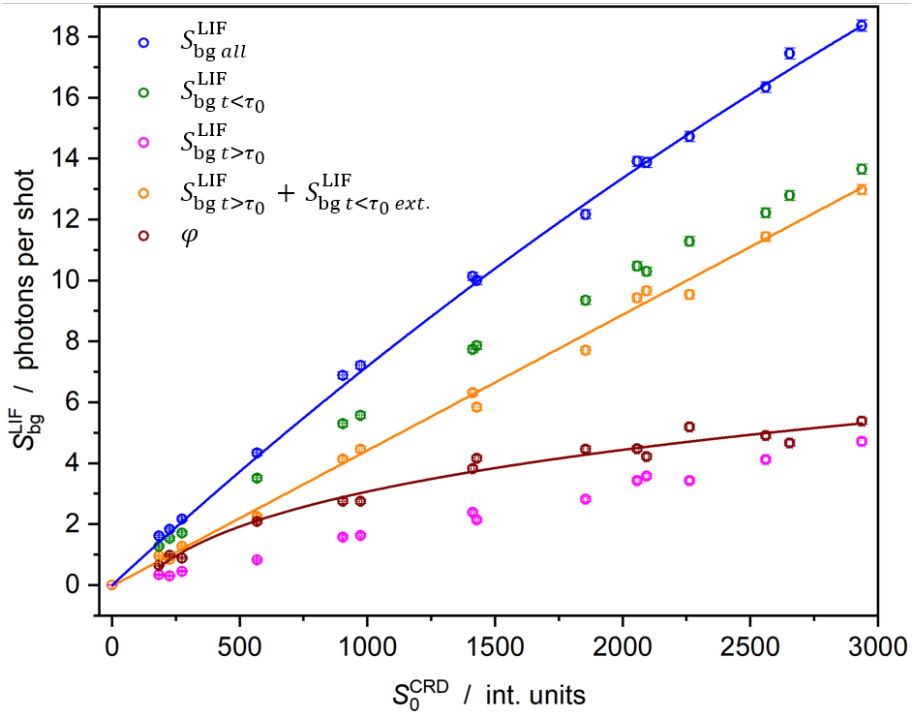

Figure 6.5: Dependence of the background LIF signal, based on the arrival time of the photons, on the laser pulse energy as measured by the time-integrated ring-down signal. All data are corrected for under-counting using Eqn 6.2.2. The blue line is a non linear fit of the form $S_{\mathrm{bg\,all}}^{\mathrm{LIF}} = a\left(1 - \exp\left(-bS_0^{\mathrm{CRD}}\right)\right)$. The orange line is a linear fit. The dark red line is a fit of ϕ to a power series model $\phi = a + b(S_0^{\mathrm{CRD}})^{\mathrm{c}}$. The statistical error bars are from one standard error. Each measurement is taken from an average of 512 laser shots, using 1 bar of N_2 at 0.5 slpm.

and count $S^{\mathrm{LIF}}_{\mathrm{bg}\,t>\tau_0}$, and then extrapolate back the coupled photons before $t = \tau_0$, $S^{\mathrm{LIF}}_{\mathrm{bg}\,t<\tau_0\,ext.}$:

$$S^{\mathrm{LIF}}_{\mathrm{bg}\,t<\tau_0\,ext.} = \frac{S^{\mathrm{CRD}}_{0\,t<\tau_0}}{S^{\mathrm{CRD}}_{0\,t>\tau_0}} \cdot S^{\mathrm{LIF}}_{\mathrm{bg}\,t>\tau_0}\,, \tag{6.2.3}$$

where, $S^{\mathrm{CRD}}_{0\,t>\tau_0}$ is the time integrated CRD signal from $t = \tau_0$ onward:

$$S^{\mathrm{CRD}}_{0\,t>\tau_0} = S^{\mathrm{CRD}}_{0} \exp(-\tau_0/\tau_0) \approx 0.37 \cdot S^{\mathrm{CRD}}_{0}\,, \tag{6.2.4}$$

and $S^{\mathrm{CRD}}_{0\,t<\tau_0}$ is the time integrated CRD signal from $t = 0$ to τ_0:

$$S^{\mathrm{CRD}}_{0\,t<\tau_0} = S^{\mathrm{CRD}}_{0} - S^{\mathrm{CRD}}_{0\,t>\tau_0}\,. \tag{6.2.5}$$

ϕ is then calculated as

$$\phi = S^{\mathrm{LIF}}_{\mathrm{bg\,all}} - \left(S^{\mathrm{LIF}}_{\mathrm{bg}\,t>\tau_0} + S^{\mathrm{LIF}}_{\mathrm{bg}\,t<\tau_0\,ext.}\right)\,. \tag{6.2.6}$$

As seen in figure 6.5, ϕ is not linear with laser pulse energy, but follows a power series model:

$$\phi = a + b(S^{\mathrm{CRD}}_{0})^{\mathrm{c}}\,,$$

with the power constant, $c = 0.25 \pm 0.13$. After that, $S^{\mathrm{CELIF}}_{\mathrm{bg}}$ is calculated as

$$S^{\mathrm{CELIF}}_{\mathrm{bg}} = \frac{S^{\mathrm{LIF}}_{\mathrm{bg\,all}} - \gamma - \phi}{S^{\mathrm{CRD}}_{0}}\,. \tag{6.2.7}$$

Another way of calculating $S^{\mathrm{CELIF}}_{\mathrm{bg}}$ is to analyse both LIF and CRD transients after $t = \tau_0$ to avoid any issues coming from uncoupled light or saturation at the beginning of the transients, and without the need to calculate ϕ. This could be done using $S^{\mathrm{LIF}}_{\mathrm{bg}\,t>\tau_0}$ and $S^{\mathrm{CRD}}_{0\,t>\tau_0}$, as

$$S^{\mathrm{CELIF}}_{\mathrm{bg}} = \frac{S^{\mathrm{LIF}}_{\mathrm{bg}\,t>\tau_0} - \gamma}{S^{\mathrm{CRD}}_{0\,t>\tau_0}}\,. \tag{6.2.8}$$

Eqn's 6.2.7 and 6.2.8 both give constant $S^{\mathrm{CELIF}}_{\mathrm{bg}}$, and they both give same results as seen in figure 6.4 (b). Using Eqn 6.2.8 simplifies the CELIF analysis by removing the need of propagating the statistical error in ϕ.

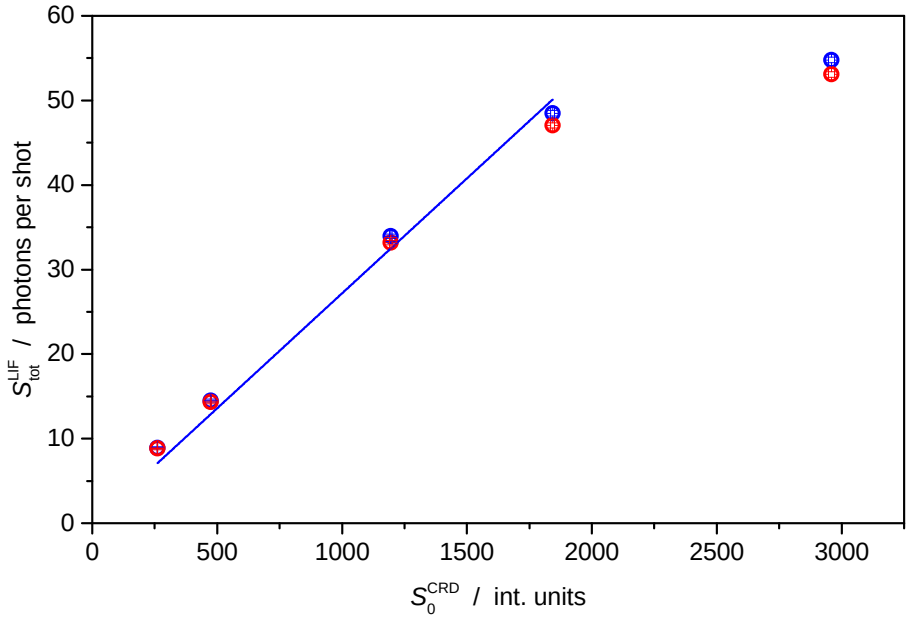

Figure 6.6: Dependence of the acetone LIF signal on the laser pulse energy as measured by the time-integrated ring-down signal. The red circles are the counted number of photons. The blue circles are the under-counting corrected number of photons, calculated using Eqn 6.2.2. The blue line is a linear fit of the corrected data. The statistical error bars are smaller than the symbols. Each measurement is taken from an average of 512 laser shots, using 1 bar of 40 ppm acetone in N_2 mixture at 0.5 slpm.

6.3 Investigating the Dependence of $S_{\mathbf{tot}}^{\mathbf{LIF}}$ and $S_{\mathbf{sample}}^{\mathbf{CELIF}}$ on the Laser Pulse Energy

To investigate the dependence of the acetone LIF and CELIF signals, $S_{\mathrm{tot}}^{\mathrm{LIF}}$ and $S_{\mathrm{sample}}^{\mathrm{CELIF}}$, on the laser pulse energy as measured by S_0^{CRD}, acetone CELIF measurements were taken at different laser pulse energies. Each measurement was averaged over 512 laser shots and was taken using 1 bar of a gas mixture of acetone in N_2 at longitudinal mass flow rate of 0.5 slpm. The same acetone mixture concentration, 40 $\pm$ 0.4 ppm, was used for all the measurements. The CRD and LIF transients and the arrival time of the photons were recorded for all the measurements. The number of acetone photons was corrected for each time bin using Eqn 6.2.2. Figure 6.6 shows how $S_{\mathrm{tot}}^{\mathrm{LIF}}$ vs. S_0^{CRD} deviates from linearity at high laser pulse energy. The

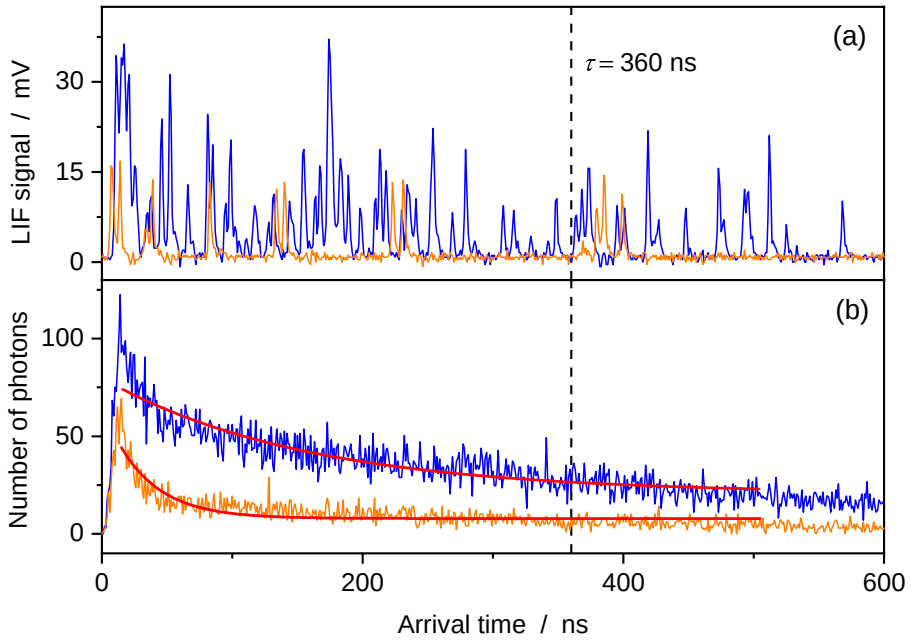

Figure 6.7: (a) Acetone LIF transients (the last of 512 laser shots), and (b) histogram of the arrival time of photons, recorded with a laser pulse energy, as measured by S_0^{CRD}, of 2900 int. units (blue curve), and 470 int. units (orange curve). The measurements were all recorded while longitudinally flowing 1 bar of 40 ppm acetone in N_2 mixture at 0.5 slpm. The histogram is from 512 laser shots, and it was corrected for under-counting using Eqn 6.2.2.

reason for this is illustrated in figure 6.7. At the beginning of the LIF transient the LIF signal is saturated when measured with high laser pulse energy, and the photon under-counting correction can not be applied. The histogram of the arrival time of the acetone photons does not follow a single exponential decay as expected even after applying under-counting correction. Thus, the LIF signal measured with high laser pulse energy should be time-integrated and not photon counted.

Thus, to overcome this issue, to analyse the acetone LIF signal, the photons in the initial region of the LIF decay must not be counted. Photons should be counted from $t = \tau$ onward, $S^{\mathrm{LIF}}_{\mathrm{tot}\,t>\tau}$, as the LIF signal and the histogram are not saturated after $t = \tau$ (dashed black line in figure 6.7). $S^{\mathrm{LIF}}_{\mathrm{tot}\,t>\tau}$ is linearly proportional to S_0^{CRD} as seen in figure 6.8. $S^{\mathrm{CELIF}}_{\mathrm{sample}}$ becomes

$$S^{\mathrm{CELIF}}_{\mathrm{sample}} = \frac{S^{\mathrm{LIF}}_{\mathrm{tot}\,t>\tau} - \gamma}{S^{\mathrm{CRD}}_{t>\tau}} - S^{\mathrm{CELIF}}_{\mathrm{bg}}\,, \tag{6.3.9}$$

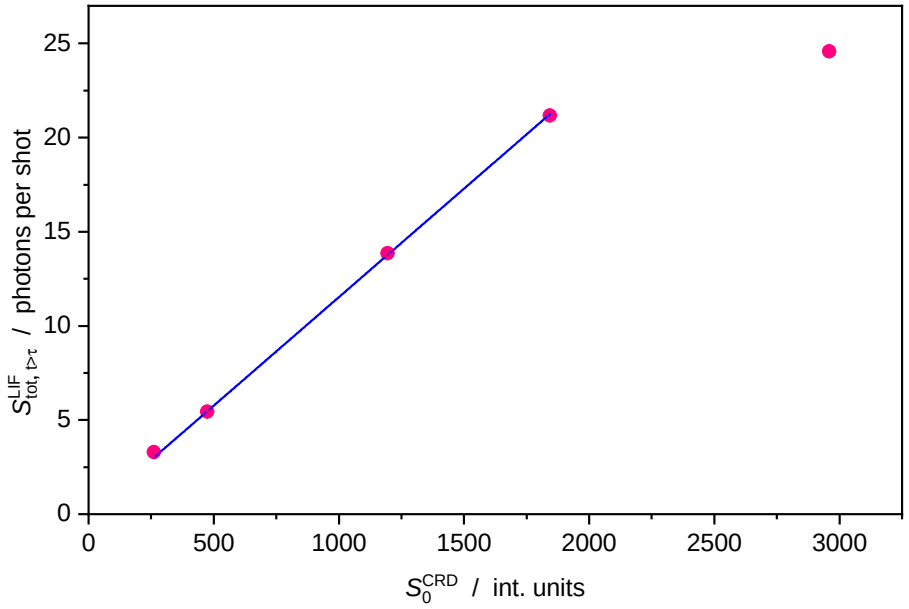

Figure 6.8: Dependence of the acetone LIF signal, counted after $t = \tau$, on the laser pulse energy as measured by the time-integrated ring-down signal. The blue line is a linear fit of the data. Each measurement is an average of 512 laser shots, and recorded while longitudinally flowing 1 bar of 40 ppm acetone in N_2 mixture at 0.5 slpm. All data are corrected for under-counting using Eqn 6.2.2. The statistical error bars are smaller than the symbols.

where $S^{\mathrm{CRD}}_{t>\tau}$ is the time integrated CRD signal after $t = \tau$. Following the error analysis in chapter 2 the statistical error in $S^{\mathrm{CELIF}}_{\mathrm{sample}}$ therefore becomes

$$\delta S^{\mathrm{CELIF}}_{\mathrm{sample}} = \left\{ \frac{S^{\mathrm{LIF}}_{\mathrm{tot}\,t>\tau}}{n(S^{\mathrm{CRD}}_{t>\tau})^2} + \frac{S^{\mathrm{LIF}}_{\mathrm{bg}\,t>\tau}}{n(S^{\mathrm{CRD}}_{0\,t>\tau})^2} + \frac{f^2\left(S^{\mathrm{LIF}}_{\mathrm{bg}\,t>\tau} - \gamma\right)^2}{(S^{\mathrm{CRD}}_{0\,t>\tau})^2} + \frac{f^2\left(S^{\mathrm{LIF}}_{\mathrm{tot}\,t>\tau} - \gamma\right)^2}{(S^{\mathrm{CRD}}_{t>\tau})^2} + \frac{\gamma(S^{\mathrm{CRD}}_{t>\tau} - S^{\mathrm{CRD}}_{0\,t>\tau})^2}{n(S^{\mathrm{CRD}}_{t>\tau})^2(S^{\mathrm{CRD}}_{0\,t>\tau})^2} \right\}^{1/2} . \tag{6.3.10}$$

Figure 6.8 shows that the measurement taken at the highest laser pulse energy is saturated and does not lineup with the rest of the data. This is because the CELIF signal at this laser pulse energy is above the higher limit of detection, and the LIF signal must be time-integrated and not photon counted.

Calculating $S^{\mathrm{CELIF}}_{\mathrm{sample}}$ using Eqn 6.3.9 gives a constant $S^{\mathrm{CELIF}}_{\mathrm{sample}}$ as seen in figure 6.9 (b) compared to the changing $S^{\mathrm{CELIF}}_{\mathrm{sample}}$ if the photons were counted in all the acetone LIF decay as shown in figure 6.9 (a). Eqn 6.3.9 also simplifies the CELIF analysis and removes the need to deal with saturated LIF signals at the beginning of the LIF transients.

6.4 Acetone CELIF Limit of Detection

At the limit of detection, the measured total signal should be three standard deviations, 3σ, above the background signal:

$$S^{\mathrm{CELIF}}_{\mathrm{sample}}\big|_{3\sigma\,\mathrm{LOD}} = 3\,\delta S^{\mathrm{CELIF}}_{\mathrm{bg}} . \tag{6.4.11}$$

At the limit of detection, the ring-down times with and without sample should be indistinguishable within experimental uncertainties, $\tau = \tau_0$. Consequently, $S^{\mathrm{CRD}} = S^{\mathrm{CRD}}_0$. Also, $S^{\mathrm{LIF}}_{\mathrm{tot}} \to S^{\mathrm{LIF}}_{\mathrm{bg}}$. Substituting in Eqn 6.3.10:

$$\delta S^{\mathrm{CELIF}}_{\mathrm{bg}} = \left\{ 2\frac{S^{\mathrm{LIF}}_{\mathrm{bg}\,t>\tau}}{n(S^{\mathrm{CRD}}_{0\,t>\tau})^2} + 2\frac{f^2\left(S^{\mathrm{LIF}}_{\mathrm{bg}\,t>\tau} - \gamma\right)^2}{(S^{\mathrm{CRD}}_{0\,t>\tau})^2} \right\}^{1/2} . \tag{6.4.12}$$

In the limit $f \to 0$, the last term in Eqn 6.4.12 is negligible. The limit of detection simplifies to

$$S^{\mathrm{CELIF}}_{\mathrm{sample}}\big|_{3\sigma\,\mathrm{LOD}} = \frac{3}{S^{\mathrm{CRD}}_{0\,t>\tau}}\sqrt{\frac{2S^{\mathrm{LIF}}_{\mathrm{bg}\,t>\tau}}{n}} . \tag{6.4.13}$$

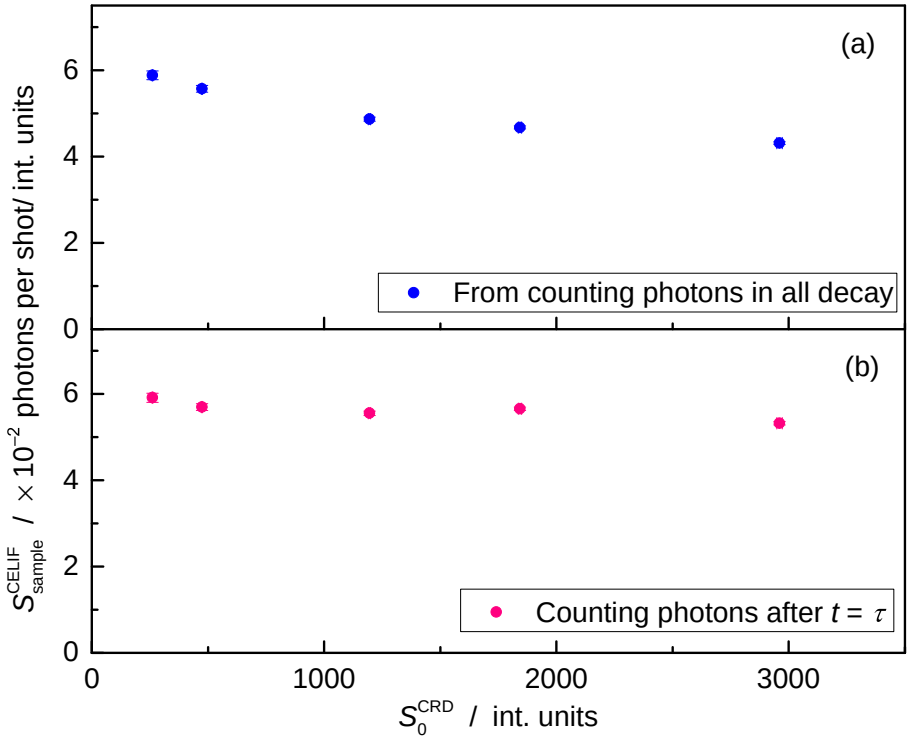

Figure 6.9: Dependence of the acetone CELIF signal on the laser pulse energy as measured by the time-integrated ring-down signal. (a) The CELIF signal is calculated from the counted and corrected number of photons per shot in all the exponential decay of the LIF transient. (b) The CELIF signal is calculated using Eqn 6.3.9. The statistical error bars are smaller than the symbols. Each measurement is an average of 512 laser shots, and recorded while longitudinally flowing 1 bar of 40 ppm acetone in N_2 mixture at 0.5 slpm.

And the acetone concentration at the 3σ limit of detection is

$$[\mathrm{Ac}]_{3\sigma\,\mathrm{LOD}} = \frac{3}{\mathcal{K}' S^{\mathrm{CRD}}_{0\,t>\tau}} \sqrt{\frac{2 S^{\mathrm{LIF}}_{\mathrm{bg}\,t>\tau}}{n}}\,. \tag{6.4.14}$$

where,

$$\mathcal{K}' = \frac{p\,\sigma}{k_{\mathrm{B}}\,T}\,\mathcal{K}\,. \tag{6.4.15}$$

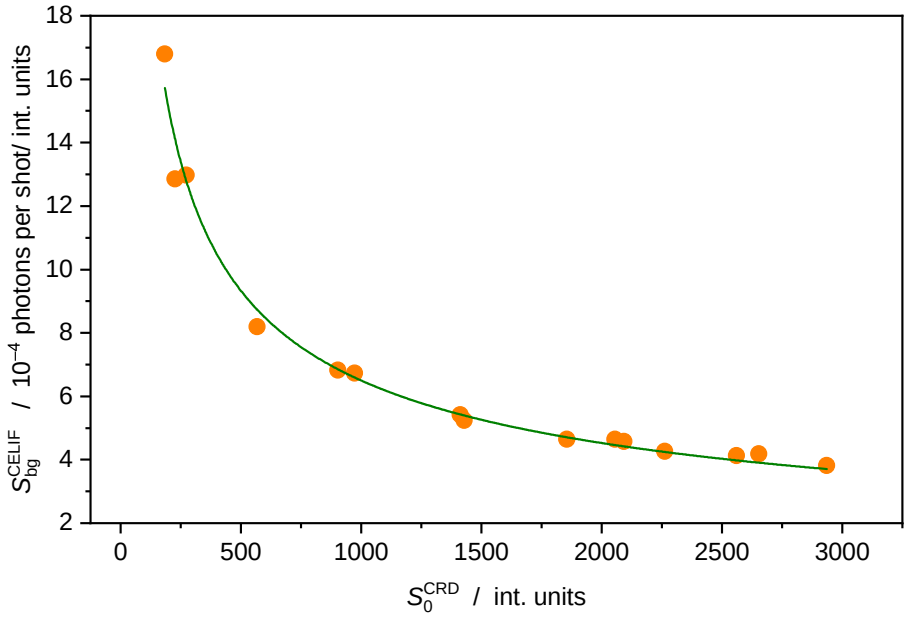

Figure 6.10: Dependence of the CELIF LOD of acetone concentration on the laser pulse energy as measured by the time-integrated ring-down signal. The green line is a fit using $S_{\mathrm{bg}}^{\mathrm{CELIF}} = a \cdot (S_0^{\mathrm{CRD}})^b$. Each measurement is an average of 512 laser shots, and recorded using 1 bar of N_2 at 0.5 slpm.

6.4.1 Scaling CELIF LOD with the Laser Pulse Energy

The background photons counted after $t = \tau_0$ are linearly proportional to the laser pulse energy, as measured by the time integrated ring-down signal,

$$S_{\mathrm{bg}\,t>\tau}^{\mathrm{LIF}} \propto S_{0\,t>\tau}^{\mathrm{CRD}}\,.$$

Substituting in Eqn 6.4.14, at constant number of shots, n, and using the same calibration, $\mathcal{K}'$:

$$[\mathrm{Ac}]_{\mathrm{LOD}} \propto \sqrt{(S_{0\,t>\tau}^{\mathrm{CRD}})^{-1}}\,, \tag{6.4.16}$$

The dependence of the CELIF LOD on the laser pulse energy was confirmed by measuring $S_{\mathrm{bg}}^{\mathrm{CELIF}}$ at different laser pulse energies, as shown in figure 6.10. The data points were fitted to a non-linear form:

$$S_{\mathrm{bg}}^{\mathrm{CELIF}} = a \cdot (S_0^{\mathrm{CRD}})^b\,,$$

where a and b are constants, and the fit yeilded $b = -0.52 \pm 0.02$.

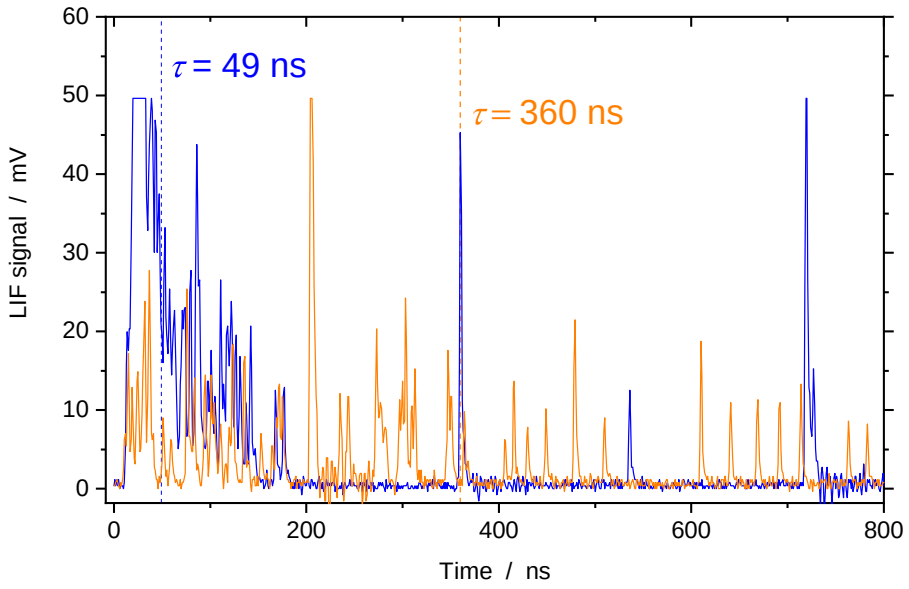

Figure 6.11: Acetone LIF transients recorded with laser pulse energy of 2600 int. units. The blue curve is the LIF signal at 556 ppm and the orange curve is the LIF signal at 42 ppm. The transients were all recorded using 1 bar of the gas mixtures at 0.5 slpm.

Thus, as discussed in chapter 2, the CELIF limit of detection can be lowered by reducing the detection of background photons:

$$S^{\mathrm{CELIF}}_{\mathrm{sample}}\big|_{3\sigma\,\mathrm{LOD}} \propto S^{\mathrm{LIF}}_{\mathrm{bg}\,t>\tau}\,,$$

or by increasing the number of laser shots or the laser intensity:

$$S^{\mathrm{CELIF}}_{\mathrm{sample}}\big|_{3\sigma\,\mathrm{LOD}} \propto (nS^{\mathrm{CRD}}_{0\,t>\tau})^{-1/2}\,.$$

6.5 Acetone CELIF Dynamic Range

To explore the dynamic range of the acetone CELIF measurement, calibration measurements were performed at different laser pulse energies, as seen in figure 6.12. The lower LOD of CELIF is limited by the background photons which result from both stray light and the fluorescence of the cavity mirrors. The higher CELIF LOD is limited by the inability to count photons at high laser pulse energies or high acetone concentrations. The blue curve in figure 6.11 shows an example of a saturated

LIF transient, which was recorded from a mixture of [Ac] = 556 ppm, using a pulse energy of 2600 int. units. Even after $t = \tau$, the transient should be time-integrated as photon counting will not give correct results. The orange curve shows a LIF transient recorded from a mixture of [Ac] = 42 ppm, using the same pulse energy. It is clear in figure 6.11 that at 556 ppm the signal is above the CELIF higher LOD, while at 42 ppm the signal is within the dynamic range of CELIF using the pulse energy 2600 int. units.

The calibration measurements were made by successive dilutions of a gas mixture of acetone in N_2 using the procedure described in section 4.2.2. The repetition rate of the Surelite laser is 10 Hz, and the 1500 averaged shots required having a larger gas mixing bottle to be able to flow the sample for a longer period of time, which was not available. Thus, the number of laser shots, n, was limited to 512. $S_{\text{bg}}^{\text{CELIF}}$ and $S_{\text{sample}}^{\text{CELIF}}$ analysis was done using the procedure described in section 6.2 and 6.3 respectively. $S_{\text{sample}}^{\text{CELIF}}$ was plotted against the [Ac] as measured by CRD, as seen in figure 6.12 (a), (c) and (e). Data above the CRD LOD was fitted using a non-linear model

$$S_{\text{sample}}^{\text{CELIF}} = a\left(1 - \exp\left(-b\left[Ac\right]\right)\right) ,$$

where a is the plateau value at infinite [Ac], and b is the time constant. Next, the data was fitted using a straight line, which is the tangent of the exponential curve,

$$S_{\text{sample}}^{\text{CELIF}} = a \cdot b \cdot \left[Ac\right] .$$

The residuals of the exponential fit and the residuals of the tangent fit were plotted against the [Ac] in figure 6.12 (b) and (d). When the tangent line residuals deviated from 0, then these data points were excluded from the calibration fit, as the photon counting was not valid anymore and the LIF transients should be time-integrated. The CRD 3σ LOD was calculated using Eqn 2.2.5. In the calibration graph, data points above the CRD LOD and below the CELIF higher LOD were then fitted using a linear fit,

$$S_{\text{sample}}^{\text{CELIF}} = \mathcal{K}'\left[Ac\right] , \tag{6.5.17}$$

where the slope $\mathcal{K}'$ is the calibration factor. Finally, $[\text{Ac}]_{3\sigma\,\text{LOD}}$ was calculated from Eqn 6.4.14. Table 6.1 summaries all the calibration measurements made with the

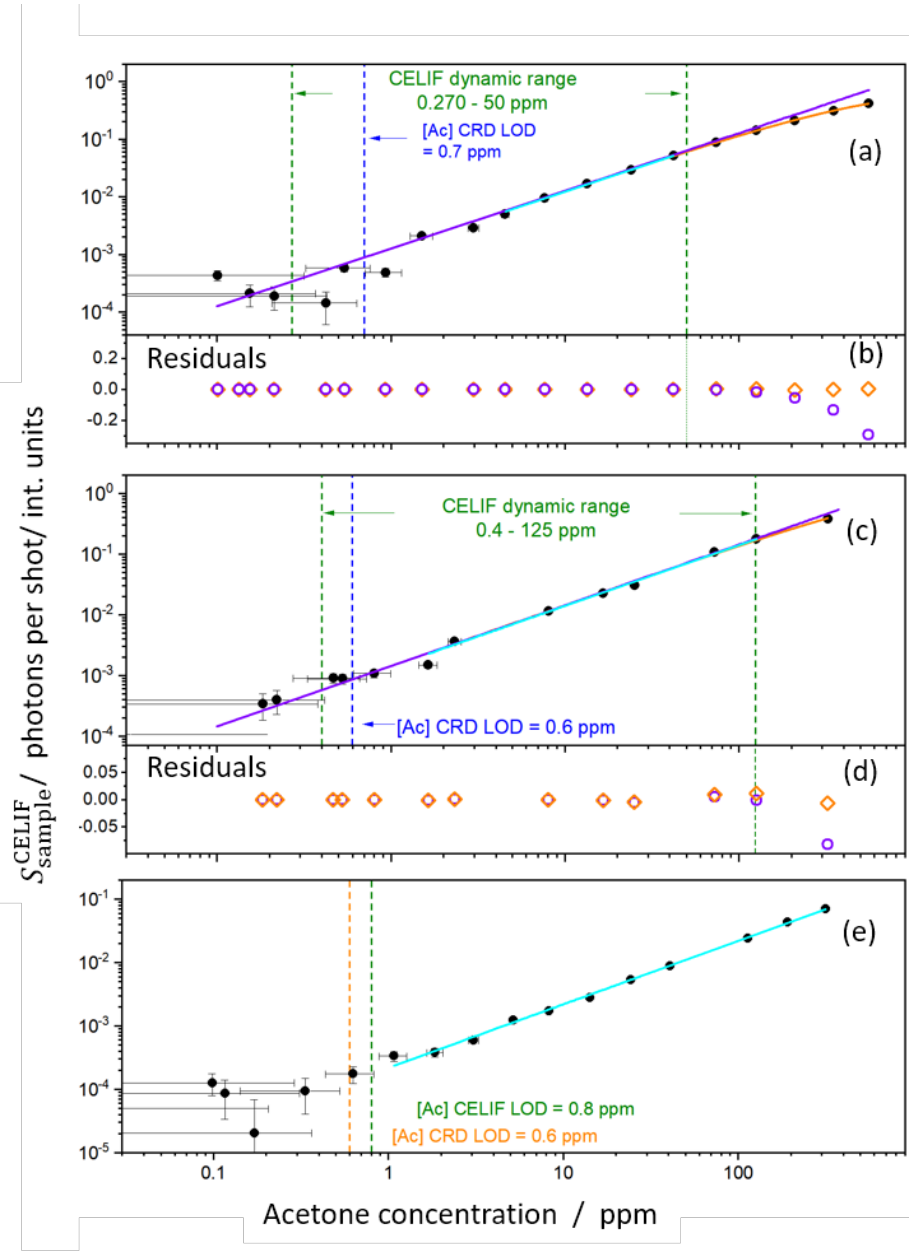

Figure 6.12: Determination of the limit of detection of the acetone CELIF measurement by successive dilution of an acetone–N_2 gas mixture, using a laser pulse energy of 170 ± 17 µJ, 100 ± 10 µJ and 45 ± 5 µJ in (a), (c) and (e) respectively. The orange curve is a fit using $S^{\mathrm{CELIF}}_{\mathrm{sample}} = a\,(1 - \exp(-b\,[Ac]))$. The purple line is a fit using the tangent $S^{\mathrm{CELIF}}_{\mathrm{sample}} = a \cdot b \cdot [Ac]$. The cyan line is the calibration linear fit. Each measurement was an average of 512 laser shots and was recorded while longitudinally flowing the gas sample at 0.5 slpm. The statistical error bars are from one standard error. The orange diamonds in (b) and (d) are the residuals of the exponential fit, and the purple circles are the residuals of the tangent fit.

Table 6.1: Comparison between the calibration measurements at different laser pulse energies.

Pulse energy (μJ)	S_0^{CRD} (int. units)	$S_{\mathrm{bg}}^{\mathrm{LIF}}$ (photons per shot)	$\mathcal{K}'$	CELIF dynamic range (ppm)
170 ± 17	2660 ± 11	19 ± 0.19	$1.21 \times 10^{-3} \pm 2.09 \times 10^{-5}$	0.270 - 50
100 ± 10	1500 ± 6	11 ± 0.15	$1.39 \times 10^{-3} \pm 4.15 \times 10^{-5}$	0.4 - 125
45 ± 5	1600 ± 6	1.7 ± 0.06	$2.19 \times 10^{-4} \pm 2.73 \times 10^{-6}$	0.8 - not measured

Surelite laser. Note that in the calibration made using a laser pulse energy of $45 \pm 5\mu$J, the measurements were within the CELIF dynamic range, as shown in figure 6.12 (e), and the exponential fit was not needed.

The high laser pulse energy improved the acetone CELIF 3σ LOD from 1.6 ppm, measured every 100 ms (averaging every 1500 shots) by the low energy, 15 kHz laser to as low as 0.270 ppm measured every 52 s (averaging every 512 shots) which was measured with the high energy, 10 Hz laser. However, the CELIF measurements reached the higher LOD faster with the high intensity laser (50 ppm at the highest laser pulse energy), compared to more than 1000 ppm measured with low energy laser, due to the photon counting regime limit.

Final conclusions and recommendations on measuring breath acetone in real-time with a wide CELIF dynamic range are presented in the next chapter.

Chapter 7

Conclusions and Future Work

7.1 Conclusions

The commonest cause of death in children with type 1 diabetes is diabetic ketoacidosis (DKA), caused by high concentrations of acidic blood ketones. There is an unmet need for alternative, non-invasive methods to untimely blood tests to monitor patient response in real time during treatment. Current near-patient blood ketone tests are inaccurate at high ketone concentrations. Breath acetone measurement is an alternative as it is proportional to blood ketone concentrations.

We have built a laser-based device to measure acetone concentration in gas samples using cavity-enhanced laser-induced fluorescence. This spectroscopic technique is a cross-correlated combination of cavity ring-down spectroscopy (CRDS) and laser-induced fluorescence (LIF). The laser system has been characterised and the optical setup for the telescope and the LIF optics has been optimised. An analog integrator has been built to measure the time integrated CRD signal. The integrator, along with a digitizer card were used for the CRD and LIF data acquisition. A suite of LabView programs has been written and implemented in the experiment for CELIF data acquisition and analysis.

We have found that, to allow the CELIF device to perform online, real-time breath acetone measurements, CRD and CELIF measurements must be made with a flowing gas sample, and not with a sample contained in a static chamber. It was found that making acetone CELIF measurements on a stagnant gas sample does

not give the real acetone concentration. This is probably caused by degradation of the acetone molecules due to photobleaching as the static molecules were exposed to increasing numbers of laser pulses.

To make sensitive CRD measurements for the CELIF calibration, the CRD measurements must be made with longitudinal sample flow (along the cavity axis), while the CELIF measurements must be made with transverse flow (perpendicular to the cavity axis) through the flow-body to reduce the residence time of the samples in the device and to extend the dynamic range of the CELIF measurements by preserving the laser intensity along the cavity axis. The transverse flow of the gas through the flow-body gives a higher limit of detection of the CELIF device of more than 2000 ppm, winning over the cavity ring-down measurement and covering the required dynamic range for the CELIF device. Flowing the samples through the flow-body minimises the stickiness of acetone in the cavity walls and mirrors, which is essential for making sensitive measurements, by preventing acetone desorption during the measurements. Any residuals of acetone which will be left in the cavity after a CELIF measurement could be flushed away by flowing air or nitrogen through the system from the three inlets: the flow-body inlet and from both side arms of the cavity and exit the system through the flow-body outlet, flushing any acetone residuals that might be stuck on the cavity walls.

After optimising the acetone CELIF measurement procedure, an acetone concentration 3σ limit of detection of 1.6 ppm, was achieved, when averaging every 1500 laser shots with the 15 kHz laser. This laser allowed making a CELIF measurement every 100 ms, averaging every 1500 laser shots. The CELIF dynamic range achieved with this laser was 1.6–2000 ppm, covering the range of breath acetone concentration a DKA patient might have.

The response-time of the CELIF measurements was optimised by optimising the design of the flow-body, and the gas sampling method. It was found that the 10–90% rise time of the CELIF measurement was 370 $\pm$ 15 ms, and the 90–10% fall time was 850 $\pm$ 21 ms. The slower fall time is likely to be caused by some acetone sticking into the tube fittings before the flow-body which takes some time to clear up. The rise time of the CELIF measurement is fast enough to faithfully find the maximum

acetone concentration. Although the measured fall time is not as fast, as long as the signal returns to the baseline before the next breath arrives then the CELIF measurement is fast enough to follow a real breath pattern. The response time of the CELIF measurement was tested using a made up mixture of acetone in air, using a simple sampling method which mimics a breathing pattern. These measurements could not be tested with breath acetone signals, as no measurements were made on diabetic patients, and at this stage, a healthy human breath acetone level can not be detected.

The 15 kHz Elforlight laser used for the CELIF measurements was not performing very well, as the averaged laser power was decaying over time. By the time the CELIF dynamic range measurements were taken, the laser pulse energy was reduced to only about 0.02 μJ per pulse. Another laser with a much higher laser pulse energy (up to 170 μJ per pulse), but with a slower repetition rate of 10 Hz, was used to investigate the limit of detection (LOD) of the CELIF measurements. We have found that this laser lowered the acetone CELIF 3σ LOD, from 1.6 ppm (averaging every 1500 laser shots, every 100 ms) to 270 ppb (averaging every 512 laser shots every 52 s). However, measuring high acetone concentrations with high laser pulse energy will be limited due to the photon counting regime limit. To expand the acetone CELIF dynamic range and allow measuring breath acetone in real-time, it is recommended to use one of the following:

- A high laser repetition rate with high laser pulse energy. Do CELIF calibration with photon counting and area integration simultaneously to have a calibration for both. The LIF PMT will need two different operating voltages. A high voltage is needed for photon counting mode, and a low voltage for area integration mode. All photon counting measurements must be taken at exactly the same PMT voltage, so too must the area integration measurements. A voltage divider with a fixed output ratio might be used to reduce the voltage when integrating the area, to allow the PMT to operate in two modes.

- A high laser repetition rate with variable laser pulse energies. This will require turning the pulse energy down at a certain acetone concentration threshold to

be within the photon counting regime, and rely in a single calibration which is made in the photon counting regime.

To make a breath acetone CELIF measurement every 100 ms, it is recommended to use a pulsed laser with repetition rate of 10 kHz, a variable pulse energy up to 100 μJ and average every 1000 laser shots. This should lower the acetone CELIF LOD to 200 ppb. Another combination would be to use a pulsed laser with a repetition rate of 1 kHz, a variable pulse energy up to 150 μJ and average every 100 laser shots. This would allow the acetone CELIF LOD to be about 300 ppb. Although higher laser pulse energies might be available, the damage threshold of the optics should be considered.

The CELIF device was validated against a selected ion flow tube mass spectrometer (SIFT-MS). The concentrations of acetone in home-made samples and standard gas mixtures were measured simultaneously by the CELIF and the SIFT-MS instruments. This validation test proved that the acetone concentration measurements by the CELIF device is reliable, fast and can be used for measurements of breath samples.

We have shown that breath acetone concentration could be measured using CELIF without the need to remove other breath gas components from the sample. The existence of O_2, CO_2 and water vapour in the breath does not affect the measured acetone CELIF signal. For the next design of the CELIF device it is recommended to use a fast response mass flow controller that is independent of the humidity, temperature and the components of the flowing gas, such as a Coriolis based mass flow controller (Bronkhorst mini Cori-flow series).

We have built a buffered-end tidal breath sampler, which was useful for sampling breath of fasted healthy subjects. At the current stage of this research, no measurements were made on diabetic patients. Thus, we were unable to test the effect of different sampler temperatures or different breath flow rate on the breath acetone concentration.

7.2 Future Work

Currently, the CELIF setup is mounted in an optical table in our laboratory. The device needs to be made more compact and made mobile. The next stage is to fit the device in a 19-inch rack to be used for medical testing. The device, including the laser, the optical cavity, the optics will be mounted on a standard optical breadboard, which will be mounted vertically in the 19-inch rack, to minimize the footprint of the device. The other equipment such as, the PMT voltage supply unit, the analog integrator, the mass flow controllers, the CO_2 sensor, the vacuum pump, gas cylinders for the device calibration, the pressure display unit, the laser box, a computer, a screen, a breath sampler will also be mounted in the 19-inch rack.

Secure measures will be taken to ensure greater mechanical robustness and cavity stability to ensure misalignment of the laser does not occur upon movement. The cavity should be kept clean by flowing nitrogen through the cavity without evacuating the cavity to ensure that no pressure change affects the alignment.

The device will be modified such that it can be operated easily by non experts. CELIF calibration procedure will be automated by replacing the manually operated valves with actuated valves, and by using standard acetone–nitrogen gas mixtures. A LabView program will be modified to control the calibration procedure and calculate the calibration factor straight after the measurements. The current cavity mirror mounts could be redesigned to ensure reproducible mirror alignment after the periodic cleaning of the mirrors.

The most expensive parts of the CELIF device could be replaced to make the device cost effective. The pulsed ND:YAG laser, which costs thousands of pounds could possibly be replaced with cheap, high power UV LED. The expensive workstation PC and the digitizer could be replaced with cheaper, pared-down, custom electronics.

A non-invasive breath sampling device which does not require any active engagement from a patient, such as a nasal cannula, should be developed. As it is not a straight forward process to test the breath samplers on diabetic or DKA patients, the breath samplers could be tested on healthy individuals who have had their breath acetone level elevated by a ketogenic diet.

The correlation between breath acetone and blood β-hydroxybutyrate (BHB) has not been established at high blood BHB levels. In the long term, our aim is to study this correlation in a large cohort of children and young people with type 1 diabetes. This study is expected to take a long period of time to collect a high patient throughputs.

The requirements which were set for the CELIF device: LOD of lower than 500 ppb, CELIF measurement dynamic range of less than 1 ppm to more than 1000 ppm, response time in the order of 500 ms, measurement speed of 100 ms has been met. The rest of the device requirements: breath sampling capability, mobility and cost effectiveness are still under investigation.

In the near future when all of the device requirements are met, the non-invasive, online, real-time, mobile, robust, cost-effective breath acetone CELIF device, which covers a large dynamic range of acetone concentrations, will win over the rest of the laser spectroscopy based breath acetone analysers, which either suffer at low or high acetone concentrations, or require sample preparation or storage or require active engagement from the patient. The self calibrated CELIF device could also replace the SIFT-MS device which, surprisingly, requires correction factors using external standards.

The CELIF device along with a pack of non-invasive devices such as non-invasive blood pH and blood bicarbonate measuring devices could reduce the need for the blood BHB tests, and could possibly replace them for the monitoring and management of diabetic ketoacidosis.

Bibliography

[1] L. Pauling, A. B. Robinson, R. Teranishi, and P. Cary, "Quantitative analysis of urine vapour and breath by gas - liquid partition chromatography," *Proceedings of the National Academy of Sciences of the United States of America*, vol. 68, pp. 2374–2376, 1971.

[2] C. Wang and P. Sahay, "Breath analysis using laser spectroscopic techniques: Breath biomarkers, spectral fingerprints, and detection limits," *Sensors*, vol. 9, no. 10, pp. 8230–8262, 2009.

[3] B. Henderson, A. Khodabakhsh, M. Metsälä, I. Ventrillard, F. M. Schmidt, D. Romanini, G. A. Ritchie, S. te Lintel Hekkert, R. Briot, T. Risby, N. Marczin, F. J. Harren, and S. M. Cristescu, "Laser spectroscopy for breath analysis: towards clinical implementation," *Applied Physics B: Lasers and Optics*, vol. 124, no. 8, pp. 1–21, 2018.

[4] Z. Wang and C. Wang, "Is breath acetone a biomarker of diabetes? A historical review on breath acetone measurements.," *Journal of breath research*, vol. 7, no. 3, p. 037109, 2013.

[5] T. D. C. Minh, D. R. Blake, and P. R. Galassetti, "The clinical potential of exhaled breath analysis for diabetes mellitus," *Diabetes Research and Clinical Practice*, vol. 97, no. 2, pp. 195–205, 2012.

[6] V. Ruzsányi and M. P. Kalapos, "Breath acetone as a potential marker in clinical practice," *Journal of Breath Research*, vol. 11, no. 2, 2017.

[7] Diabetes UK - Know diabetes. Fight diabetes, Diabetes: the basics, https://www.diabetes.org.uk/, Accessed: April 2019.

[8] A. A. Klocker, H. Phelan, S. M. Twigg, and M. E. Craig, "Blood β-hydroxybutyrate vs. urine acetoacetate testing for the prevention and management of ketoacidosis in Type 1 diabetes: A systematic review," *Diabetic Medicine*, vol. 30, no. 7, pp. 818–824, 2013.

[9] National Collaborating Centre for Women's and Children's Health (UK), "Diabetes (Type 1 and Type 2) in Children and Young People Diagnosis and Management", National Institute for Health and Care Excellence (UK), Aug, 2015.

[10] K. J. Noyes, P. Crofton, L. E. Bath, A. Holmes, L. Stark, C. D. Oxley, and C. J. Kelnar, "Hydroxybutyrate near-patient testing to evaluate a new endpoint for intravenous insulin therapy in the treatment of diabetic ketoacidosis in children," *Pediatric Diabetes*, vol. 8, no. 3, pp. 150–156, 2007.

[11] T. P. J. Blaikie, J. A. Edge, G. Hancock, D. Lunn, C. Megson, R. Peverall, G. Richmond, G. A. D. Ritchie, and D. Taylor, "Comparison of breath gases, including acetone, with blood glucose and blood ketones in children and adolescents with type 1 diabetes," *Journal of Breath Research*, vol. 8, p. 046010, nov 2014.

[12] G. Hancock, C. E. Langley, R. Peverall, G. A. Ritchie, and D. Taylor, "Laser-based method and sample handling protocol for measuring breath acetone," *Analytical Chemistry*, vol. 86, no. 12, pp. 5838–5843, 2014.

[13] M. Sun, Z. Wang, Y. Yuan, Z. Chen, X. Zhao, Y. Li, and C. Wang, "Continuous Monitoring of Breath Acetone, Blood Glucose and Blood Ketone in 20 Type 1 Diabetic Outpatients Over 30 Days," *Journal of Analytical & Bioanalytical Techniques*, vol. 08, no. 05, 2017.

[14] D. Smith, P. Španěl, A. A. Fryer, F. Hanna, and G. A. Ferns, "Can volatile compounds in exhaled breath be used to monitor control in diabetes mellitus?," *Journal of Breath Research*, vol. 5, no. 2, 2011.

[15] J. Herbig, T. Titzmann, J. Beauchamp, I. Kohl, and A. Hansel, "Buffered end-tidal (BET) sampling - A novel method for real-time breath-gas analysis," *Journal of Breath Research*, vol. 2, no. 3, 2008.

[16] J. Herbig and J. Beauchamp, "Towards standardization in the analysis of breath gas volatiles," *Journal of Breath Research*, vol. 8, p. 037101, sep 2014.

[17] J. King, K. Unterkofler, G. Teschl, S. Teschl, H. Koc, H. Hinterhuber, and A. Amann, "A mathematical model for breath gas analysis of volatile organic compounds with special emphasis on acetone," *Journal of Mathematical Biology*, vol. 63, no. 5, pp. 959–999, 2011.

[18] C. Turner, P. Španěl, and D. Smith, "A longitudinal study of ammonia, acetone and propanol in the exhaled breath of 30 subjects using selected ion flow tube mass spectrometry, SIFT-MS," *Physiological Measurement*, vol. 27, no. 7, pp. 637–648, 2006.

[19] W. Lindinger, A. Hansel, and A. Jordan, "On-line monitoring of volatile organic compounds at pptv levels by means of proton-transfer-reaction mass spectrometry (PTR-MS) medical applications, food control and environmental research," *International Journal of Mass Spectrometry and Ion Processes*, vol. 173, no. 3, pp. 191–241, 1998.

[20] M. Righettoni, A. Tricoli, S. Gass, A. Schmid, A. Amann, and S. E. Pratsinis, "Breath acetone monitoring by portable Si:WO3 gas sensors," *Analytica Chimica Acta*, vol. 738, pp. 69–75, 2012.

[21] T. Toyooka, S. Hiyama, and Y. Yamada, "A prototype portable breath acetone analyzer for monitoring fat loss," *J Breath Res*, vol. 7, no. 3, p. 36005, 2013.

[22] D. H. Kim, Y. S. Shim, J. M. Jeon, H. Y. Jeong, S. S. Park, Y. W. Kim, J. S. Kim, J. H. Lee, and H. W. Jang, "Vertically ordered hematite nanotube array as an ultrasensitive and rapid response acetone sensor," *ACS Applied Materials and Interfaces*, vol. 6, no. 17, pp. 14779–14784, 2014.

[23] K. Schwarz, W. Filipiak, and A. Amann, "Determining concentration patterns of volatile compounds in exhaled breath by PTR-MS.," *Journal of Breath Research*, vol. 3, no. 2, p. 027002, 2009.

[24] P. Španěl and D. Smith, "Progress in SIFT-MS: Breath analysis and other applications," *Mass Spectrometry Reviews*, vol. 30, pp. 236–267, jul 2010.

[25] D. Smith and P. Španěl, "SIFT-MS and FA-MS methods for ambient gas phase analysis: Developments and applications in the UK," *Analyst*, vol. 140, no. 8, pp. 2573–2591, 2015.

[26] D. Smith and P. Španěl, "Selected ion flow tube mass spectrometry (SIFT-MS) for on-line trace gas analysis," *Mass Spectrometry Reviews*, vol. 24, no. 5, pp. 661–700, 2005.

[27] A. Prabhakar, A. Quach, D. Wang, and H. Zhang, "Breath Acetone as Biomarker for Lipid Oxidation and Early Ketone Detection," *Global Journal of Obesity, Diabetes and Metabolic Syndrome*, vol. 1, pp. 12–19, 2014.

[28] C. Wang and A. B. Surampudi, "An acetone breath analyzer using cavity ringdown spectroscopy: an initial test with human subjects under various situations," *Measurement Science and Technology*, vol. 19, no. 10, p. 105604, 2008.

[29] C. Wang and A. Mbi, "A new acetone detection device using cavity ringdown spectroscopy at 266 nm: evaluation of the instrument performance using acetone sample solutions," *Measurement Science and Technology*, vol. 18, no. 8, pp. 2731–2741, 2007.

[30] L. Ciaffoni, G. Hancock, J. J. Harrison, J. P. H. Van Helden, C. E. Langley, R. Peverall, G. A. D. Ritchie, and S. Wood, "Demonstration of a mid-infrared cavity enhanced absorption spectrometer for breath acetone detection," *Analytical Chemistry*, vol. 85, no. 2, pp. 846–850, 2012.

[31] T. P. J. Blaikie, J. Couper, G. Hancock, P. L. Hurst, R. Peverall, G. Richmond, G. A. D. Ritchie, D. Taylor, and K. Valentine, "Portable Device for Measur-

ing Breath Acetone Based on Sample Preconcentration and Cavity Enhanced Spectroscopy," *Analytical Chemistry*, vol. 88, no. 22, pp. 11016–11021, 2016.

[32] M. Sun, C. Jiang, Z. Gong, X. Zhao, Z. Chen, Z. Wang, M. Kang, Y. Li, and C. Wang, "A fully integrated standalone portable cavity ringdown breath acetone analyzer," *Review of Scientific Instruments*, vol. 86, p. 095003, sep 2015.

[33] M. Mazurenka, A. J. Orr-Ewing, R. Peverall, and G. A. Ritchie, "Cavity ring-down and cavity enhanced spectroscopy using diode lasers," *Annual Reports on the Progress of Chemistry - Section C*, vol. 101, pp. 100–142, 2005.

[34] M. Nowakowski, J. Wojtas, Z. Blelecki, and J. Mlkołłajczyk, "Cavity enhanced absorption spectroscopy sensor," *Acta Physica Polonica A*, vol. 116, no. 3, pp. 363–367, 2009.

[35] J. C. Anderson, "Measuring breath acetone for monitoring fat loss: Review," *Obesity*, vol. 23, no. 12, pp. 2327–2334, 2015.

[36] A. Rewers, K. McFann, and H. P. Chase, "Bedside monitoring of blood β-hydroxybutyrate levels in the management of diabetic ketoacidosis in children," *Diabetes technology & therapeutics*, vol. 8, no. 6, pp. 671–676, 2006.

[37] A. Q. T. Pham, L. H. R. Xu, and O. W. Moe, "Drug-induced metabolic acidosis," *F1000Research*, vol. 4, p. 1460, 2015.

[38] T. Kato, A. Tsukanaka, T. Harada, M. Kosaka, and N. Matsui, "Effect of hypercapnia on changes in blood pH, plasma lactate and ammonia due to exercise," *European Journal of Applied Physiology*, vol. 95, no. 5-6, pp. 400–408, 2005.

[39] M. M. Adeva and G. Souto, "Diet-induced metabolic acidosis," *Clinical Nutrition*, vol. 30, no. 4, pp. 416–421, 2011.

[40] R. A. Feenstra, M. K. Kiewiet, E. C. Boerma, and E. ter Avest, "Lactic acidosis in diabetic ketoacidosis," *Case Reports*, vol. 2014, p. bcr2014203594, 2014.

[41] M. K. Alam, M. R. Rohrscheib, J. E. Franke, T. M. Niemczyk, J. D. Maynard, and M. R. Robinson, "Measurement of pH in whole blood by near-infrared spectroscopy," *Applied Spectroscopy*, vol. 53, no. 3, pp. 316–324, 1999.

[42] N. A. Rosen, W. E. Charash, and E. F. Hirsch, "Near-infrared spectrometric determination of blood pH," *Journal of Surgical Research*, vol. 106, no. 2, pp. 282–286, 2002.

[43] Y. E. Yang, O. O. Soyemi, M. R. Landry, and B. R. Soller, "Noninvasive in vivo measurement of venous Blood pH during exercise using near-infrared reflectance spectroscopy," *Applied Spectroscopy*, vol. 61, no. 2, pp. 223–229, 2007.

[44] E. Ferber, A. DeKelaita, R. Narayanan, and P. J. Cobut, "Systems and Methods for Biological Metrics Measurement," 2018. US Patent US20180085040A1.

[45] H. Y. Y. Nyein, W. Gao, Z. Shahpar, S. Emaminejad, S. Challa, K. Chen, H. M. Fahad, L. C. Tai, H. Ota, R. W. Davis, and A. Javey, "A Wearable Electrochemical Platform for Noninvasive Simultaneous Monitoring of Ca 2+ and pH," *ACS Nano*, vol. 10, no. 7, pp. 7216–7224, 2016.

[46] A. Charogiannis and F. Beyrau, "Investigation of laser induced phosphorescence properties of acetone," *16th Int Symp on Applications of Laser Techniques to Fluid Mechanics*, no. July 2012, pp. 1–12, 2012.

[47] A. Lozano, B. Yip, and R. K. Hanson, "Acetone: A Tracer for Concentration Measurements in Gaseous Flow by Planar Laser-Induced Fluorescence," *Experiments in Fluids*, vol. 13, pp. 369–376, 1992.

[48] M. A. Blitz, D. E. Heard, and M. J. Pilling, "Study of acetone photodissociation over the wavelength range 248-330 nm: Evidence of a mechanism involving both the singlet and triplet excited states," *Journal of Physical Chemistry A*, vol. 110, no. 21, pp. 6742–6756, 2006.

[49] K. L. K. Lee, K. Nauta, and S. H. Kable, "Photodissociation of acetone from 266 to 312 nm: Dynamics of CH_3 + CH_3CO channels on the S_0 and T_1 states," *Journal of Chemical Physics*, vol. 146, no. 4, pp. 0–12, 2017.

[50] M. C. Thurber, F. Grisch, B. J. Kirby, M. Votsmeier, and R. K. Hanson, "Measurements and modeling of acetone laser-induced fluorescence with implications for temperature-imaging diagnostics.," *Applied optics*, vol. 37, no. 21, pp. 4963–4978, 1998.

[51] R. A. Bryant, J. M. Donbar, and J. F. Driscoll, "Acetone laser induced fluorescence for low pressure/low temperature flow visualization," *Experiments in Fluids*, vol. 28, no. 5, pp. 471–476, 2000.

[52] J. Ashenhurst, "UV-Vis Spectroscopy: Absorbance of Carbonyls, https://www.masterorganicchemistry.com/2016/09/26/uv-vis-spectroscopy-absorbance-of-carbonyls/three, Sep 2016, Accessed: July 2019.

[53] F. Ossler and M. Alden, "Measurements of picosecond laser induced fluorescence from gas phase 3-pentanone and acetone: Implications to combustion diagnostics," *Applied Physics B: Lasers and Optics*, vol. 64, pp. 493–502, 1997.

[54] S. E. Sanders, O. R. Willis, N. H. Nahler, and E. Wrede, "Absolute fluorescence and absorption measurements over a dynamic range of 106 with cavity-enhanced laser-induced fluorescence," *Journal of Chemical Physics*, vol. 149, no. 1, 2018.

[55] M. D. Wheeler, S. M. Newman, A. J. Orr-Erwing, and M. N. Ashfold, "Cavity Ring-Down Spectroscopy," *J. Chem. Soc.*, vol. 94, no. 3, pp. 337 – 351, 1998.

[56] D. Romanini, I. Ventrillard, G. Méjean, J. Morville, and E. Kerstel, "Introduction to cavity enhanced absorption spectroscopy," in *Cavity-Enhanced Spectroscopy and Sensing*, pp. 1–60, Springer, 2014.

[57] C. Harris and B. Selinger, "Single-Photon Decay Spectroscopy. II. The Pile-up Problem," *Australian Journal of Chemistry*, vol. 32, no. 10, pp. 2111–2129, 1979.

[58] J. D. Driscoll, A. Y. Shih, S. Iyengar, J. J. Field, G. A. White, J. A. Squier, G. Cauwenberghs, and D. Kleinfeld, "Photon counting, censor corrections, and lifetime imaging for improved detection in two-photon microscopy," *Journal of Neurophysiology*, vol. 105, no. 6, pp. 3106–3113, 2011.

[59] X. Ding, K. Zang, Y. Fei, T. Zheng, T. Su, M. Morea, G. Jin, J. S. Harris, X. Jiang, and Q. Zhang, "Pile-up correction in characterizing single-photon avalanche diodes of high dark count rate," *Optical and Quantum Electronics*, vol. 50, no. 6, pp. 1–11, 2018.

[60] R. Feng, D. Rundle, and G. Wang, "Neural-networks-based Photon-Counting Data Correction: Pulse Pileup Effect," pp. 1–14, April 2018.

[61] P. Taylor-Burdett, "Optimisation of a LIF setup for a CELIF Sensor for Breath Acetone", Masters thesis, Durham University, 2017.

[62] J. Landes, " Optimisation of Analyte-Gas Flow Through a CELIF Sensor for Breath Acetone", Masters thesis, Durham University, 2018.

[63] A. D. Elster, "Classification of Flow", http://mriquestions.com/laminar-v-turbulent.html, 2015, Accessed: Sep 2019.

[64] Glenn Research Center, "Mach Number", https://www.grc.nasa.gov/www/k-12/airplane/mach.html, March, 2018, Accessed: Sep 2019.

[65] T. Risby and S. Solga, "Current status of clinical breath analysis," *Applied Physics B*, vol. 85, no. 2, pp. 421–426, 2006.

[66] P. Sahay, S. T. Scherrer, and C. Wang, "Measurements of the weak UV absorptions of isoprene and acetone at 261-275 nm using cavity ringdown spectroscopy for evaluation of a potential portable ringdown breath analyzer.," *Sensors (Basel, Switzerland)*, vol. 13, no. 7, pp. 8170–8187, 2013.

[67] C. Schulz and V. Sick, "Tracer-LIF diagnostics: Quantitative measurement of fuel concentration, temperature and fuel/air ratio in practical combustion systems," *Progress in Energy and Combustion Science*, vol. 31, no. 1, pp. 75–121, 2005.

[68] M. C. Thurber and R. K. Hanson, "Pressure and composition dependences of acetone laser-induced fluorescence with excitation at 248, 266, and 308 nm," *Applied Physics B: Lasers and Optics*, vol. 69, no. 3, pp. 229–240, 1999.

[69] M. C. Thurber and R. K. Hanson, "Simultaneous imaging of temperature and mole fraction using acetone planar laser-induced fluorescence," *Experiments in Fluids*, vol. 30, no. 1, pp. 93–101, 2001.

[70] M. Righettoni, A. Ragnoni, A. T. Güntner, C. Loccioni, S. E. Pratsinis, and T. H. Risby, "Monitoring breath markers under controlled conditions," *Journal of Breath Research*, vol. 9, no. 4, p. 047101, 2015.

[71] A. Anthony, " Measuring Breath Acetone", Masters thesis, Durham University, 2018.

Appendix A

Under-Counting

A.1 Amount of Under-Counting

Using the substitution $x = \exp(-t/\tau)$ to solve the integral in Eqn 2.3.47 we get:

$$\begin{aligned}
S_{\mathrm{c}} &= \frac{1}{\Delta t}\int_1^0 \left(1 - e^{-S_0\,x}\right)\,\left(-\frac{\tau}{x}\right)\,\mathrm{d}x, \\
&= \frac{\tau}{\Delta t}\int_0^1 \frac{1}{x} - \frac{e^{-S_0\,x}}{x}\,\mathrm{d}x, \\
&= \frac{\tau}{\Delta t}\,\left[\ln x - \left(\ln x + \frac{-S_0\,x}{1\cdot 1!} + \frac{(-S_0\,x)^2}{2\cdot 2!} + \frac{(-S_0\,x)^3}{3\cdot 3!} + \ldots\right)\right]_0^1, \\
&= \frac{\tau}{\Delta t}\,\left(S_0 - \frac{S_0^2}{2\cdot 2!} + \frac{S_0^3}{3\cdot 3!} - \ldots\right).
\end{aligned}$$

This can be simplified to

$$\begin{aligned}
S_{\mathrm{c}} &= S_{\mathrm{tot}}\,\left(1 - \frac{S_0}{4} + \frac{S_0^2}{18} - \frac{S_0^3}{96} + \ldots\right), \\
&= S_{\mathrm{tot}}\,\left(1 - \frac{1}{4}\left(S_{\mathrm{tot}}\frac{\Delta t}{\tau}\right) + \frac{1}{18}\left(S_{\mathrm{tot}}\frac{\Delta t}{\tau}\right)^2 - \frac{1}{96}\left(S_{\mathrm{tot}}\frac{\Delta t}{\tau}\right)^3 + \ldots\right).
\end{aligned}$$

A.2 Alternative Derivation

The probability of two photons falling into the first bin is the square of Eqn 2.3.40. The probability to find two photons at time t in the decay is then

$$p^{(2)}(t) = \left(S_0\,e^{-t/\tau}\right)^2,$$

and integration gives the number of two-photon events within each shot:

$$P^{(2)} = \int_0^\infty S_0^2\, e^{-2t/\tau}\, \frac{1}{\Delta t}\, \mathrm{d}t = \frac{S_0^2 \tau}{2\Delta t} = \frac{S_{\mathrm{tot}}^2}{2} \cdot \frac{\Delta t}{\tau}.$$

Each two-photon event leads to only one photon being counted, which is already included in the single-photon count. Hence, the two-photon under-count is half of $P^{(2)}$:

$$S_{\mathrm{uc}}^{(2)} = P^{(2)}/2 = \frac{S_{\mathrm{tot}}^2}{4} \cdot \frac{\Delta t}{\tau},$$

which is the same as the two-photon correction derived via the Poisson distribution above.